

# The development and characterization of a thermosiphon photobioreactor for the cultivation of photosynthetic bacteria

*by*

BOVINILLE ANYE CHO

Thesis presented in partial fulfillment  
of the requirements for the Degree

The crest of Stellenbosch University, featuring a shield with a red and white design, topped with a crown and a banner. The word 'of' is written in a cursive font above the shield.  
MASTER OF ENGINEERING  
(CHEMICAL ENGINEERING)

UNIVERSITEIT  
iYUNIVESITHI  
STELLENBOSCH  
UNIVERSITY

in the Faculty of Engineering  
at Stellenbosch University

1918 · 2018

Supervisor  
Dr. Robbie Pott

December 2018

## **DECLARATION**

By submitting this thesis electronically, I declare that the entirety of the work contained therein is my own, original work, that I am the sole author thereof (save to the extent explicitly otherwise stated), that reproduction and publication thereof by Stellenbosch University will not infringe any third party rights and that I have not previously in its entirety or in part submitted it for obtaining any qualification.

Date: **December 2018**

## PLAGIARISM DECLARATION

1. Plagiarism is the use of ideas, material and other intellectual property of another's work and to present is as my own.
2. I agree that plagiarism is a punishable offence because it constitutes theft.
3. I also understand that direct translations are plagiarism.
4. Accordingly all quotations and contributions from any source whatsoever (including the internet) have been cited fully. I understand that the reproduction of text without quotation marks (even when the source is cited) is plagiarism.
5. I declare that the work contained in this assignment, except where otherwise stated, is my original work and that I have not previously (in its entirety or in part) submitted it for grading in this module/assignment or another module/assignment.

Student number: **21490406**

Initials and surname: **B. ANYE CHO**

Signature:

A handwritten signature in blue ink, appearing to read 'B. Anye Cho', is displayed on a light blue rectangular background.

Date: **November 7, 2018**

## **ACKNOWLEDGEMENT**

Firstly, I would like to acknowledge my supervisor Dr. Robbie Pott for his continuous guidance, support and encouragement through my studies at Stellenbosch University. Also, I want to appreciate the valuable suggestions and helpful discussions of Dr. Tobi Louw and Godfrey Gakingo which were very vital towards my understanding of the CFD modeling technique.

I am very grateful to the Mandela Rhodes Foundation, South Africa for their fully funded scholarship which was established since 2005 to build exceptional leadership capacity in Africa (whilst also seeking to foster better reconciliation and entrepreneurship) through its various programmes.

I wish to appreciate my fellow BPEG Research Group mates JP Du Toit, Ayman A. Abufalgah, M.A. van Niekerk, Philip Uys, and G.M. Teke for making me enjoy a pleasant working environment. Thanks to Jos and George White for technical workshop assistance and computational resource support at Department of Process Engineering respectively.

I need to specially thank my mother, Asanji Patience Fru, brothers, Anye Makeeva Awah and Asanji Alain Aburi for their love, support and encouragement during the hardest times of years.

## ABSTRACT

Since their 1<sup>st</sup> appearance in 1940s, closed photobioreactors (PBRs) have received significant attention as biotechnological systems, as viable alternatives to open systems. These improvements were aimed at addressing the very high material, operational, and production costs (circa 80% of total cost) associated with the energy input for aeration or agitation by mechanical and pneumatic devices. This thesis describes a PBR designed to exploit natural fluid circulation in closed loops, achieved by the thermosiphon effect arising from the temperature-induced density differential due to microbial light absorption and subsequent cooling. This PBR design provides important energy and cost savings through elimination of the mechanical and pneumatic devices.

Light, being an obligate requirement for photosynthetic microorganisms within PBRs, can additionally power natural fluid circulation (the thermosiphon effect) in solar water heating systems (SWHS). Therefore, this work begins by structurally adapting the original thermosiphon loop published by Close in 1962 to meet the design criteria of a photobioreactor, resulting in a Thermosiphon Photobioreactor (TPBR) geometry comprising of five main sections: (i) adiabatic vertical cylindrical storage tank, (ii) truncated cone-shaped cooling section, and (iii) adiabatic downcomer, (iv) heating section (collector /absorber) and (v) adiabatic upriser. The TPBR's geometry was sized to 1-L working volume through a single parameter optimization for the riser diameter, and constructed from glass and other hydrogen impermeable auxiliary units for Experimental Fluid Dynamic (EFD) studies.

To get valuable insights into the reactor's thermal and hydrodynamic performance, Computational Fluid Dynamics (CFD) was used to theoretically investigate the design, and operation of such a reactor systems. The CFD model was based on a 2D transient model which accounted for the non-uniform volumetric sensible heating due to microbial light absorption. This extends on previous studies on thermosiphon modeling which made use of simplified boundary conditions such as uniform constant wall temperatures and surface flux by accounting for the non-uniform light and heat distribution, which varies throughout the reactor as per a Beer-Lambert type curve. The light absorptive model was implemented via a User-Defined Function (UDF) which incorporated experimentally obtained spectral irradiance and attenuation parameters of *Rhodospseudomonas palustris*. The TPBR's buoyancy driven convection was

characterized by the boussinesq approximation as well as experimental and theoretical estimated heat transfer coefficients.

The resulting CFD simulations have limited usefulness without experimental validation, in part due to the complexity of this study. Therefore, experimental data from thermocouple sensors, and marker image trackers fitted to the TPBR containing a biomass loading of  $0.5\text{kg/m}^3$  *Rhodopseudomonas palustris* were used to validate the CFD model at the same operating conditions. The CFD simulation results clearly demonstrated buoyancy driven characteristic flow profiles with strong eddies showed at the storage tank, while flow velocities were tilted more to the front than to the rear riser section. These simulation results were ascertained through validation experiments with active *Rhodopseudomonas palustris* and predicted the TPBR's thermal and hydrodynamic performance for all measuring points with a relatively small difference of less than 5% (317.7-307.9 K) and 10% (0.009-0.0085 m/s) as observed respectively. The flow visualization on the riser section of the TBPR also found that light absorption significantly influences fluid flow circulation and mixing which leads to a satisfactory agreement between the experimental observations and the CFD simulations results from a qualitative view point.

Additional experimentation with active and inactive *Rhodopseudomonas palustris* revealed that the bacterial metabolic heat generation and waste fluorescence heat significantly contributed to the overall thermal and thermosiphoning effect of the TPBR. There was a 4% and 8% increase in the steady state temperature and heating rate respectively from the active microbial light absorption. This corresponded to a 3% increase of active bacterial cells in free suspension throughout the steady state conditions. In general, the TPBR provided satisfactory passive fluid flow to keep bacterial cells in suspension, maintaining up to 88% of the active bacterial loading in free suspension

## ABSTRAK

Sedert hul eerste verskyning in die 1940's, het geslote fotobioreaktors (FBRs) 'n beduidende hoeveelheid aandag ontvang as biotegnologiese stelsels en as lewensvatbare alternatiewe tot oop stelsels. Hierdie verbeteringe streef om die probleem van die baie hoë materiaal-, operasionele, en produksiekostes (circa 80% van totale koste) wat geassosieer word met die energie-inset vir belugting en beroering deur meganiese en pneumatiese toestelle, op te los. Hierdie tesis beskryf 'n FBR wat ontwerp is om die natuurlike vloeistof sirkulasie in geslote lusse te benut, wat bereik word deur die termosifon-effek wat ontstaan vanuit die temperatuur geïnduseerde digtheid differensiaal weens die mikrobiële ligabsorpsie en daaropvolgende afkoeling. Hierdie FBR-ontwerp voorsien belangrike energie- en kostebesparings deur die eliminerings van meganiese en pneumatiese toestelle.

Lig, wat 'n verpligte vereiste vir fotosintetiese mikro-organismes binne FBR is, kan natuurlike vloeistofsirkulasie (die termosifon-effek) in sonwaterverhittingstelsels (SWVS) aandryf. In hierdie werk word die oorspronklike termosifonlus, gepubliseer deur Close in 1962, struktureel aangepas om aan die ontwerp kriteria van 'n fotobioreaktor te voldoen. Dit het 'n Termosifon Fotobioreaktor (TFBR) geometrie tot gevolg, wat bestaan uit vyf hoofdele: (i) adiabatiese vertikale silindriese opgaartenk, (ii) afgeknotte keëlvormige verkoelingseksie, (iii) adiabatiese sakpyp, (iv) verhittingseksie (opvanger/absorbeerder), en (v) adiabatiese stygpyp. Die TFBR se geometrie was geskaal tot 1 L bedryfsvolume deur 'n enkel parameter optimering vir die stygpypdeursnee en gebou uit glas en ander waterstof ondeurdringbare bykomende eenhede vir Eksperimentele Vloeddinamika (EVD) studies.

Om waardevolle insig in die reaktor se termiese en hidrodinamiese werkverrigting te kry, is Reken Vloeddinamika (RVD) gebruik om die ontwerp en werking van so 'n reaktorstelsel teoreties te ondersoek. Die RVD model is gebaseer op 'n 2D tydafhanklike model wat die nie-uniforme volumetriese waarneembare verhitting as gevolg van mikrobiële ligabsorpsie, in ag neem. Dit bou op vorige studies op termosifon modellering wat gebruik gemaak het van eenvoudige randtoestande soos uniforme konstante muur temperature en oppervlak vloed deur verantwoording te doen vir die nie-uniforme lig- en hitteverspreiding, wat varieer deur die reaktor volgens 'n Beer-Lambert tipe kurwe. Die ligabsorberende model is geïmplementeer deur 'n Gebruiker Gedefinieerde Funksie (GGF) wat spektrale uitstraling en dempingparameters van

*Rhodopseudomonas palustris* wat eksperimenteel verkry is, geïnkorporeer het. Die TFBR se dryfvermoë gedrewe konveksie was gekarakteriseer deur die Boussinesq benadering, sowel as eksperimentele en teoretiese beraamde hitte-oordrag koëffisiënte.

Die resulterende RVD simulaties het beperkte nuttigheid sonder eksperimentele validering, gedeeltelik as gevolg van die kompleksiteit van hierdie studie. Daarom is eksperimentele data van termokoppelsensors en merker beeld opspoorders vasgemaak aan die TFBR wat 'n biomassa lading van  $0.5 \text{ kg/m}^3$  *Rhodopseudomonas palustris* bevat, gebruik om die RVD model by dieselfde operasionele kondisies te valideer. Die RVD simulatie resultate het duidelik dryfvermoë gedrewe karakteristieke vloeiprofiel gedemonstreer en sterk werweling gewys by die opgaartenk, terwyl vloeisnelhede hoër was aan die voorkant as aan die agterkant van die stygpypdeel. Hierdie simulatie resultate is gestaaf deur validasie-eksperimente met aktiewe *Rhodopseudomonas palustris* en het voorspel dat die TFBR se termiese en hidrodinamiese werkverrigting vir alle metingspunte met 'n relatiewe klein verskil van minder as 5% (317.7-307.9 K) en 10% (0.009-0.0085 m/s), soos onderskeidelik waargeneem. Die vloeivisualisering op die stygpypdeel van die TFBR het ook gewys dat ligabsorpsie 'n beduidende invloed op vloeisirkulasie en vermenging het, wat lei tot 'n bevredigende ooreenkoms tussen die eksperimentele waarnemings en die RVD simulatie resultate vanuit 'n kwalitatiewe oogpunt.

Addisionele eksperimentasie met aktiewe en onaktiewe *Rhodopseudomonas palustris* het gewys dat die bakteriële metaboliese hitte opwekking en afvalfluoresensiehitte 'n aansienlike bydrae gemaak het tot die algehele termiese en termosifoniese effek van die TFBR. Daar was 'n 4% en 8% verhoging in die bestendige toestand temperatuur en verhitings tempo onderskeidelik van die aktiewe mikrobiële ligabsorpsie. Dit stem ooreen met 'n 3% verhoging van aktiewe bakteriële selle in die vrye suspensie regdeur die bestendige toestand kondisies. Oor die algemeen, het die TFBR bevredigende passiewe vloeistof vloeiverskaf om die bakteriële selle in suspensie te hou, wat tot 88% van die aktiewe bakteriële lading in vrye suspensie gehandhaaf het.



# TABLE OF CONTENTS

<b>DECLARATION.....</b>	<b>ii</b>
<b>PLAGIARISM DECLARATION.....</b>	<b>iii</b>
<b>ACKNOWLEDGEMENT.....</b>	<b>iv</b>
<b>ABSTRACT.....</b>	<b>v</b>
<b>ABSTRAK.....</b>	<b>vii</b>
<b>TABLE OF CONTENTS .....</b>	<b>ix</b>
<b>LIST OF FIGURES .....</b>	<b>xii</b>
<b>LIST OF TABLES .....</b>	<b>xvi</b>
<b>NOMENCLATURE.....</b>	<b>xvii</b>
<b>CHAPTER ONE: INTRODUCTION.....</b>	<b>1</b>
1.1 BACKGROUND AND MOTIVATION .....	1
1.2 RESEARCH OBJECTIVES AND QUESTIONS .....	4
1.2.1 OBJECTIVES.....	4
1.2.2 RESEARCH QUESTIONS .....	5
1.3 THESIS OVERVIEW.....	5
<b>CHAPTER TWO: LITERATURE REVIEW.....</b>	<b>7</b>
2.1 PHOTOFERMENTATION BY PURPLE NON-SULPUR BACTERIA.....	7
2.2 PHOTOBIOREACTORS: DESIGNS AND TYPES .....	10
2.2.1 VERTICAL COLUMN PBR.....	12
2.2.2 FLAT PLATE PBR .....	13
2.2.3 TUBULAR PBR.....	14
2.3 LIGHT AVAILABILITY, TRANSMISSION AND SIMULATION .....	16

2.4 THERMOSIPHON LOOPS, DESIGN AND APPLICATIONS .....	24
2.5 COMPUTATIONAL FLUID DYNAMICS MODELING AND EXPERIMENTAL VALIDATION .....	27
<b>CHAPTER THREE: MATERIALS AND METHODS .....</b>	<b>35</b>
3.1 RESEARCH DESIGN .....	35
3.2 THERMOSIPHON PBR'S DESIGN CONSIDERATION .....	36
3.3 THERMOSIPHON PBR'S GEOMETRY .....	37
3.3.1 ANALYTICAL MODEL FOR SIZING PROTOTYPE THERMOSIPHON PBR .....	38
3.4 EXPERIMENTAL FLUID DYNAMIC STUDIES .....	43
3.4.1 EXPERIMENTAL SETUP .....	43
3.4.2 FLUID FLOW, HEAT AND LIGHT TRANSFER RELATIONSHIPS IN THE TPBR .....	44
3.4.3 LAMP RADIATION MODELING FOR TPBR'S IRRADIANCE.....	50
3.4.4 RATE OF HEATING FROM LIGHT TRANSFER EXPERIMENTS .....	52
3.4.5 FRESH CULTURING OF BACTERIA FOR ACTIVE EXPERIMENTAL TESTING IN THE TPBR .....	54
3.4.6 FLUID FLOW VISUALIZATION .....	55
3.4.7 SEDIMENTATION EXPERIMENT .....	56
3.5 COMPUTATIONAL FLUID DYNAMICS MODELING .....	57
3.5.1 BOUNDARY CONDITIONS .....	59
3.5.2 SOLUTION STRATEGY AND CONVERGENCE CRITERION.....	60
3.6 ANALYTICAL METHOD .....	61
3.6.1 CELL CONCENTRATION .....	61
<b>CHAPTER FOUR: RESULTS AND DISCUSSIONS.....</b>	<b>62</b>
4.1 SPECTRAL PARAMETERS USED IN CFD MODELING.....	62
4.1.1 RESULTS OF HALOGEN LAMP RADIATION MODEL .....	62

4.1.3 RESULTS OF HEAT TRANSFER MEASUREMENTS .....	68
4.2 CFD SIMULATIONS RESULTS.....	71
4.2.1 TEMPERATURE DISTRIBUTION .....	71
4.2.2 VELOCITY DISTRIBUTION .....	75
4.3 FLOW VISUALIZATION RESULTS .....	79
4.4 VALIDATION: COMPARISON BETWEEN EXPERIMENTS RESULTS AND CFD SIMULATIONS.....	82
4.4.1 TEMPERATURE VALIDATION RESULTS.....	82
4.4.2 VELOCITY VALIDATION RESULTS .....	83
4.4.3 FLUID FLOW PROFILE VALIDATION RESULTS.....	84
4.5 EFFECT OF LIGHT ABSORPTION ON HEATING RATE .....	86
4.6 EFFECT LIGHT ABSORPTION ON THERMOSIPHONING CELLS.....	88
<b>CHAPTER FIVE: CONCLUSIONS AND RECOMMENDATIONS .....</b>	<b>90</b>
5.1 CONCLUSIONS.....	90
5.2 RECOMMENDATIONS .....	92
<b>REFERENCES.....</b>	<b>94</b>
<b>APPENDIX B: ANSYS WORKBENCH ENVIRONMENT .....</b>	<b>108</b>
<b>APPENDIX C: CFD RESIDUAL MONITORING .....</b>	<b>109</b>
<b>APPENDIX C: NETWON'S LAW OF COOLING .....</b>	<b>111</b>
<b>APPENDIX D: <i>R. PALUSTRIS</i> GROWTH FORMULA .....</b>	<b>113</b>
<b>APPENDIX E: COMPOSITON OF INOCULATED GROWTH MEDIA FOR <i>R.</i> <i>PALUSTRIS</i>.....</b>	<b>114</b>
<b>APPENDIX F: EXPERIMENTAL EQUIPMENT.....</b>	<b>115</b>
<b>APPENDIX F: THERMOCOUPLE MANUFACTURER'S SPECIFICATION .....</b>	<b>118</b>
<b>APPENDIX G: HALOGEN LAMP MANUFACTURERS GUIDE .....</b>	<b>119</b>

## LIST OF FIGURES

Figure 1: Schematic diagram of purple photosynthetic bacteria habitat position in their natural habitat redrawn from Dwi & Reksodipuro (2009).....	7
Figure 2: Schematic diagram of microbial population growth redrawn from (Clarke, 2013).....	9
Figure 3: Schematic diagrams of: (A) bubble column PBR, (B) internal-loop (draft-tube) airlift PBR, (C) split column airlift PBR and (D) external loop airlift PBR redrawn from (Wang et al., 2012). .....	13
Figure 4: Schematic diagram of the (A) side view of a flat plat PBR, and (B) front view of a pump-driven flat plat PBR redrawn from (Wang et al., 2012).....	14
Figure 5: Schematic diagram of a Tubular Photobioreactor with parallel run horizontal tubes redrawn from (Chisti, 2008). .....	15
Figure 6: Electromagnetic spectrum with detail spectral pattern of visible and near infrared light useful for photosynthesis adapted from (Carvalho et al., 2011).....	16
Figure 7: Emittance spectrums of: (A) Cool White Fluorescent, (B) Gro-Lux, (C) incandescent, (D) Halogen, (E) AllnGAP II LED(Peak at 643nm) and (F) GaAIAs (Peak at 663nm) lamps compiled from (Anderson, 2003).....	18
Figure 8: Blackbody emission spectral for three lamps at different color temperatures with their emission curves showing the entire spectrum (U.V, Visible and Infrared wavelength) that was reproduced from (MacIsaac et al., 1999).....	20
Figure 9: Schematic diagram of the typical ratios of radiated energy and heat losses redrawn from (USHIO America, 2018).....	21
Figure 10: Schematic of density variation in a rectangular thermosiphon loop with a low level heated section and a high level heat sink redrawn from (Budihardjo et al., 2007).....	25
Figure 11: Schematic of the various natural circulation loops redrawn from (Zvirin, 1982). .....	25
Figure 12: Schematic of the flow diagram adopted for the adopted methodology for this study.	35
Figure 13: Schematic of geometrical development for novel Thermosiphon PBR.....	37
Figure 14: Schematic diagram of thermosiphon PBR's considered design parameters.....	39
Figure 15: Schematic diagram of the experimental setup: (1) Thermocouples, (2) Data acquisition unit, (3) Computer, (4) Thermal insulation, (5) Halogen lamps, (6) Cooling water outlet, (7) Cooling water inlet, (8) Cooling sections, (9) Rotameter (10) Water chiller, (11) Reservoir, and (12) Submersible water pump.....	43

Figure 16: Schematic view of light radiating the TBPR. The front surface ( $z = 0$ ), to the rear surface ( $z = 1$ ), with $A$ , $I_0(\lambda)$ , $I_z(\lambda)$ , and $q(I)$ being the irradiated area, incident radiant illumination, radiant illumination at any point $z$ , and volumetric sensible heat generated at that point $z$ within the riser respectively. ....	45
Figure 17: Photograph of the thermosiphon PBR in full operation for heat transfer analysis with the indicated positions of measuring position.....	48
Figure 18: Schematic of the thermosiphon PBR's heating and cooling curve illustrating all the various sections where the heat transfer equations are applied .....	49
Figure 19: Schematic of thermosiphon PBR's cooling curve illustrating the application of newton's law of cooling for modeling the riser's heat transfer coefficient .....	50
Figure 20: Schematic diagram of the halogen lamp's emission spectral in the photosynthetically active region with the shared area showing the region for numerical computation of the radiant flux density.....	51
Figure 21: Schematic diagram of the box model applied to the photosynthetically active region of the halogen lamp spectrum .....	52
Figure 22: Photograph of (A) active and (B) inactivated <i>Rhodospseudomonas palustris</i> under a light microscope with a magnification of $40\times$ .....	53
Figure 23: Photographs of (A) <i>Rhodospseudomonas palustris</i> incubated on agar and (B) planktonic <i>Rhodospseudomonas palustris</i> biomass used for all experimental testing.....	54
Figure 24: Schematic diagram for the estimation of local flow velocity through the riser section .....	55
Figure 25: Schematic diagram for the estimation of biomass settling rate.....	56
Figure 26: Photograph of the experimental setup illustrating the estimation of biomass settling	57
Figure 27: (A) and (B) are the 3D and 2D Thermosiphon PBR reactor geometries while (B) and (C) are the element meshing used at the top and bottom sections of the reactor respectively .....	59
Figure 28: Biomass calibration curve of <i>Rhodospseudomonas palustris</i> used to convert absorbance to biomass. Reproduced from the original experimental graph established by (J.P. du Toit, 2017).....	61
Figure 29: Blackbody radiation curve of halogen lamp used as solar simulators at a color temperature of 2900K .....	63

Figure 30: The box model applied to the photosynthetically active part of the Halogen lamp emission spectrum.....	64
Figure 31: Linear regression between absorbance ( $A_b$ ) and biomass concentration ( $X$ ) at various wavelength (400 to 900 nm) .....	66
Figure 32: Spectral extinction coefficient of <i>Rhodospseudomonas palustris</i> measured at five different biomass concentrations from 400 to 900 nm .....	67
Figure 33: Temperature of thermosiphon PBR as a function of time for the three thermocouple sensor positions. Experimental data (average temperature, $T_{av}$ and stabilization temperature, $T_{stab}$ ): from startup to thermal equilibrium indicated with symbols while theoretical curve (model); illumination switch off after 15000 s indicated with a solid line.....	69
Figure 34: Temperature of the hot water in thermosiphon PBR as a function of times for the three thermocouple sensor positions. The experimental data (average temperature, $T_{av}$ ) and theoretical curve (model) are indicated with symbols and lines respectively. ....	70
Figure 35: Temperature contours of CFD steady state simulations showing the temperature notation points, which correspond to the thermocouple positions in the experimental set-up.....	72
Figure 36: Temperature contours distribution with magnified areas of high temperature gradient within the thermosiphon PBR's CFD simulation .....	74
Figure 37: Velocity vectors of the CFD simulations showing the direction of flow due to thermosiphoning .....	75
Figure 38: Velocity contours of the CFD simulations showing the two velocity notation points and the riser's flow profile.....	77
Figure 39: Flow visualization photographs of the TPBR at intervals of 15s, operating under 0.5 $Kgm^3$ intervals under for active and inactive bacterial cells with pink to blue color dissipation showing indicating fluid flow through the riser.....	81
Figure 40: Flow visualization photographs of 45s and 60s compared with CFD simulation results .....	84
Figure 41: Flow visualization photograph of the storage and mixing tank sections compared with CFD simulation results .....	85
Figure 42: Heating rate: startup to steady temperature-time profile for active and inactive bacterial cells within the thermosiphon PBR and under the same operating conditions. ....	86

Figure 43: Biomass circulation rate for active and inactive *Rhodopseudomonas palustris* bacterial cells with the error bars representing the standard deviations of three repeats..... 89

Figure 44: Photograph of the ANSYS workbench environment used throughout the simulation process of this wor ..... 108

Figure 45: photograph of the scaled residuals used throughout the simulation process of this work ..... 109

Figure 46: photograph of the final scaled residuals used for the simulation process of this work ..... 110

## LIST OF TABLES

Table 1: The various growth modes of purple non sulfur bacteria (Deo et al., 2012a) .....	8
Table 2: Various photobioreactor designs, light penetration depths and their reported productivity redrawn from (Janssen et al., 2003) .....	12
Table 3: Major types of artificial lights and their photonic features redrawn from (Carvalho et al., 2011) .....	17
Table 4: Summarize emissivity factors for incandescent lamps at different operating temperatures .....	21
Table 5: Relative performance of the different experimental tool, reproduced from (Joshi et al., 2009). .....	32
Table 6: Experimental tools for structure characterization, reproduced from (Joshi et al., 2009). .....	33
Table 7: TPBR Critical system design parameters .....	39
Table 8: Optimized geometrical parameters for TPBR prototype construction .....	42
Table 9: Mesh quality details .....	58
Table 10: Thermophysical properties of water (Lide, 2003) .....	58
Table 11: Summary of average weighted radiant flux density numerically computed with the box model.....	64
Table 12: Spectral attenuation parameters of <i>Rhodospseudomonas palustris</i> .....	66
Table 13: Comparison of measured and CFD simulated temperatures .....	83
Table 14: Comparison of measured and CFD simulated velocities.....	83
Table 15: Results of the biomass concentration calculations for active <i>R. palustris</i> .....	115
Table 16: Results of the biomass concentration calculations for inactivated <i>R. palustris</i> .....	116



## NOMENCLATURE

<b>SYMBOLS</b>	<b>DESCRIPTION</b>	<b>UNITS</b>
$V_1$	Volume of cylindrical tank	<i>mm</i>
$V_2$	Volume of truncated cone	<i>mm</i>
$V_3$	Volume of downcomer	<i>mm</i>
$V_4$	Volume of riser	<i>mm</i>
$V_5$	Volume of upriser	<i>mm</i>
$V_T$	Total volume	$mm^3$
$D_t$	Tank diameter	<i>mm</i>
$D_d$	Downcomer diameter	<i>mm</i>
$H_{t1}$	Height of top tank	<i>mm</i>
$H_{t2}$	Height of bottom tank	<i>mm</i>
$H_t$	Height of tank	<i>mm</i>
$H_c$	Height of cooler	<i>mm</i>
$H_d$	Height of downcomer	<i>mm</i>
$BA$	Bend allowance	<i>mm</i>
$L_r$	Length of upriser	<i>mm</i>
$I_z(\lambda)$	Point irradiance	$W/m^2$
$I_0(\lambda)$	Surface irradiance	$W/m^2$
$K_0$	Overall extinction coefficient	$m^{-1}$
$K_w$	Water extinction coefficient	$m^{-1}$
$K_b$	Bacterial extinction coefficient	$m^2/kg$
$X$	Biomass concentration	$Kg/m^3$
$Z$	Light path length	<i>m</i>
$q$	Volumetric heat generation	$W/m^3$
$Q_c$	Natural convection lost to water	<i>W</i>
$\dot{V}$	Volumetric water flow rate	$Kg/s$
$C_p$	Specific heat capacity of water	$JKg^{-1}K^{-1}$
$\dot{Q}_{lost}$	Rate of heat lost by convection	$K/s$
$\dot{Q}_{lights}$	Rate of heating by halogen lamps	$K/s$

---

$T_{stab}$	Stabilization temperature	$K$
$T_s$	Hot water temperature	$K$
$T_\infty$	Ambient temperature	$K$
$T_{w,out}$	Outlet water cooling temperature	$K$
$T_{w,in}$	Inlet water cooling water temperature	$K$
$V$	Volume of water	$m^3$
$m$	Mass of water	$Kg$
$t$	Time	$s$
$Z_{curvette}$	Sample thickness	$m$
$A_c$	Area of cooling section	$mm^2$
$h_c$	Heat transfer coefficient of cooling section	$J/s.K$
$A_r$	Area of riser section	$m^2$
$h_r$	Heat transfer coefficient of cooling section	$J/s.K$
$h$	Planks constant	
$c$	Speed of light in air	
$k$	Boltzmann constant	$J/K$
$\lambda$	Wavelength	$mm$
$\rho$	Density of water	$Kg/m^3$
$\beta$	Thermal expansion coefficient	$K^{-1}$
$\epsilon$	Photon energy content	$J$
$\nu$	Wavelength frequency	

---

# CHAPTER ONE

## INTRODUCTION

### 1.1 BACKGROUND AND MOTIVATION

Despite the biotechnological developments and technical advances in closed photobioreactor (PBR) design as alternatives for open systems, almost all the PBR designs have been customized for microalgae culture and very little to do photosynthetic bacteria and biohydrogen production. This has mainly been driven by the environmental concerns of fossil fuels (Basak, Jana, & Das, 2016; Chisti, 2008; Pilon, Berberoğlu, & Kandilian, 2011), and less economic viability, which are to be addressed through minimization of the operation and production costs with efficient designs that are scalable for commercial purposes (Gómez-Pérez, Espinosa, Montenegro Ruiz, & van Boxtel, 2015; Gupta, Lee, & Choi, 2015a; Soman & Shastri, 2015). As a result, more development still needs to be done on system designs, especially as there is often a significant amount of energy consumption involved in supplying aeration and agitation by mechanical/or pneumatic devices (Acien Fernández, Fernández Sevilla, & Molina Grima, 2013; Sierra et al., 2008). That aeration and agitation energy is meant to achieve the main goal of increasing biomass productivity by improving mass transfer, microbial cell suspension, and eliminating the light and nutrient gradients through enhanced mixing (Acien Fernández et al., 2013; Reyna-Velarde, Cristiani-Urbina, Hernández-Melchor, Thalasso, & Cañizares-Villanueva, 2010). However, the mixing energy often results to a reduced overall efficiency (Sierra et al., 2008; Wang, Lan, & Horsman, 2012; Wheaton & Krishnamoorthy, 2012). As well as, hydrodynamic stress and physical cell damage due to high mixing speeds (Acien Fernández et al., 2013; Sierra et al., 2008; Wang et al., 2012) which intend restricts cell growth and metabolic activities. Overall, it impacts the material, operational and production costs, up to *circa* 80% of total costs (Gómez-Pérez et al., 2015; Zhang et al., 2015).

On the other hand, solar radiation, which is the renewable resource driving the microbial metabolic activities of these photosynthetic microorganisms is however currently only exploited for photosynthetic purposes within PBRs (Krujatz et al., 2015). Even when implemented, about 85% of the absorbed solar radiation is still been wasted as metabolic heat and fluorescence (Akkerman, Janssen, Rocha, & Wijffels, 2002; Anderson, 2003; Carvalho, Silva, Baptista, & Malcata, 2011). The thermal effect is even more significant for photosynthetic bacteria like

*Rhodospseudomonas palustris* whose absorption is in the visible (400-700) and near infrared (700-900) segment of the electromagnetic spectrum (Akkerman et al., 2002; Krujatz et al., 2015). Meanwhile, temperature control mechanisms, genetic engineering of the pigment absorbing molecule, symbiotic culturing, and advance light delivery system (Carvalho et al., 2011; Murphy & Berberoğlu, 2011) have been recommended by several studies to overcome this bottleneck of excess metabolic heat and fluorescence. However, no one to the best of the author's knowledge has recommended or attempted to design a PBR which exploits the light absorption of these photosynthetic bacteria, recycles the generated wasted and fluorescence heat, to power the PBR's mixing through natural convection by implementing the thermosiphon effect.

The concept of utilizing the heat generated during light absorption in the PBR for mixing shows merit, since the thermosiphoning effect has already been applied in solar water heating systems (SWHS) with satisfactory mass flow rates of  $5.6 \times 10^{-3}$ -  $6.9 \times 10^{-3}$  kg/s (Budihardjo, Morrison, & Behnia, 2007),  $1.8 \times 10^{-4}$  Kg/s (Freegah, Asim, & Mishra, 2013), 30 kg/s (Morrison & Braun, 1985; Ogueke, Anyanwu, & Ekechukwu, 2009), and velocity flow rates of  $3.3 \times 10^{-2}$  m/s (Morrison, Budihardjo, & Behnia, 2005), 0.8 m/s (Gandhi, Sathe, Joshi, & Vijayan, 2011). It is notable that these mass and velocity flow rates are powerful enough to carry microbial cells in free suspension. Mindful of the fact that these photosynthetic bacteria are not susceptible to shear stress due to their dimensions being much more less than the microscale of turbulence generated in most PBRs including stirred tank reactor (Krujatz et al., 2015). In addition to, (i) their very versatile metabolic repertoire, (ii) high substrate to product conversion, (iii) their ability to degrade waste organics in bioremediation processes, (iv) the lack of oxygen evolving ability, which prevents inhibition of the hydrogen evolving enzymes and (v) their ability to utilize a wide spectrum of light (Basak & Das, 2007). They are an exemplary candidate photosynthetic microorganism to be cultivated in such a new bioreactor since as they do not require gas sparging but are able to treat recalcitrant waste-water streams.

Therefore, it is hypothesize that the high absorption efficiency will enhance the thermosiphoning within the bioreactor due to the high sensible heat generation on the collectors (riser section) and subsequent subcooling at the sink (cooler section). In application, such a thermosiphon photobioreactor will be closed system and void of aeration since the bacterium is anoxygenic, and does not required carbon dioxide during its heterotrophic growth mode (Basak et al., 2016;

Deo, Ozgur, Eroglu, Gunduz, & Yucel, 2012a; Dwi & Reksodipuro, 2009; Nogi, Akiba, & Horikoshi, 1985). As a result, it will cultivate the photosynthetic bacteria while minimizing the energy requirements for aeration and agitation bringing about a more economically feasible process with important energy and cost savings (Gómez-Pérez et al., 2015; Gupta, Lee, & Choi, 2015b).

The unavailability of literature on such a thermosiphon PBR design imposes some complexity in the proof of concept, thereby requiring many prototypes to be built and tested, since as the performance of SWH systems is affected by the interaction of multiple factors namely (i) design parameters, (ii) operating conditions, and (iii) metrological data (Shariah & Shalabi, 1997) which are inconsistent by varying from country to country. However, Computational Fluids Dynamic modeling (CFD) is a very powerful and useful tool for conveniently and accurately simulating, evaluating and analyzing the internal hydrodynamics, irradiance characteristic of photobioreactors by numerically solving the Navier-Stokes equations (Pires, Alvim-Ferraz, & Martins, 2017). This was implemented in this thesis to evade the expensive, time-consuming, trial and error method but still yielding valuable insights into the design, operation, scale up and optimization of these thermosiphon PBR systems.

The advent of low cost, high speed computers coupled with the rapid progress in parallel computing and development of several commercial CFD codes has enabled scientists, chemical, process and mechanical engineers to establish the modeling methodology for thermosiphon and natural convection systems. However, most of these investigations make use of a simplified boundary condition such as uniform constant wall temperature and surface flux (Alizadehdakhl, Rahimi, & Alsairafi, 2010; Budihardjo et al., 2007; Fadhl, Wrobel, & Jouhara, 2013; Freegah et al., 2013; Gandhi et al., 2011; Louisos, Hitt, & Danforth, 2013; Malik, Shah, & Khushnood, 2013; Pilkhwal et al., 2007a) as the heating source on the absorber/collector sections. This approach works well under certain experimental conditions, such as electric heating, nuclear fuel elements, heat exchangers, boiling water heating, and 'black pipe' solar water heaters. However, such modeling approaches are not well suited for the proposed thermosiphon PBR since it experiences non-uniform volumetric heating from microbial light absorption due to light penetration at the collector/absorber sections, which must be accounted for by solving the relevant radiation transfer equation.

The resulting CFD simulations (vector, line, contour, and surface plots) have limited value without experimental validation, mainly due to the complexity of the system being studied. In recent years, intrusive and nonintrusive techniques (Joshi, Tabib, Deshpande, & Mathpati, 2009) have been used in the identification and characterization of flow structure under Experimental Fluid Dynamics (EFD). A nonintrusive technique referred to as ‘image maker method’ based on the underlying principle of measuring the displacement marked by fluid particles in consecutive images has been widely used for flow visualization, although less frequently for quantitative characterization. On the other hand, thermocouple temperature reading located on a center pipe positions have been widely used for the experimental validation of CFD modeling of thermosiphon and natural convection related studies (Alizadehdakhel et al., 2010; Budihardjo et al., 2007; Fadhl et al., 2013; Freegah et al., 2013; Gandhi et al., 2011; Louisos et al., 2013; Malik et al., 2013; Pilkhwal et al., 2007a) Therefore, The image marker technique and the thermocouple center pipe temperature readings on the experimental setup were adopted for this thesis to validate the passive fluid flow and thermal performance of the CFD simulation results.

Overall, the aim of the project was to design, fabricate, model and evaluate a photobioreactor that: (i) achieves natural fluid circulation by the thermosiphon effect arising from temperature differences due to microbial light absorption, (ii) maintains bacterial cells in free suspension and (iii) has adequate mass and heat transfer. The development of such a reactor will allow for reduced mixing energy costs, and be particularly well-suited to implementation with anaerobic photofermentative organisms, such as *Rhodospseudomonas palustris*.

## 1.2 RESEARCH OBJECTIVES AND QUESTIONS

### 1.2.1 OBJECTIVES

The main aim of this research is to use CFD modeling and experiments to support the development of a thermosiphon photobioreactor, where fluid circulation is achieved by temperature-induced density differences arising from light absorption. The aim of the larger project, of which this work forms a part, is to apply the TPBR for waste-water treatment by a candidate photosynthetic bacterium like *Rhodospseudomonas palustris* which is extremely metabolically diverse, and able to consume a large variety of potentially recalcitrant wastewater components, while simultaneously producing high purity hydrogen. The main aim was achieved by addressing the following five specific objectives.

- To develop a reactor geometry based on the passive thermosiphon fluid flow and construct it for testing.
- To develop a numerical model and evaluate the passive fluid flows within the reactor geometry using ANSYS-workbench version 17.2.
- To validate the TPBR design by comparing how closely the experimental model corresponds to the CFD model.
- To investigate microbial light absorption, and heat transfer rates, analysis within the TPBR.
- To establish proper operating conditions for the cultivation of photosynthetic bacteria using this TPBR.

### 1.2.2 RESEARCH QUESTIONS

- How does the light to heat conversion affect the TPBR's passive fluid flow and mixing while operating under diphasic systems?
- Can the internal power from natural fluid circulation prevent cell sedimentation and enable continuous suspended culturing of photosynthetic bacteria within the TPBR?
- To what extent does the numerical model predict the experimental scenario?

### 1.3 THESIS OVERVIEW

Chapter one is the introduction chapter which covers the background and motivation, research objectives and questions, and the thesis overview.

Chapter two is the literature review chapter and covers photofermentation by purple non-sulfur bacteria, photobioreactor designs and types, light availability, transmission and simulation, thermosiphon loops, design and their applications, Computational fluid dynamics modeling (CFD) and experimental validation.

Chapter three is the material and methods chapter which covers the research design, thermosiphon photobioreactor design consideration, thermosiphon photobioreactor geometry,

experimental fluid dynamic studies, Computational Fluid Dynamics (CFD) modeling, and analytical method.

Chapter four is the result and discussion chapter which includes spectral parameters used for CFD modeling, CFD simulation results, flow visualization results, validation results, effect of light absorption on heating rate, and the effect of light absorption on thermosiphoning cells.

Chapter five is the conclusion and recommendation chapter covering the conclusions and recommendations.



## CHAPTER TWO

### LITERATURE REVIEW

#### 2.1 PHOTOFERMENTATION BY PURPLE NON-SULFUR BACTERIA

Purple non-sulfur bacteria (PNSB) are a group of diverse photosynthetic microorganism which can use reduced carbon sources as their electron donor, and are known to be facultative anoxygenic phototrophs belonging to the class of *Alphaproteobacteria* with many biological hydrogen producing species like *Rhodobacter sphaeroides*, *Rhodobacter capsulatus*, *Rhodospirillum rubrum* and *Rhodopseudomonas palustris* etc (Basak et al., 2016; Deo et al., 2012a; Dwi & Reksodipuro, 2009; Nogi et al., 1985). Their natural habitat is at the anaerobic layers of ponds, lakes and lagoons, far below the chlorophyll containing oxygenic phototrophs, as illustrated in Figure 1, resulting in them being very metabolic versatile by thriving in conditions where similar organisms cannot function (Dwi & Reksodipuro, 2009).

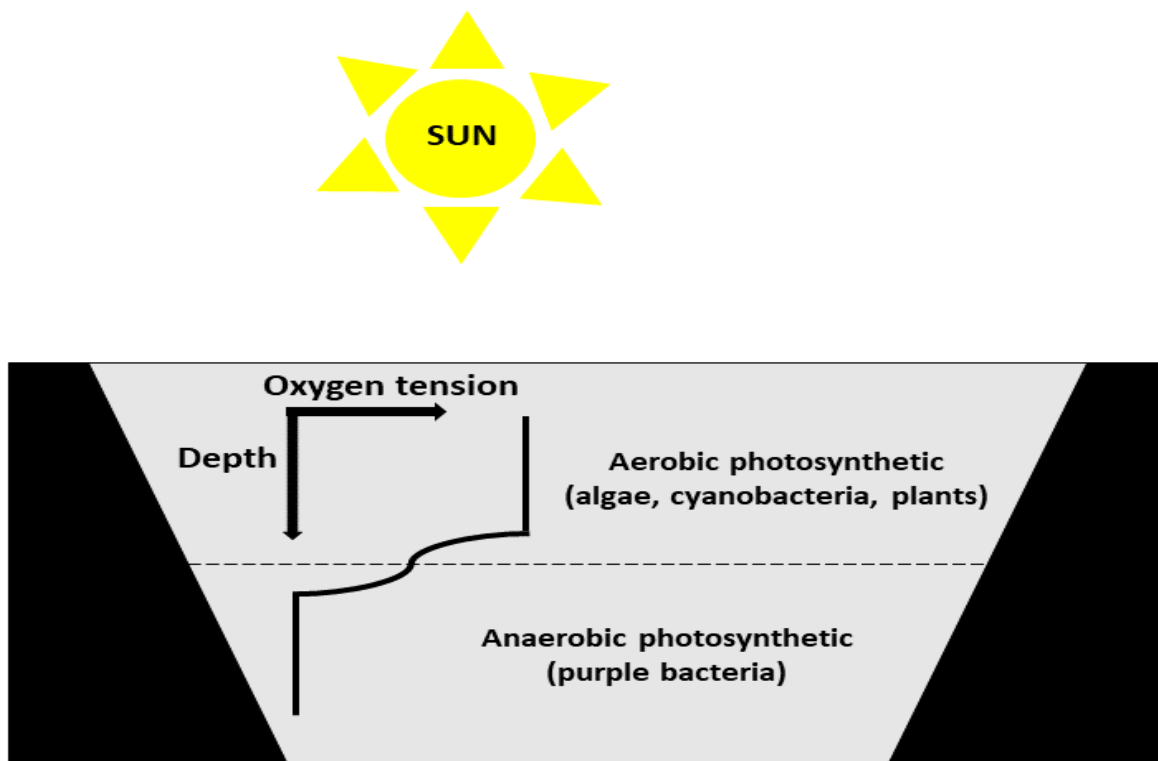


Figure 1: Schematic diagram of purple photosynthetic bacteria habitat position in their natural habitat redrawn from Dwi & Reksodipuro (2009)

They are capable of using solar energy to oxidize organic compounds like (i) sugars (sucrose and glucose), (ii) short chain organic acids (acetic, butyrate, fumarate, formate, lactate, malate, propionate and succinate), (iii) amino acids, and even (iv) polyphenols (Deo, Ozgur, Eroglu, Gunduz, & Yucel, 2012b; Hallenbeck & Benemann, 2002; Kapdan & Kargi, 2006; Pilon et al., 2011) to generate electrons which are competed for by (i) CO<sub>2</sub> fixation, (ii) N<sub>2</sub> fixation (and concomitant H<sub>2</sub> production), (iii) polyhydroxybutyrate (PHB) biosynthesis, thereby resulting in their metabolic growth mode being very versatile. This versatility has attracted many researchers towards metabolic regulation of carbon, nitrogen, and energy in recent times (Deo et al., 2012b). This is summarized in Table 1, where the photoheterotrophic growth represents the only growth mode which results to directly hydrogen production.

Table 1: The various growth modes of purple non sulfur bacteria (Deo et al., 2012a)

<b>Mode of growth</b>	<b>Carbon source</b>	<b>Energy source</b>	<b>Remarks</b>
Photoautotrophic	CO <sub>2</sub>	Light	CO <sub>2</sub> fixation and H <sub>2</sub> is used as the proton donor
Aerobic respiration	Organic carbon	Organic carbon	O <sub>2</sub> is the terminal electron acceptor
Photoheterotrophic	Organic carbon	Light	The only growth mode that results in H <sub>2</sub> production
Anaerobic respiration/chemoheterotrophic	Organic carbon	Organic carbon	Requires a terminal electron acceptor other than O <sub>2</sub> like N <sub>2</sub> , H <sub>2</sub> S or N <sub>2</sub>
Fermentation/anaerobic, dark	Organic carbon	Organic carbon	

The biological hydrogen produced is often regarded as the future's energy because it has a high energy yield of 122 kJ/g, which is 2.75 times greater than hydrocarbon fuels (Argun & Kargi, 2010; Kapdan & Kargi, 2006), highest amount of energy density (143 GJ/ ton) (Basak et al., 2016; Gilbert, Ray, & Das, 2011), emits only water and not carbon dioxide during combustion with oxygen (Basak et al., 2016; Gilbert et al., 2011), produced under ambient temperature and atmospheric pressure (Gilbert et al., 2011), and easily used in fuel cells for direct electricity generation (Deo et al., 2012a; Kapdan & Kargi, 2006).

The biological production of hydrogen by PNSB requires light as an energy source, electron donating substrate (oxidize organic compounds) and a biological catalyst (nitrogenase) to

convert light into hydrogen by combining the protons and electrons (Akkerman et al., 2002; Deo et al., 2012b; Hallenbeck & Benemann, 2002). Their photoheterotrophic growth and bacterial multiplication has generally been characterized into five main phases namely (i) lag phase, (ii) exponential growth phase, (iii) linear growth phase, (iv) stationary phase, and (v) death phase (Anderson, 2015; Clarke, 2013) as illustrated in Figure 2.

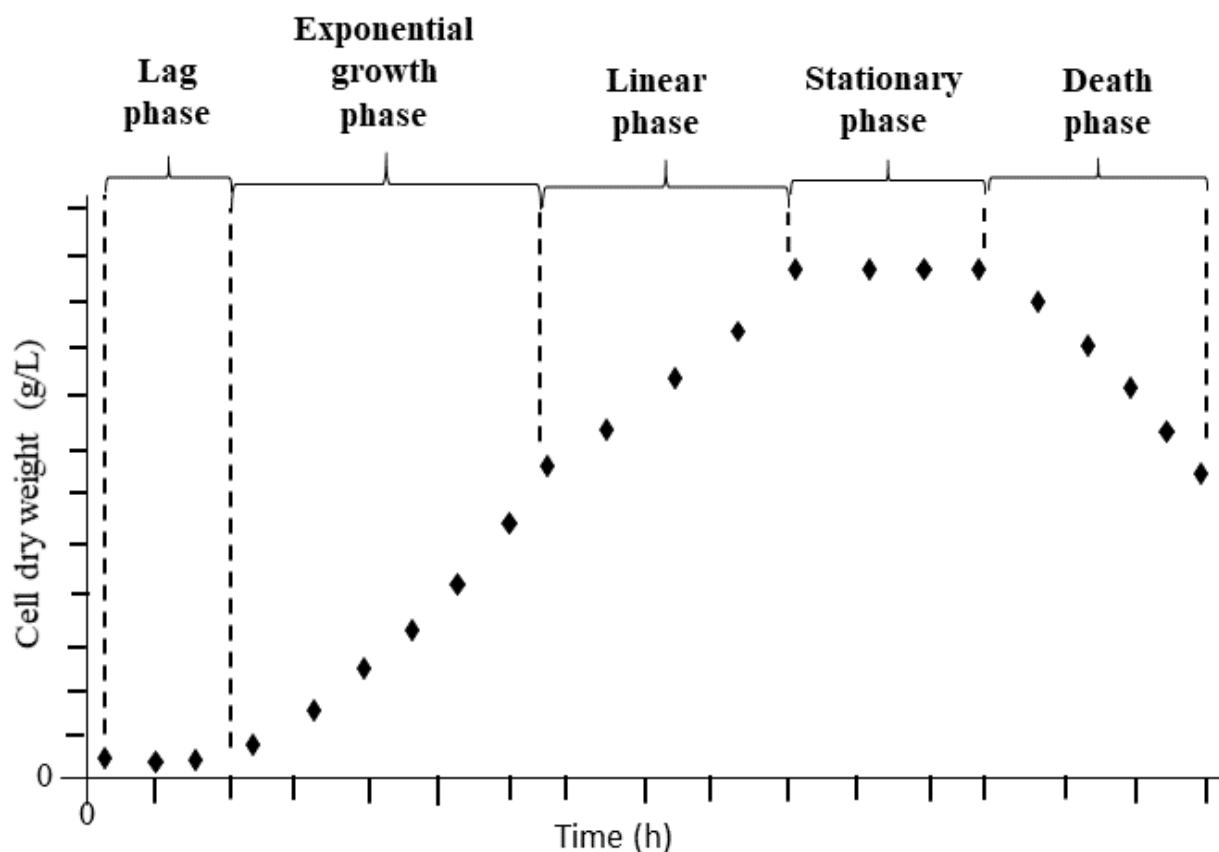


Figure 2: Schematic diagram of microbial population growth redrawn from (Clarke, 2013)

Depending on the PNSB species, the lag phase (i) maybe brief or nonexistent because the microbial cells are still adapting to their new environment and this lag phase is often eliminated by using actively growing inoculated cultures (Anderson, 2015; Clarke, 2013). After adapting to their new environments, the bacterial cells experience growth acceleration in the (ii) exponential growth phase by multiplying exponentially with time due to the abundant nutrients and light supply (Anderson, 2015; Clarke, 2013). As the bacterial cell concentration increases, the light supply as well as the nutrients begins to decrease leading to a (iii) linear growth phase and this decrease in light is cause by mutual shading whereby bacterial cells closer to the light source

block light rays from going to farther away bacterial cells (Anderson, 2015; Clarke, 2013). As the growth progresses, bacterial cells continue to deplete nutrients and produce inhibitory metabolic products causing growth to slow down leading to a (iv) stationary phase, where the growth and death of bacterial cells are constant (Anderson, 2015; Clarke, 2013). The final (v) death phase is often encountered when the bacterial cells runs out of sufficient nutrients (starvation) to maintain population or stress is significant (Anderson, 2015; Clarke, 2013).

## 2.2 PHOTOBIOREACTORS: DESIGNS AND TYPES

The cultivation of photosynthetic microbial cells for fuel production (popularly known as third generation biofuels) typically takes place within technical systems called photobioreactors which differ from classical bioreactors because of the additional light supply requirements to the classical growth substrates and can take the form of an open system such as natural waters (ponds, lakes, lagoons, etc.) and artificial ponds (raceway ponds) (Gupta et al., 2015a; Krujatz et al., 2015; Kunjapur & Eldridge, 2010; Pires et al., 2017; Pulz, 2001; Tamburic, Zemichael, Crudge, Maitland, & Hellgardt, 2011a) or an enclosed transparent glass or plastic container, cut off from the atmosphere (such as stirred tank PBRs, tubular PBRs, vertical column PBRs and flat plate PBRs) (Gupta et al., 2015a; Krujatz et al., 2015; Kunjapur & Eldridge, 2010; Pires et al., 2017; Pulz, 2001; Tamburic, Zemichael, Crudge, Maitland, & Hellgardt, 2011b).

Open systems are simpler with low capital, operational and production costs (Gupta et al., 2015a; Krujatz et al., 2015; Pires et al., 2017; Pulz, 2001) but cannot be applied for biohydrogen production because of the oxygen inhibition to the nitrogenase activity (biocatalyst for H<sub>2</sub> production) (Basak et al., 2016; Deo et al., 2012a; Dwi & Reksodipuro, 2009; Ji, Legrand, Pruvost, Chen, & Zhang, 2010; Kapdan & Kargi, 2006; Nogi et al., 1985) and even if the very little biohydrogen is produced, it will escape into plain air. Other major drawbacks for the none photoheterotrophic growth mode in open systems includes (i) significant evaporative loss, (ii) large land requirements (iii) carbon dioxide (CO<sub>2</sub>) diffusion to the atmosphere, (iv) poor light transfer and utilization by photosynthetic microbial cells, (v) contamination and pollution by predators or other fast growing heterotrophs, (vi) poor mass transfer rates due to inefficient mixing/stirring mechanism, and (viii) uncontrolled growth parameters such as temperature, pH

levels, and nutrient supplies (Gupta et al., 2015a; Krujatz et al., 2015; Kunjapur & Eldridge, 2010; Pulz, 2001; Tamburic et al., 2011b).

The performance indicator for these enclosed photobioreactor systems is not only determined by their ability to provide growth requirements but a measure of their ability to balance these growth parameters. This often comes at a greater expense of high capital and operational cost couple to the high maintenance and limited scalability, resulting to their commercial scale-up not often regarded as economically feasible (Posten, 2009). Therefore in order to effectively design and operate photobioreactors for converting solar energy into biomass by photosynthetic microorganisms, careful understanding of the coupling between the (i) biological response: the physiological demands of the microbial cell for growth and product development with regards to the value of the product and their field of application, and (ii) environmental considerations: one applied parameter does not adversely affect the other parameter (Posten, 2009). As a result, photobioreactors are categorized according to reactor geometries with some standard designs being (i) vertical column (ii) tubular and (iii) flat plate reactors as shown in Figure 3, Figure 4 and Figure 5 (Kapdan & Kargi, 2006; Kunjapur & Eldridge, 2010; Wang et al., 2012)

These photobioreactor designs are constrained by the light regime inside of them which in turn predominantly affects their productivity (Janssen, Tramper, Mur, & Wijffels, 2003). The light regime is characterized by a photic zone with intense light at the PBR's surface and a dark zone within the interior of the PBR (Acién Fernández, García Camacho, & Chisti, 1999; Janssen et al., 2003). The photic zone has been defined as the depth at which 90% of the incoming photon flux is absorbed and referred to as the light penetration depth ( $d_p$ ) (Janssen et al., 2003). This light penetration depth and the biomass concentration in the culture are the two predominant factors which determine the light gradient of the PBR (Janssen et al., 2003). An increase in the light penetration depth often leads to an increase in the PBR's surface to volume (S/V) ratio especially for tubular and airlift PBRs (Acién Fernández et al., 1999). Therefore, for the PBR to intercept sufficient light, a high S/V ratio is a prerequisite (Posten, 2009). Hence, the light penetration depth is very significant since as the microorganisms closest to PBR surface are predominantly in contact with light close to the PBR surface walls which is where most of the photosynthesis occurs (Carvalho et al., 2011). Consequently, the photosynthesis rate is inhibited the further away the microorganism is from the PBRs surface walls because light is blocked by mutual

shading of cells via absorption by their pigments and via scattering (Janssen et al., 2003; Posten, 2009). The light penetration depth and productivity for this different photobioreactor designs have been summarized in Table 2.

Table 2: Various photobioreactor designs, light penetration depths and their reported productivity redrawn from (Janssen et al., 2003)

Photobioreactor type	Dimension	Biomass density (g dw $L^{-1}$ )	Photosynthetic Efficiency ( $Y_{dw,E}$ ) <sup>c</sup>
Bubble column and airlift column PBR	Diameter 19.3 cm Height: 2.17-2.32	1.25-2.75	0.84
(a) Internal draft tube	$A_d/A_R = 1.24$		
(b) Split cylinder	$A_d/A_R = 1$		
Airlift column	Diameter 9.6 Height 2m: $A_d/A_R = 0.5$	3.3	0.82
Flat plate PBR	(a) Vertical, width 2.6m (b) Tilted 10-90 facing south, width 2.8 cm	(a) 15-17.5 (b) 5-8	(a) 1.480.84 (b) 10-20
Tubular PBR	Length $2 \times 122.5$ m: $D_{int} : 2.5$ cm	3.5	0.60
Tubular PBR	Length: 90 cm (a) $D_{int} : 2.5$ cm (b) $D_{int} : 5.3$ cm	(a) 3.3-6.9 (b) 2.5 5.1	(a) 0.48-0.63 (b) 0.68-0.95

### 2.2.1 VERTICAL COLUMN PBR

As seen in Figure 3, vertical column PBRs are potentially the simplest of all photobioreactor geometries (Skjånes, Andersen, Heidorn, & Borgvang, 2016). They are frequently used in outdoor large scale growth experiments and generally consist of cylindrical transparent glass or plastics with radii and heights measuring up to 0.2 m and 4 m respectively (Gupta et al., 2015a; Wang et al., 2012). Their heights impose a limitation on mass transfer as carbon dioxide ( $CO_2$ ) gradients can be formed when they exceed 4 m which significantly reduces oxygen ( $O_2$ ) removal thereby inhibiting growth of the culture by starving of  $CO_2$  (e.g. algae culture) and creating pH gradients (Wang et al., 2012). Conversely, they have excellent gas transfer coefficients with very

little shear stress affecting the microbial cells when operated at average superficial gas velocities since mixing is driven by constant motion of bubbles which are very gentle compared to the impellers and other pump driven systems (Skjånes et al., 2016; Wang et al., 2012). The bubble column, internal loop airlift, split column airlift and external loop airlift PBRs are the four major types of vertical column PBR (Wang et al., 2012) as shown in (A), (B), (C), and (D) of Figure 3 respectively.

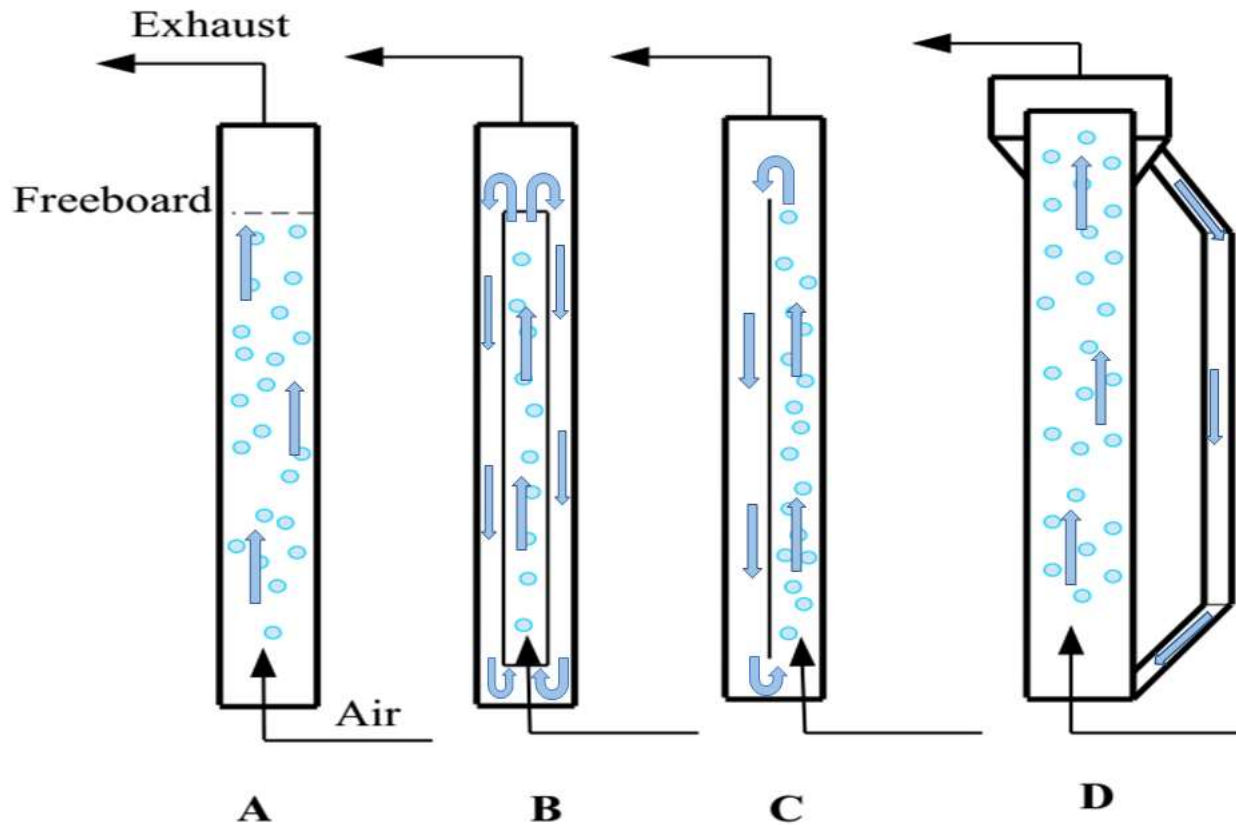


Figure 3: Schematic diagrams of: (A) bubble column PBR, (B) internal-loop (draft-tube) airlift PBR, (C) split column airlift PBR and (D) external loop airlift PBR redrawn from (Wang et al., 2012).

### 2.2.2 FLAT PLATE PBR

As illustrated in Figure 4, flat plate PBRs are often considered the most robust design of PBRs, due to their simple construction. They consist of two transparent sheets joined together making a flat plate reactor which allows any desired light path and microorganism culture to flow between them (Gupta et al., 2015a; Posten, 2009; Wang et al., 2012). These transparent sheets can be

made from glass, Plexiglas or polycarbonate with varying sizes that can measure heights up to 1.5 m and widths of 0.1 m (Akkerman et al., 2002). Flat plate PBRs as well as vertical tubular PBRs do have a high surface area to volume ratio thereby possessing good light utilization (Bangert, 2013; Bitog et al., 2011; Gupta et al., 2015a; Skjånes et al., 2016). On the other hand, the growth of photosynthetic microbial cells in the flat plates PBR poses a common problem of biofouling on the light transfer surfaces thereby lowering light penetration (Gupta et al., 2015a). Depending on the type of mixing employed, flat plate PBRs can be classify into (i) pump driven where the direct mixing and turbulence is provided by the pumping flow of liquids, and (ii) airlift driven where the buoyancy driven mixing and turbulence is provided by the compressed air during aeration (Wang et al., 2012).

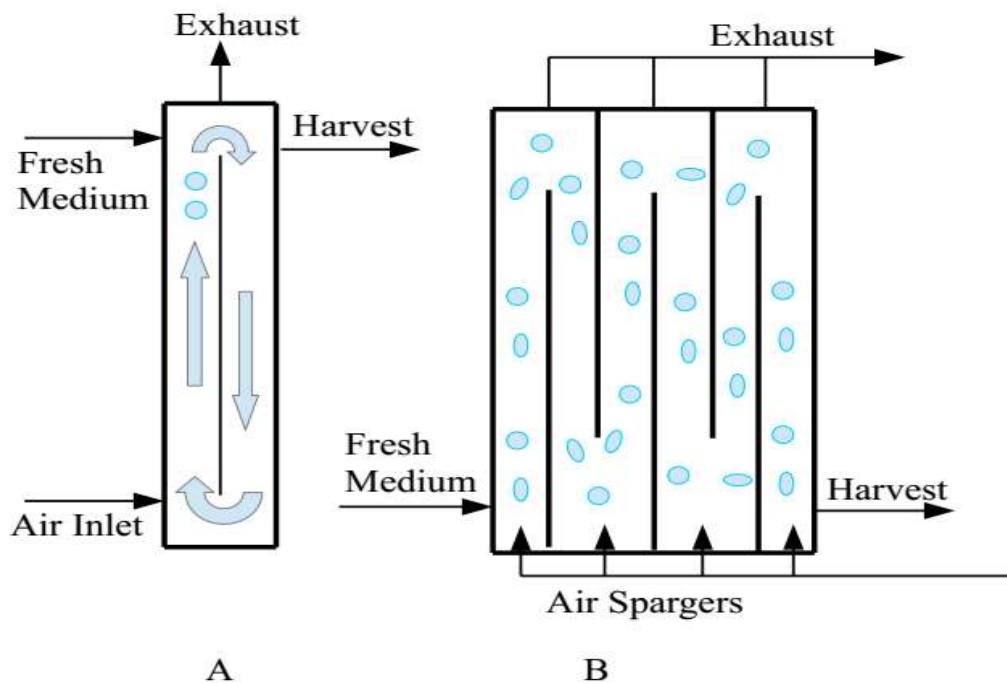


Figure 4: Schematic diagram of the (A) side view of a flat plat PBR, and (B) front view of a pump-driven flat plat PBR redrawn from (Wang et al., 2012)

### 2.2.3 TUBULAR PBR

Illustrated in Figure 5, tubular PBRs are one of the most popular photobioreactor configurations. They are generally constructed from transparent tubing usually made from plastics or glass with either spiral, curved or straight formations and different orientations such as vertical, horizontal or inclined which serves as solar collector for the photosynthetic microbial cells suspending



within the flowing medium (Akkerman et al., 2002; Chisti, 2008; Posten, 2009; Wang et al., 2012). Their diameters are generally not greater than 0.1m in order to allow sunlight penetration through the transparent tubing walls to the culturing medium while being circulated by either aeration or mechanical pumps (Akkerman et al., 2002; Chisti, 2008; Posten, 2009; Wang et al., 2012). The turbulence generated by recirculation using aeration or mechanical pumps needs to be monitored and maintained at low enough levels in order not to induce cell damage due to the formation of micro eddies (Acien Fernández et al., 2013; Bangert, 2013; Wang et al., 2012). Horizontal tubular PBRs do have greater surface area to volume (A:V) ratio compared to their vertical counterparts thereby enabling them to have maximum sunlight exposure due to the solar angle of incidence (Bangert, 2013; Gupta et al., 2015a; Skjånes et al., 2016). As a result, they experience high temperature variation and increased oxygen build-up for microalgae cultures prompting the use of different temperature control techniques such as submerging the array in water, using covers, spraying with water and using heat exchangers (Skjånes et al., 2016; Wang et al., 2012).

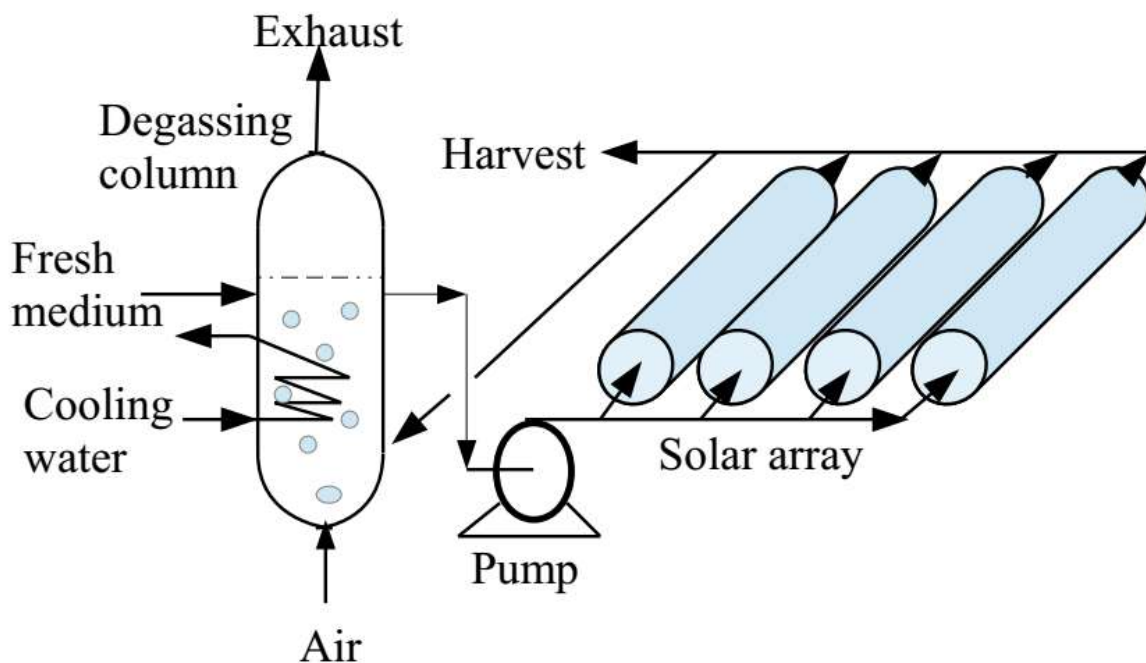


Figure 5: Schematic diagram of a Tubular Photobioreactor with parallel run horizontal tubes redrawn from (Chisti, 2008).

### 2.3 LIGHT AVAILABILITY, TRANSMISSION AND SIMULATION

Light being either a particle (quanta or photon), or wave can be physically referred to as electromagnetic radiation of any wavelength on the electromagnetic spectrum (Anderson, 2015; Carvalho et al., 2011) as illustrated in Figure 6. Light in its natural (sun light) or artificial (light bulb) form is the energy source driving metabolic activities of most photosynthetic microorganism (Pilon et al., 2011; Pires et al., 2017) and unlike other abiotic factors (e.g. temperature, pH, nutrients and gases) (Carvalho et al., 2011; Pires et al., 2017), it's a key process parameter that is often very difficult to control: it cannot be stored, pumped or mixed but is continuously been supplied with a high degree of uncertainty around its stability and uniformity over time and space (Carvalho et al., 2011; Krujatz et al., 2015).

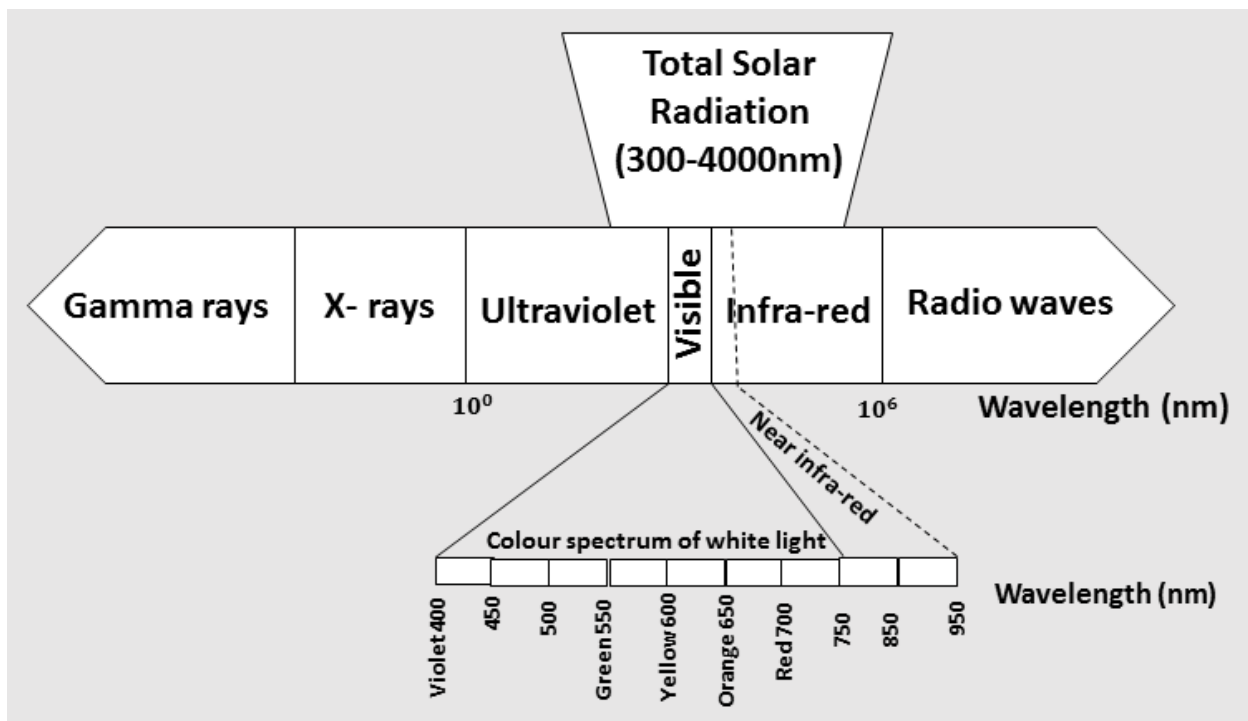


Figure 6: Electromagnetic spectrum with detail spectral pattern of visible and near infrared light useful for photosynthesis adapted from (Carvalho et al., 2011).

Natural light from the sun reaching the atmosphere of the Earth's surface is estimated at  $1.73 \times 10^{17} W$  or  $6.38 \times 10^{19} Wh/year$  (Pilon et al., 2011). The incident solar spectrum varies from geographic location to location and it exhibits dependence on latitude and altitude, weather conditions (e.g. cloud cover), period of the day and year (less in winter and more summer)

(Acién Fernández et al., 1999; Anderson, 2015; Pilon et al., 2011). For these reasons, some geographic locations are more promising for harvesting solar energy than others, with southwest United States, northern Mexico, the Andes, northern and southern Africa, the Middle East, and Australia as promising areas, followed by southern Europe, southern China, South East Asia, Brazil and most of Africa (Pilon et al., 2011).

In application for microbial photosynthesis, growth and subsequent product formation, these instabilities present a big bottleneck and can be minimize with the use of artificial light sources which generate photons in the photosynthetic active regions (PAR) of the electromagnetic spectrum, and are supplied at the appropriate intensity, duration, and wavelength (Anderson, 2015; Carvalho et al., 2011). Some of the commonly used artificial light source for microbial growth includes but not limited to (i) incandescent bulbs, (ii) halogen lamps, (ii) fluorescent lamps (ii) gro-lux fluorescent lamp, (ii) light emitting diodes (LEDs), and (iii) laser diodes (Anderson, 2015; Bitog et al., 2011; Carvalho et al., 2011; Krujatz et al., 2015) as presented in Table 3.

Table 3: Major types of artificial lights and their photonic features redrawn from (Carvalho et al., 2011)

<b>TYPE OF LIGHT</b>	<b>REGION (400-500 nm) OF ENERGY EMISSION</b>	<b>REGION (600-700 nm) OF ENERGY EMISSION</b>	<b>ENERGY CONVERSION TO HEAT</b>	<b>LIFETIME (TYPICAL VALUE)</b>	<b>COST</b>	<b>LUMINOUS EFFICACY (<math>lm/W</math>)</b>
Incandescent bulbs	0.5%	3.8%	Very high	750-2,000 h Degradation of light output with time	Low price	10-18
Halogen lamps	0.3%	3.3%	High	3,000-4,000 h light output level does not diminish over time	Low price	15-20
Fluorescent lamps	25.0%	20.7%	Low	10,000 h duration with degradation of light output along time	10 times more expensive than incandescent bulbs	35-100
Gro-lux fluorescent lamp	18.9%	37.9%	Low	15,000 h duration with degradation of light output along time	3-10 times more expensive than incandescent bulbs	50-70
Light emitting diodes (LEDs)	0.04-0.08%	87.6-98.3%	Very low (below 10%)	35,000-50,000 h duration with degradation of light out along time	2-10 times more expensive than fluorescent lamps	25-64
Laser diodes			Negligible	High quality diode lasers with 100, 000	2 times more expensive than	30-45

As seen in *Figure 7*(A, B, E and F) where most of the light emitted by cool white fluorescent, Gro-lux, AlInGAP II LED and GaAlIAs LED are in the visible region (400-700nm) with combined percentages of 45.56%, 56.87%, 98.42% and 87.59% respectively (Anderson, 2003). This similarity of their light emission spectrums to daylight enables them to be applied extensively for testing different plants and microalgae biomass production rates (Anderson, 2003). However, this is not the case for incandescent and halogen lamps as *Figure 7*(C and D) shows their visible region lamp emittance to be 4.23% and 3.60% respectively (Anderson, 2003). This implies that they are highly inefficient for plants and microalgae photosynthesis since as most of their energy will be converted to heat (long wave radiation of mostly infrared region)(Anderson, 2003). However, they are the favorite choice for photosynthetic bacteria whose absorption is in both the visible and near infra-red region of the electromagnetic spectrum.

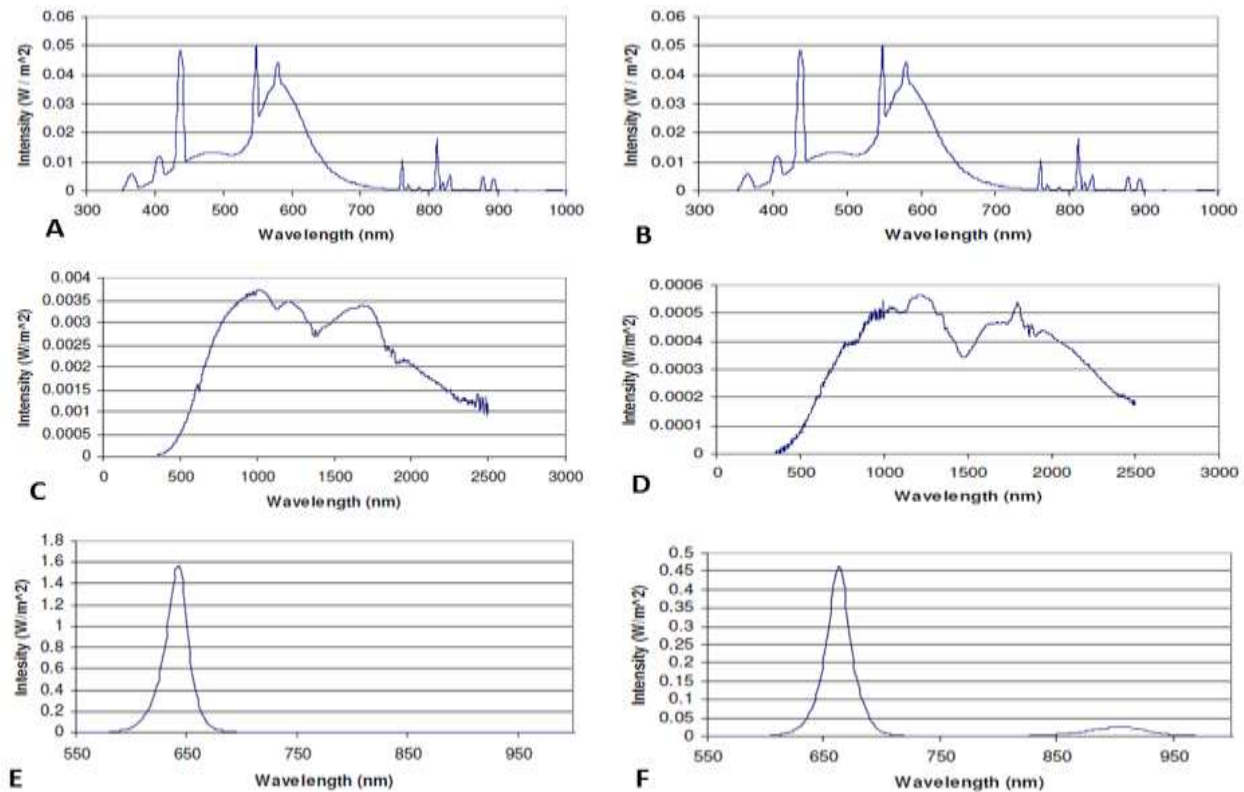


Figure 7: Emittance spectrums of: (A) Cool White Fluorescent, (B) Gro-Lux, (C) incandescent, (D) Halogen, (E) AlInGAP II LED(Peak at 643nm) and (F) GaAlIAs (Peak at 663nm) lamps compiled from (Anderson, 2003)

In designing effective microbial culturing systems to supply the correct-light at the appropriate intensity, duration, and wavelength, a detailed review of the microbial spectral requirements couples to other selection criteria like (i) good reliability, (ii) electrical efficiency, (iii) low heat dissipation, (iv) high durability, (v) reasonable compactness, (vi) low cost, and (vii) long lifetime of the artificial lighting source often needs to be performed (Anderson, 2015; Carvalho et al., 2011). As a result, halogen lamps which continuously convert electrical energy into heat and light of a full spectrum (spectra output), both in quantity and quality thereby perfectly mimicking sunlight were chosen as solar simulators in this thesis. As well, they have been extensively used in laboratory conditions as the best choice for artificial lighting by several other studies pertaining to designing of culturing systems for photosynthetic bacterial growth and biohydrogen production (Jouanneau, Wong, & Vignais, 1985; Krujatz et al., 2015; Ogbonna, Yada, & Tanaka, 1995; D Zhang et al., 2015; T. Zhang, 2013).

Halogen lamps being a type of incandescent bulbs is approximated as blackbodies at an operating temperature of 2900K (MacIsaac, Kanner, & Anderson, 1999). This implies that, all the electrical resistive heating is converted into photonic emission of a quite reddish yellow light (MacIsaac et al., 1999). The resulting radiation distribution for standard incandescent lamps looks like Figure 8 while its spectral exitance  $I(\lambda, T)$  is described by the Planck's radiation law (equation (1)) (Cengel & Ghajar, 2011; MacIsaac et al., 1999). The emitted portions of light as radiant flux density ( $W/m^2$ ) is calculated by numerically computing the area under the generated emission spectral curve,  $A(T)$  (equation (2)) (MacIsaac et al., 1999). In real life, the photonic emission of these incandescent lamps decreases due to losses and reflection at each glass interface of the bulb's glob (Cengel & Ghajar, 2011; MacIsaac et al., 1999). Therefore, they are usually not true blackbodies (but rather producing 'graybody' radiation) whereby the spectrum is like a blackbody of a somewhat different operating temperature. The emissivity factor accounts for these accumulated losses with a typical ratio of the radiated energy and heat loss is illustrated in Figure 9 while Table 4 summarizes some reported emissivity factors.

$$I(\lambda, T) = \frac{2\pi hc^2}{\lambda^5} \frac{1}{e^{-hc/\lambda KT} - 1} \quad (1)$$

Where  $I(\lambda, T)$  is flux of power per unit area per unit wavelength and known as the spectral exitance,  $\lambda$ ,  $T$ ,  $h$ ,  $c$ , and  $K$  are the wavelength, color temperature (in K), Planck's constant, speed of light in a vacuum, and Boltzmann's constant.

$$A(T) = \int_0^{\infty} I(\lambda, T) d\lambda \quad (2)$$

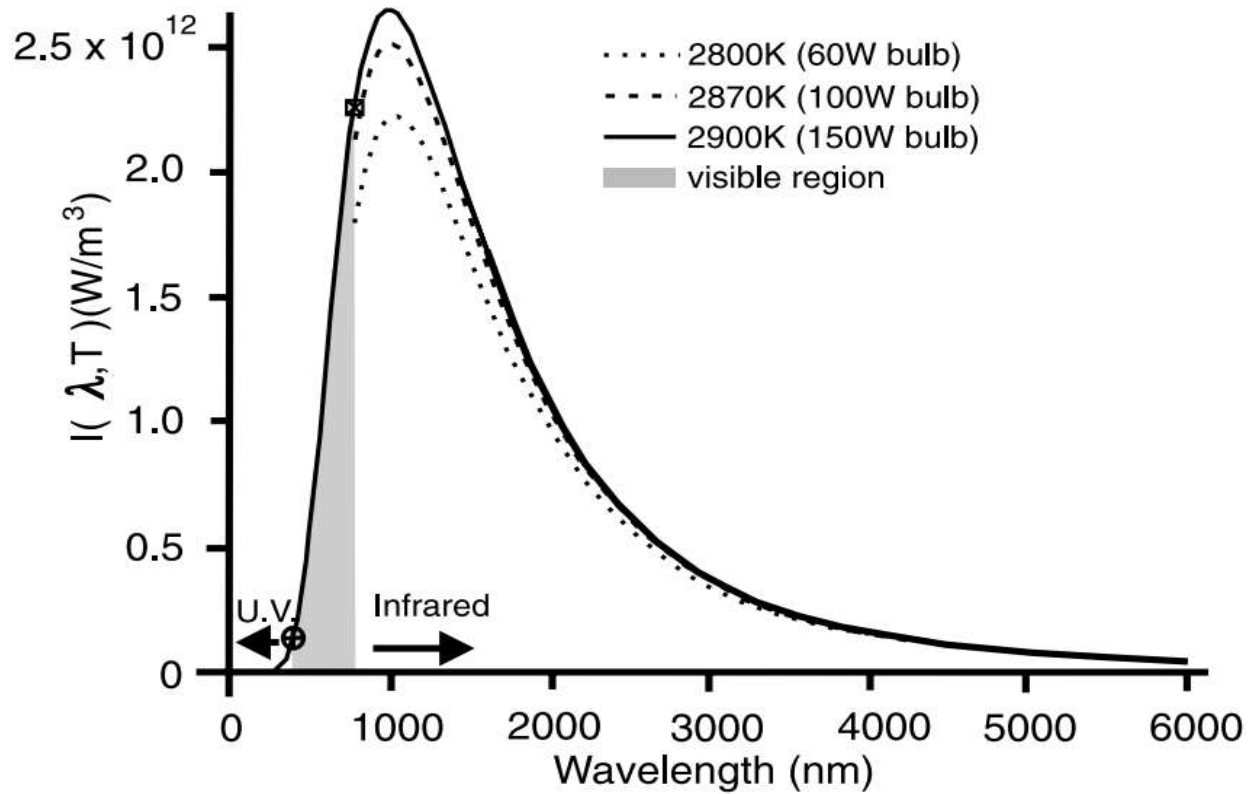


Figure 8: Blackbody emission spectral for three lamps at different color temperatures with their emission curves showing the entire spectrum (U.V, Visible and Infrared wavelength) that was reproduced from (MacIsaac et al., 1999).

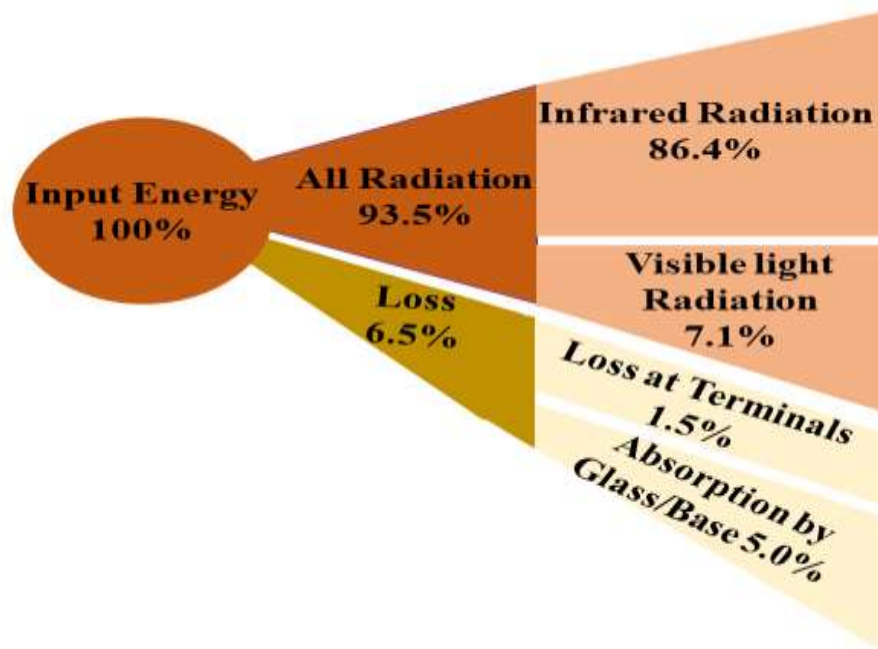


Figure 9: Schematic diagram of the typical ratios of radiated energy and heat losses redrawn from (USHIO America, 2018)

Table 4: Summarize emissivity factors for incandescent lamps at different operating temperatures

SN	Emissivity factor	Operating temperature (K)	Reference
1	0.502	1500	(Fu, Leutz, & Ries, 2006)
2	0.440	3200	(Fu et al., 2006)
3	0.386	2900	(MacIsaac et al., 1999)
4	0.65	2900	(Lide, 2003)

The productivity of culturing systems is determined by the microbial cell growth rate which, for fixed abiotic factors and fluid dynamics, is a function of the light regime and profile to which the cells are suggested within the photobioreactor (Acién Fernández et al., 1999; Kong & Vigil, 2014; Kunjapur & Eldridge, 2010). In uniformly illuminated PBRs with homogenously and randomly oriented microbial cells, the illumination intensity decreases sharply due to absorption and scattering by microbial cells or bubbles if present (Acién Fernández et al., 1999; Luo & Al-Dahhan, 2004). Quantifying this photo-biotechnological process is very essential in monitoring and evaluating the light intensity and availability, which is of utmost important when operating this PBR at even high microbial cell concentration and large light-path lengths (Molina-Grima et al., 1999). The microbial cell light environment is characterized by several parameters including

(i) light-path length, (ii) microbial cell concentration (iii) reactor wall properties (iv) microbial cell morphology - cell diameter and shape (v) cell pigment fraction (vi) bubbles if present (Acién Fernández et al., 1999; Berberoglu, Yin, & Pilon, 2007; Luo & Al-Dahhan, 2004; Pilon et al., 2011).

The illuminated PBR provides light for microbial absorption in the form of photons. Each photon absorbed by the microbial photosynthetic pigment contains discrete portions of energy,  $E$  as describe by (equation(3)) (Carvalho et al., 2011). The photosynthetic pigments of purple non sulfur bacteria are carotenoids and bacteriochlorophylls with wavelength absorption at visible ( $400 \text{ nm} \leq \lambda \leq 500 \text{ nm}$ ) and infrared ( $700 \text{ nm} \leq \lambda \leq 1000 \text{ nm}$ ) respectively (Nogi et al., 1985; Pilon et al., 2011). As per (equation (3)), the specific energy content is inversely proportional to wavelength. Therefore, the carotenoid pigment experiences mostly ionizing effect and changes in its molecules due to the short wave-high energy content. Conversely, the long wavelength absorption of bacteriochlorophylls has a low energy content to mediate chemical changes in its molecules therefore resulting to thermal effect only (Carvalho et al., 2011). The heat generation from microbial light absorption is referred to as sensible heating within this thesis. However, it becomes volumetric when the fluorescence and metabolic waste heat are included to it giving the non-uniform sensible volumetric heating.

$$E = \frac{hC}{\lambda} \quad (3)$$

Where  $h$  is Planck's constant ( $6.626 \times 10^{34} \text{ J.s}$ ),  $C$  is the speed of light in vacuum ( $3 \times 10^8 \text{ ms}^{-1}$ ) and  $\lambda$ , is the wavelength (nm).

Several numerical methods and models have been applied to acquire reliable data in characterizing the light transfer within culturing systems including solving radiation transport equations (equation (4)) (Berberoglu, Gomez, & Pilon, 2009; Berberoglu et al., 2007; Kong & Vigil, 2014; Murphy & Berberoğlu, 2011; Pilon et al., 2011; Wheaton & Krishnamoorthy, 2012), two-flux approximation (equation (5)) (Cornet, Dussap, Gros, Binois, & Lasseur, 1995; J. Huang et al., 2015; Pilon et al., 2011), and Beer-Lambert law (equation (6)) (Acién Fernández et al., 1999; Luo & Al-Dahhan, 2004; Pilon et al., 2011; Pires et al., 2017; Dongda Zhang et al., 2015; T. Zhang, 2013).



$$\frac{dI_{\lambda}(\vec{r}, \vec{s})}{ds} + (a_{\lambda} + \sigma_{\lambda,s})I_{\lambda}(\vec{r}, \vec{s}) = \frac{a_{\lambda}n^2\sigma T^4}{\pi} + \frac{\sigma_{\lambda,s}}{4\pi} \times \int_0^{4\pi} I_{\lambda}(\vec{r}, \vec{s}_i)\Phi_{\lambda}(\vec{s}_i, \vec{s})d\Omega_i \quad (4)$$

Where  $I_{\lambda}(\vec{r}, \vec{s})$  represents the wavelength ( $\lambda$ ) radiation intensity, in the light path direction  $\vec{s}$ , and position vector  $\vec{r}$ , wavelength dependent absorption coefficient  $a_{\lambda}$ , light path length  $s$ , scattering direction  $\vec{s}_i$ , wavelength dependent scattering coefficient  $\sigma_{\lambda,s}$ , refractive index  $n$ , Stefan-Boltzmann constant  $\sigma$ , local temperature  $T$ , and solid angle  $d\Omega_i$ .

$$\frac{I_z}{I_0} = \frac{1}{Z} \ln \frac{4\alpha_1}{(1 + \alpha_1)^2 e^{\alpha_2} - (1 - \alpha_1)^2 e^{-\alpha_2}} \quad (5)$$

Where  $\alpha_1 = \sqrt{E_a/(E_a + E_s)}$ ,  $\alpha_2 = \alpha_1 X_b L(E_a + E_s)$ , with  $E_a$  and  $E_s$  being the mass absorption and scattering coefficient respectively. If  $\alpha_1 = 1$  and  $E_s = 0$ , (equations (5)) reverts back to the beer lambert law (equation (6)).

$$I(Z) = I_0 e^{-K_0 Z} \quad (6)$$

Where  $I(z)$  and  $I_0$  represents the local and incident light intensity respectively, the overall spectral attenuation coefficient,  $K_0 = K_b X_b + K_w$ ,  $K_b$  and  $K_w$  being the microbial and water mass extinction coefficients while  $X_b$  and  $Z$  are the microbial biomass concentration and light path length respectively.

The radiation transfer equation (equation (4)) can be solved numerically without simplification for an absorbing, emitting and scattering medium using commercially available software like ANSYS fluent (Malalasekera & Versteeg, 2006; Pilon et al., 2011). Some ANSYS Fluent models like Monte carlo (MC), Descret ordinate (DO) are commonly used to model light transfer in photobioreactors (Kong & Vigil, 2014; Murphy & Berberoğlu, 2011; Pilon et al., 2011; Rek, Rudolf, & Zun, 2012; Wheaton & Krishnamoorthy, 2012; Williamson & Wilson, 2009) assuming non-gray radiation and semi-transparent walls but this comes at a great computational expense. Mindful that, the cornet two flux approximation considers the culture medium to be non-uniform, under high biomass cell concentration where both the absorption and scattering

contributes to the light attenuation. However, the microbial cell scattering is often assumed negligible when operating PBRs at a biomass concentration less than  $1 \text{ Kg}/\text{m}^3$  (Berberoglu et al., 2007; Jacobi, Steinweg, Sastre, & Posten, 2012; Krujatz et al., 2015; Wheaton & Krishnamoorthy, 2012) which simplifies (equation (5)) in the beer lambert law (6). As a result, equation (3) was chosen and used in mathematical tackling the volumetric sensible heat-source generated from light penetration (see section 3.4.2).

## 2.4 THERMOSIPHON LOOPS, DESIGN AND APPLICATIONS

Natural or free convection flows (natural circulation) arise due to the effect of a density difference in a body field (e.g., gravity) and the density difference can be brought about by a temperature difference or heterogeneous multiphase flow (Gandhi et al., 2011; Louisos et al., 2013; Zvirin, 1982). In practice, creating natural circulation within rectangular and cylindrical enclosures, square cavities or any loop can be attainable through heating of the working fluid from the bottom and cooling it from above (Gandhi et al., 2011; Louisos et al., 2013; Zvirin, 1982). The continuously process of heating and cooling establishes a temperature difference within the loop and consequently creates a density gradient thereby enabling the lighted fluid to rise up and be replaced by the heavier fluid as it falls down with the fluid motion being governed by buoyancy forces (Başaran & Küçüka, 2003; Budihardjo et al., 2007; Louisos et al., 2013) as illustrated in Figure 10.

Natural circulation has gained significant attention in engineering applications such as solar energy systems, cooling of electrical and electronic equipment, thermal energy storage, and heat removal systems in nuclear power plants, as a result of their high reliability, low maintenance costs and absence of moving parts. Some of these natural circulation loops are displayed in Figure 11.

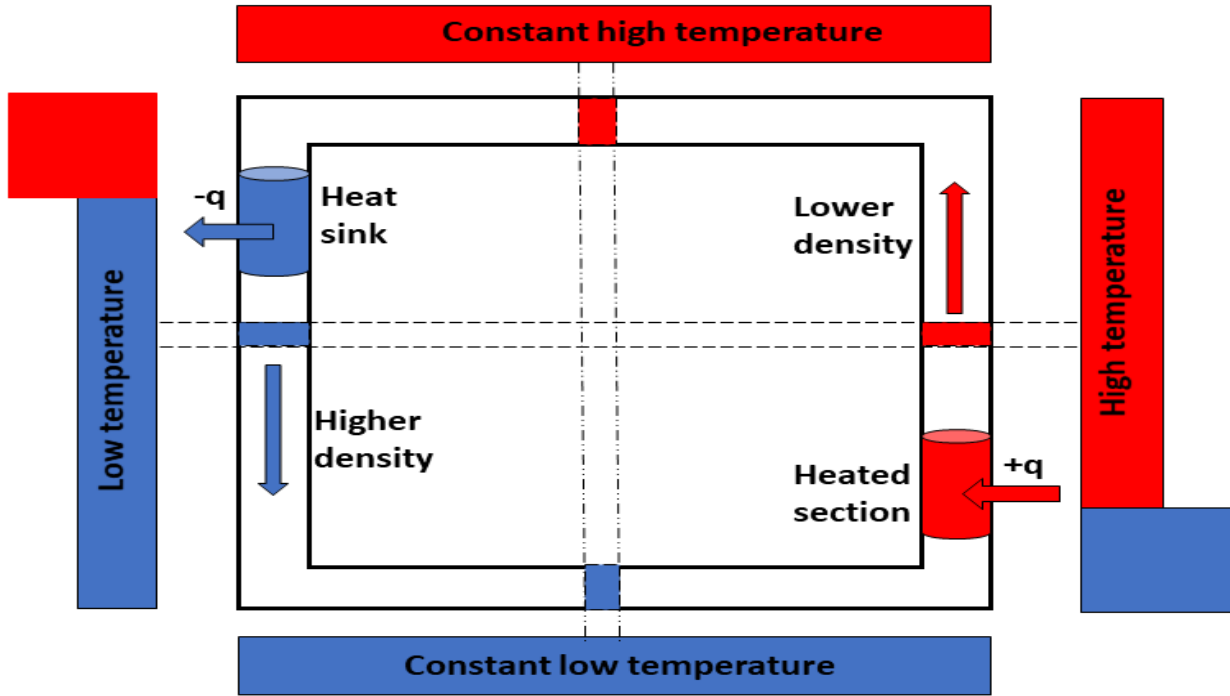


Figure 10: Schematic of density variation in a rectangular thermosiphon loop with a low level heated section and a high level heat sink redrawn from (Budihardjo et al., 2007)

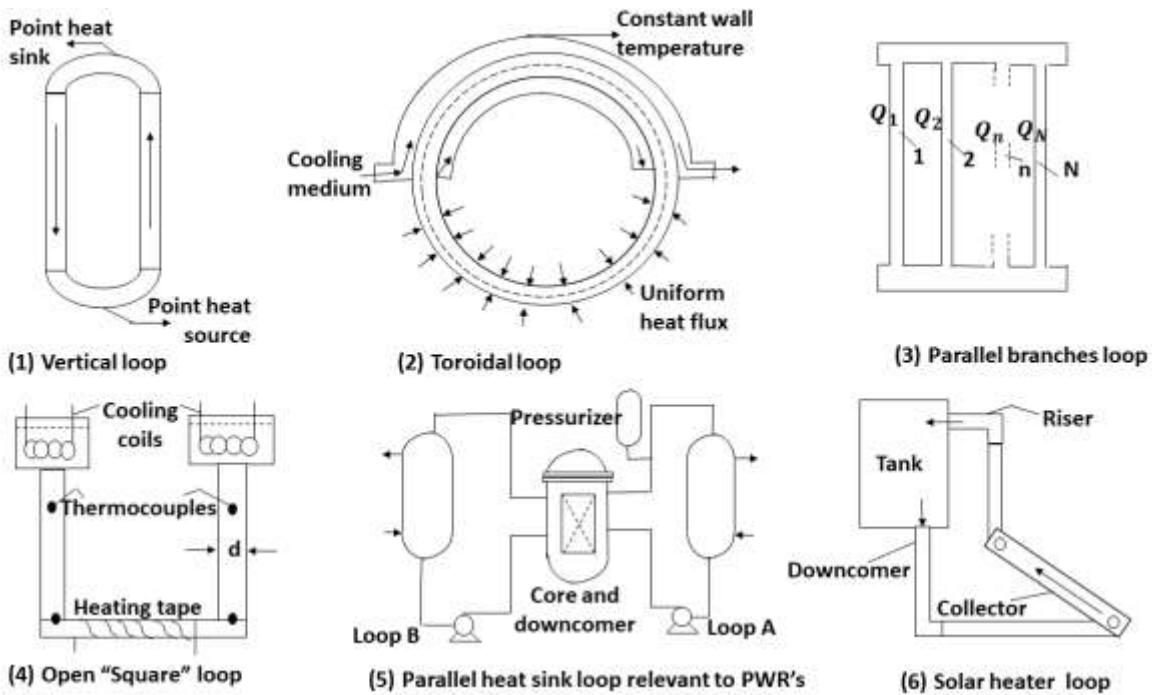


Figure 11: Schematic of the various natural circulation loops redrawn from (Zvirin, 1982).

Since the very 1<sup>st</sup> work on the performance of solar water heaters (SWH) with natural circulation (figure 23 (6)) was published by Close in 1962, SWH in numerous industrial and domestic applications have drastically increased over the last 30 years (Shukla, Sumathy, Erickson, & Gong, 2013). This is mainly driven by the relative abundance of solar radiation which is harnessed as alternative renewable energy. China leads the global SWH market (118  $GW_{th}$ ) while the European Union, Japan, India and Brazil have recorded a significant expansion (Shukla et al., 2013). Closed thermosiphon loops are characterized by three main sections which forms the basic structural units of a thermosiphon solar water heaters namely (i) storage tank, (ii) connecting pipes (downcomer and upriser), and (iii) collector/absorber whereby thermosiphon is exploited to transport the heat gain by the heat transfer fluid (HTF) from the solar collector to the storage tank (Ogueke et al., 2009; Shukla et al., 2013). Among the commonly used HTFs like water, air, glycol/water mixture, hydrocarbon and refrigerant or phase change liquids (Shukla et al., 2013), water stands out as the favorite HTF for SWH systems because of its high specific heat capacity, low viscosity, less expensive and non-toxic features (Shukla et al., 2013). As a result, water was chosen for this thesis since as it's the growth medium for naturally occurring photosynthetic bacteria. Therefore, all the thermophysical properties pertinent to water will be used.

There are complexities involve in designing thermosiphon SWH systems since as their system performance is affected by the interaction of multiple factors, namely: (i) design parameters, (ii) operating conditions, and (iii) metrological data (Shariah & Shalabi, 1997). For this reason experimental studies on the development of thermosiphon systems (Asfia & Dhir, 1996; Başaran & Küçüka, 2003; Morrison & Braun, 1985; Samanci & Berber, 2011; Vijayan, Sharma, & Saha, 2007) are performed on trial and error basis. However, this approach can be expensive and timing consuming. An alternative method of investigation is the use of fundamental theoretical CFD modeling, to predict and characterize thermosiphon and natural convection systems. There have been some investigations using a modeling approach of these systems for water heating, and other engineering applications, however, none have been performed with the aim or characterizing systems designed for photosynthetic organisms (Alizadehdakhel et al., 2010; Budihardjo et al., 2007; Fadhl et al., 2013; Freegah et al., 2013; Gandhi et al., 2011; Louisos et al., 2013; Morrison & Braun, 1985; Morrison et al., 2005; Pilkhwal et al., 2007b; Rek et al., 2012; Williamson & Wilson, 2009).

While the CFD modeling methodology has been well established in literature, most of these investigations make use of a simplified boundary condition such as uniform constant wall temperature and surface flux as the heating source on the absorber/collector sections. This approach works well under certain experimental conditions of electric heating, nuclear fuel element, heat exchangers, or boiling water heating. However, it is not well suited for the modeling of natural or artificial externally illuminated systems like a thermosiphon PBR, for which light penetration, absorption and scattering by the working fluid brings about non-uniform volumetric heating at the collector/absorber sections and must be accounted for by solving a relevant radiation transfer equation (equation (4), (5) or (6)).

## 2.5 COMPUTATIONAL FLUID DYNAMICS MODELING AND EXPERIMENTAL VALIDATION

CFD modeling is a methodology based on the theories of fluid mechanics, mathematics (fundamental governing equations for the conservations of mass (7 and 10), momentum (8 and 11), energy (9 and 12), ) and computer science (software tools e.g. solvers, pre and post processing utilities). This is used as a powerful tool in solving and obtaining approximate solutions (qualitative predictions) for complicated fluid flow, heat and mass transfer, chemical reactions and other related phenomena (ANSYS Fluent, 2016; Malalasekera & Versteeg, 2006; Pires et al., 2017) which cannot be done experimentally or analytically. Moreover, there are many other advantages of CFD over experiment-based approaches to analysis and designing fluid systems including (i) substantial reduction of lead times and costs of new designs, (ii) ability to study systems where controlled experiments are difficult or impossible to perform (e.g. very large systems), (iii) ability to study systems under hazardous conditions at and beyond their normal performance limits (e.g. safety studies and accident scenarios) and (iv) practically unlimited level of detail of results (Malalasekera & Versteeg, 2006).

$$\begin{aligned} & \text{(Rate of increase of mass in fluid element)} \\ & = \text{(Net rate of flow of mass into fluid element )} \end{aligned} \quad (7)$$

$$\begin{aligned} & \text{(Rate of increase of momentum of fluid particle)} \\ & = \text{(Sum of forces on fluid particle )} \end{aligned} \quad (8)$$

$$\begin{aligned}
& \text{(Rate of increase of energy of fluid particle)} \\
& = \text{(Net rate of heat added to the fluid particle)} \\
& + \text{(Net rate of work on the fluid particle)}
\end{aligned} \tag{9}$$

$$\frac{\partial \rho}{\partial t} = \nabla \cdot (\rho \vec{v}) = S_m \tag{10}$$

Where equation (10) is the general form of the mass conservation equation and is valid for both compressible and incompressible flows. The mass source  $S_m$  can be added onto continuous phase from either a dispersed second phase (e.g., due to vaporization of liquid droplets) and/or any user-define sources/functions (UDF).

$$\frac{\partial}{\partial t}(\rho \vec{v}) + \nabla \cdot (\rho \vec{v} \vec{v}) = -\nabla P + \nabla \cdot (\bar{\tau}) + \rho \vec{g} + \vec{F} \tag{11}$$

In the conservation of momentum equation (11) of a non accelerating reference frame,  $P$  represents the static pressure,  $\bar{\tau} = u \left[ (\nabla \vec{v} + \nabla \vec{v}^T) - \frac{2}{3} \nabla \cdot \vec{v} I \right]$ , is the stress tensor,  $u$  is the molecular viscosity and  $I$  is the unit tensor, while  $\rho \vec{g}$  and  $\vec{F}$  are the gravitational body force and external body forces (e.g., that arises from dispersed phase interaction) respectively. The  $\vec{F}$  source term is model-dependent (e.g., porous-media) and user-define sources/functions (UDF).

$$\frac{\partial}{\partial t}(\rho E) + \nabla \cdot (\vec{v}(\rho E + P)) = \nabla \cdot \left\{ K_{eff} \nabla T - \sum_j h_j \vec{J}_j + (\bar{\tau}_{eff} \cdot \vec{v}) \right\} + s_h \tag{12}$$

Equation (12) is the general form of the energy conservation equation solved by ANSYS Fluent where the first three terms on the right-hand side represent the energy transfer due to conduction, species, and viscous dissipation respectively.  $K_{eff} = (K + K_t)$  is the effective conductivity and  $K_t$  is the turbulent thermal conductivity which is defined as per the employed turbulent model.  $\vec{J}_j$ , is the species diffusion flux while the energy source term  $S_h$  includes the heat of chemical reactions and other volumetric heat sources.

$$E = h - \frac{P}{\rho} + \frac{v^2}{2} \tag{13}$$

Equation (13) is part of equation (12) where  $h = (\sum_j Y_i h_j)$  is the sensible enthalpy of ideal gas with a species mass fraction  $Y_j$  and enthalpy,  $h_j = \int_{T_{ref}}^T C_{p,j} dT$

In their partial differential form (equation (10) to (12)), are the fundamental governing equations which describes the existing relationships between the temperature, velocity, pressure, and density of the fluid flow problem including those that are reacting or non-reacting, laminar or turbulent, compressible or incompressible (ANSYS Fluent, 2016; Malalasekera & Versteeg, 2006; Pires et al., 2017). CFD replaces these partial differential equations with sets of algebraic equations which can then be solved numerically at specific locations by iteration and with the help of digital (High speed and large memory) computers in a process called discretization (Malalasekera & Versteeg, 2006; Pires et al., 2017).

These numerical solutions are possible through three distinctive techniques namely (i) Finite difference method (FDM), (ii) finite element method (FEM) and, (iii) spectra method (Malalasekera & Versteeg, 2006). The finite volume method (FVM) which is a special formulation of the FEM and central to some of the most well-established CFD codes such as CFX/ANSYS, FLUENT, PHOENICS and STAR-CD (Malalasekera & Versteeg, 2006), was chosen for this study because of its advantages over the other CFD techniques, namely: (i) exact conservation of relevant properties for each control volume (finite cell size) by minimizing residuals, (ii) clear relationship between the numerical algorithm and the underlying conservation principles, (iii) better computer memory and speed, and (iv) working concepts are easily understood by engineers (Malalasekera & Versteeg, 2006).

The iterative method of resolving the algebraic equations over each control volume element results in residuals which are minimized by changing the value associated with each desired variable in successive iterations. However, this often leads to residual errors resulting from the interpolation process between volumes (Malalasekera & Versteeg, 2006). These residual errors indicate that the approximated solution may have be dependent on the model resolution or may be have been compromised by computer round-off errors (Malalasekera & Versteeg, 2006). Therefore, the exact existence of the approximated solution is difficult to establish theoretically only and more to that, the uniqueness of the solution cannot be guaranteed but the possible solution convergence is dependent on the initial condition (Malalasekera & Versteeg, 2006). Nevertheless, the solution accuracy can be verified with a grid dependence test (where the solution does not change significantly with mesh size) but there are no explicit rules governing

the model accuracy with respect to the actual observed physical conditions of the setup without experimentation (Malalasekera & Versteeg, 2006).

The numerical algorithms with which CFD solves complex fluid flow problems are structured around sophisticated user interfaces where parameters are inputted and results are examined in three main elements namely (i) a pre-processor, (ii) a solver, and (iii) a post-processor, so as to provide easy access to their solving power (Malalasekera & Versteeg, 2006; Pires et al., 2017). At the pre-processor, the input flow problem is subsequently transformed into a suitable form for the solver's use and its main user activities include (i) geometry definition or computational domain, (ii) grid generation (division of the computational domain into a grid or mesh, (iii) physical and chemical phenomena selection, (iv) definition of fluid properties, and (v) specification of appropriate boundary conditions (Malalasekera & Versteeg, 2006). At the solver, the numerical algorithm performs (i) integration of the governing equations over all the control volumes of the computational domain, (ii) discretization, (iii) solves the set of algebraic equations iteratively (Malalasekera & Versteeg, 2006). The post-processor is equipped with versatile data visualization tools including (i) domain geometry and grid display, (ii) vector plots (iii) line and shaded contour plots, (iv) 2D and 3D surface plots, (v) particle tracking, (vi) view manipulation (translation, rotation, scaling etc.), and (vii) colour postscript output (Malalasekera & Versteeg, 2006).

The advent of low cost, high speed computers coupled to the rapid progress in parallel computing and development of several commercial CFD codes (PHOENICS, EFDC, FLUENT, CFX/ANSYS, Modified K-FIX, CVD-2, STAR-CD, COMSOL, Fluent STABILized, FAOM, etc.) (Bitog et al., 2011; Pires et al., 2017) has enabled scientists, and engineers to analyse complex and integrated systems through CFD simulations. This has proven to be very reliable when the CFD simulations results are validated with experiments leading to their numerous application in (i) conceptual studies of new designs, (ii) detail product development, and (iii) troubleshooting and redesigning with significant time, cost and workload reduction of designing so many prototypes and testing them experimentally for optimization purposes (Bitog et al., 2011; Gómez-Pérez et al., 2015; Pires et al., 2017). In recent years, researchers have applied mostly FLUENT and CFX/ANSYS commercial CFD codes to accurately and conveniently analyze, and visualize flow characteristics inside Photobioreactors. For instance, raceway ponds



(Xu, Li, & Waller, 2014; Yang et al., 2016), flat PBRs (Massart, Mirisola, Lupant, Thomas, & Hantson, 2014), tubular PBRs (Gómez-Pérez et al., 2015), vertical column PBRs, such as draft tube airlift PBRs (J. Huang et al., 2016; Luo & Al-Dahhan, 2011; Soman & Shastri, 2015; Wheaton & Krishnamoorthy, 2012; Yu et al., 2009). As well, this FLUENT and CFX/ANSYS commercial CFD codes have extensively been applied in modeling natural convection and thermosiphon systems (Budihardjo et al., 2007; Fadhl et al., 2013; Gandhi et al., 2011; Louisos et al., 2013; Morrison et al., 2005; Rek et al., 2012).

The experimentation for validating CFD simulations includes the identification and characterization of flow structures by making use of some experimental tools which have studied and classified under Experimental Fluid Dynamics (EFD) as intrusive and nonintrusive techniques, or as planer measurement techniques, point measurement techniques, and volumetric measurement techniques (Joshi et al., 2009). Techniques such as (i) dye injection, (ii) smoke injection, (iii) hydrogen bubbles and photochromic tracers, and (iv) fluorescent particle tracking which are widely used for flow visualization and less for quantitative characterization have been group under marker image tracking methods by (Joshi et al., 2009) making it possible for their working principle as well as their advantages and limitations to be compared with other techniques as seen in Table 6.

On the other hand, point and planer measurement techniques are to date the most implemented techniques while holographic particle image velocimetry (HPIV) and stereoscopic particle image velocimetry (SPIV) are getting more recent attention (Cui & Fan, 2004; Joshi et al., 2009). Also, the performance of these techniques in terms of qualitative and quantitative characterization of flow structures is represented in Table 5.

Table 5: Relative performance of the different experimental tool, reproduced from (Joshi et al., 2009).

SN	Performance parameter	Marker image tracking method	Hot film anemometry HFA	Laser Doppler velocimetry LDV	Particle image velocimetry PIV	Volumetric measurement techniques
1	Mean velocity	cannot be estimated	can be estimated but without directional information	Accurately measured	Accurately measured	Accurately measured
2	Turbulent kinetic energy	cannot be estimated	gives good estimate	gives good estimate	Gives good estimation	Gives good estimation
3	Energy dissipation	cannot be estimated	obtain using energy spectrum	can be estimated using EIM method and dimensional analysis equispacing is required	Can be estimated using structure function approach	Can be estimated using structure function approach
4	Energy spectrum	cannot be estimated	3D spectrum gives correct values	can be estimated using EIM method and dimensional analysis equispacing is required	Can be estimated using structure function approach	Can be estimated using structure function approach
5	Structure time scale	cannot be estimated	gives good estimate	gives good estimates	can be estimated but reliability reduces with increase Re	can be estimated but reliability reduces with increase Re
6	Shape and size of structure	gives good estimate	cannot be directly estimated	cannot be directly estimated	gives good estimate	can be accurately estimated

Table 6: Experimental tools for structure characterization, reproduced from (Joshi et al., 2009).

SN	TECHNIQUES	PRINCIPLE	ADVANTAGES	LIMITATIONS
1	Marker image tracking method (i) dye injection, (ii) smoke injection, (iii) hydrogen bubbles and photochromic tracers, and (iv) fluorescent particle tracking	The underlying principle governing these techniques is the measurement of the simulations displacement marked by fluid particles in consecutive images	Very good for flow visualization, and in correlating probe-type turbulent burst detection techniques with the corresponding visualization data	Extracting of accurate quantitative is very difficult
2	Point measurement techniques (i) laser Doppler velocimetry (LDV)  (ii) Hot film anemometry (HFA)	Provides instantaneous velocity components at the point within the flow field where two or more mutually perpendicular laser beams interact to form a fringe pattern. The seeding particle scatters the incident laser as it passes through the fringe and induces a shift in frequency called Doppler shift which is depended on the fringe spacing and the velocity of the particle normal to the fringe.  Works on the convective heat transfer from a heated wire film element placed within a fluid flow where any changes in fluid conditions can that affects the heated element will be virtually detected instantaneously by a constant temperature/constant current HFA system.	Nonintrusive, factory calibrated and micrometer –sized seeding are traceable  High data rate of $\sim 20KHz$ , equispaced data and evaluation of entire energy spectrum	Unequispaced techniques, interpolation is needed for equispacing and high frequency values of energy are anomalous  Intrusive techniques, requires prior knowledge for calibration, HFA probes are very sensitive and costly, point dataset, can't provide information on flow structure's spatial topology, voltage-velocity calibration are crucial, limited response at high frequencies, voltage stability and temperature variation are crucial, and, negative velocities cannot be measured reason why mean velocity cannot be reported
3	Planer measurement technique (i) Particle image velocimetry (PIV)	The fluid volume under investigation is seeded with a few micrometer-sized particles which are assumed to closely follow the fluid flow while a slice of the flow field is illuminated with a pulsing lighting sheet. This followed by sing a	Planer measurement technique, two or three components measurement is possible, possibilities of evaluating spatial derivatives, possibilities of	Low data rate ( $\sim 7 - 10Hz$ ), spatial limitation by window size, reduced accuracy for strong velocity gradient measurements.

		digital CCD camera to record the two images of the fluid flow within a short time interval and processing these two successive images to get the instantaneous velocity field. By dividing the entire image into interrogation areas, an intercorrelation technique is used to evaluate the probably displacement of each seeding particle.	velocity measurement over a wide range, provides more space information on flow instabilities with coherent and coherent turbulent structures.	
	(ii) Laser-induced fluorescence, (LIF)	Fluorescent dye is used to seed flow and based on the temperature and/or concentration, the intensity of the local light changes and the local transient variation is obtained. It is an extension or add-on to PIV technique	Quantification of scalar flux and cross-correlation.	Same as those in PIV techniques
4	Volumetric measurement techniques			
	(i) Stereoscopic particle image velocimetry (SPIV)	SPIV is commonly referred to as the 3D extension of the PIV technique and provides the three velocity components of the flow confined within a thin slice of the moving fluid medium. It uses the statistical average (correlation) of seeding particles viewed from two separate angles and combined their average 2D vectors into 3D vectors but loses information on the individual seeding particle	Estimation of the shape for flow structures.	Very low data rate, qualitative information and it applicability is limited to simple flow
	(ii) Defocusing particle image velocimetry (DPIV)	Three dimensionality (3D) are achievable through the defocusing principle.	Same as those of the SPIV techniques	Qualitative information
	(iii) Holographic particle image velocimetry (HPIV)	3D information of large particles in a fluid volume are recorded in a hologram instantaneously followed by the reconstruction of the particle image in a 3D space which provides 3D positions including the size and shape information of the particles.	Same as those of the HPIV technique	Qualitative information, low laser light intensity, low sampling and low particle density.

## CHAPTER THREE

### MATERIALS AND METHODS

#### 3.1 RESEARCH DESIGN

The research design adopted for this thesis started with the identification of the various design considerations necessary for the proper operation of a photobioreactor which incorporates the thermosiphon effect to achieve natural circulation from light exposure used for the purpose of culturing photosynthetic bacteria. This was followed by developing a suitable reactor geometry with geometric specification of its components that enabled the construction of a 1L working volume prototype and mounted together with other auxiliary components in an experimental setup for Experimental Fluid Dynamics studies (EFDs). The flow (hydrodynamics) and thermal correlations as a result of light adsorption and light attenuation was evaluated at this stage, producing relevant data to be inputted into the Computation Fluid Dynamic (CFD) modeling. Once the CFD simulations were completed, additional validation experiments were conducted, followed by bacterial growth, light absorption and thermosiphoning studies within the TPBR. Data analyses were performed and reported with possible recommendations for further studies. A flow diagram of the process is as illustrated in Figure 12.

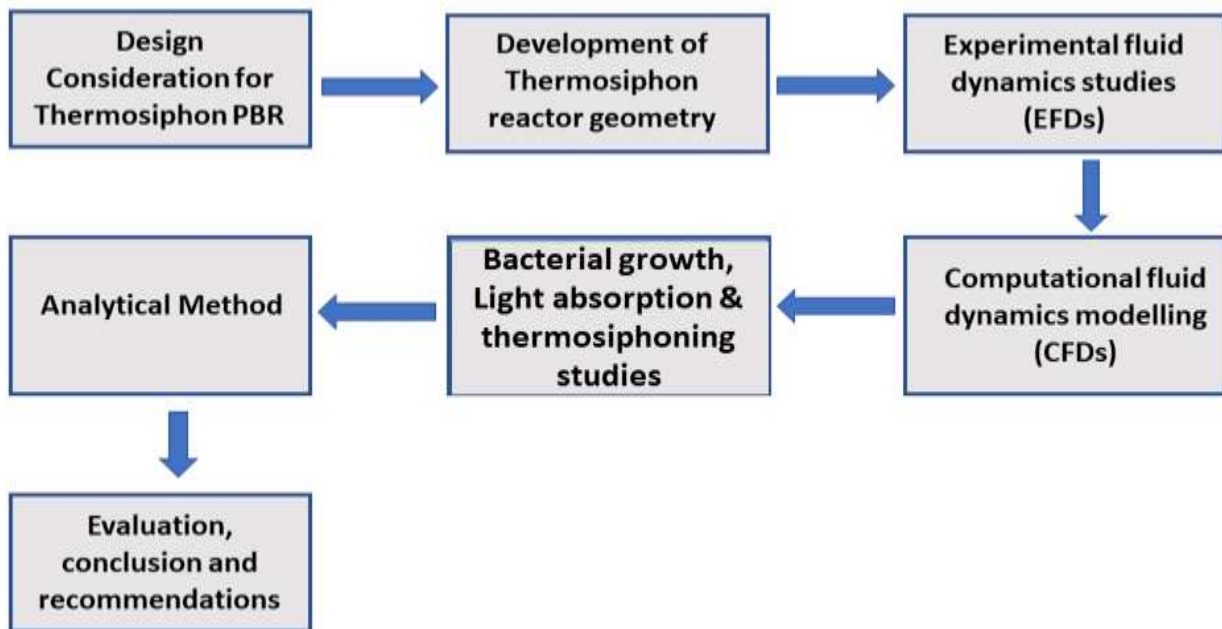


Figure 12: Schematic of the flow diagram adopted for the adopted methodology for this study

### 3.2 THERMOSIPHON PBR'S DESIGN CONSIDERATION

Since both photobioreactors (PBRs) and thermosiphon solar water heaters (SWH) have certain advantages and limitations, and mindful of the unavailability of literature on such a thermosiphon photobioreactor design, the approach utilized in this thesis was to separately examine the existing designs considerations for operational PBRs and SWH systems with the main aim of combining the unique features of these two designs into an integrated design consideration for the novel thermosiphon PBR. The following criteria were outlined to build a high-performance thermosiphon PBR for the purpose of cultivating photosynthetic bacteria:

1. The laboratory scale thermosiphon PBR should have possibility of being autoclaved, which limits the working volume of the prototype to about 1L (Skjånes et al., 2016; Tamburic et al., 2011b).
2. The thermosiphon PBR should have appropriate ports allowing for regular culture sample extraction for the measurement of important parameters during experiments (Skjånes et al., 2016).
3. The thermosiphon PBR should minimize biofilm formation by having smooth internal surfaces and limited bends to increase cleanability (Wang et al., 2012).
4. The thermosiphon PBR should have an optimal surface to volume ratio and light path as features which have been well explored in vertical tubular photobioreactors (Akkerman et al., 2002; Kunjapur & Eldridge, 2010; Skjånes et al., 2016; Tamburic et al., 2011b; Wheaton & Krishnamoorthy, 2012).
5. The thermosiphon PBR should have the possibility of insertion of multiple sensors and electrodes for logging and control of multiple culture parameters (Skjånes et al., 2016; Tamburic et al., 2011b).
6. The system should be as hydrogen impermeable as possible, by ensuring the use of minimal hydrogen gas penetration materials when in contact with the culturing system and connection joints (Akkerman et al., 2002; Skjånes et al., 2016; Tamburic et al., 2011b).
7. All materials used for construction and mounting of the experimental setup were assessed for criteria such as availability on the market, transparency whenever needed, weight,

resistance to oxidation and corrosion, durability and heat resistance (Skjånes et al., 2016; Tamburic et al., 2011b; Wang et al., 2012).

8. The materials should be robust enough to tolerate the intensive use by avoiding tension in breakable materials such as glass caused by contact between these materials and harder materials such as metals (Skjånes et al., 2016; Wang et al., 2012).
9. The thermosiphon PBR should have a simple, low cost solution for temperature control, in the laboratory prototype a cooling water circuit (Skjånes et al., 2016; Wang et al., 2012).

### 3.3 THERMOSIPHON PBR'S GEOMETRY

The thermosiphon PBR geometry was developed from a structural adaptation of the original thermosiphon loop used by Close (1962), to meet the system's performance of a photobioreactor. This process was captured in the geometrical advancement as shown in Figure 13.

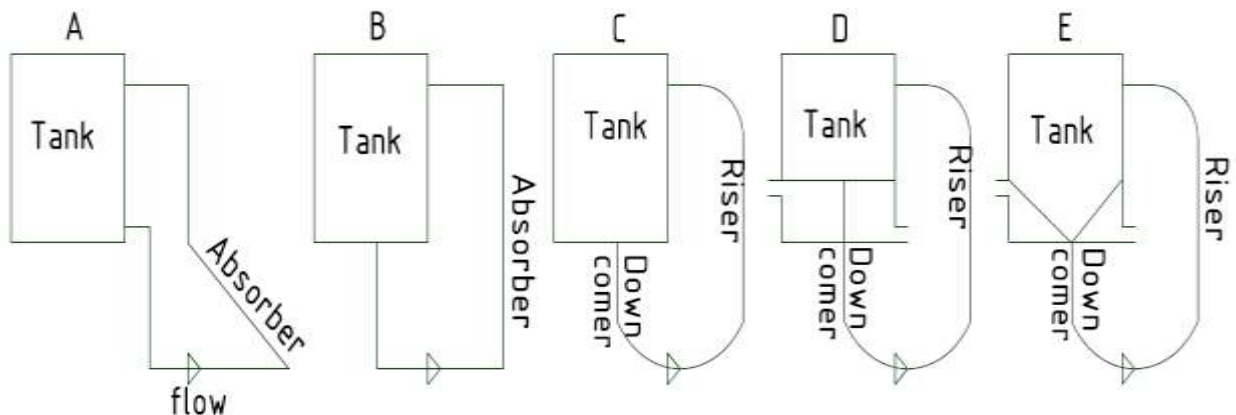


Figure 13: Schematic of geometrical development for novel Thermosiphon PBR

The original thermosiphon loop ((A) of Figure 13 (Close, 1962)) is characterized by three main sections forming the basic structural units of a thermosiphon solar water heaters namely: (i) the storage tank, (ii) connecting pipes (downcomer and upriser), and (iii) collector/absorber (Close, 1962). The downcomer and riser were of tubular shape since previous studies (Fernandes, Dragone, Teixeira, & Vicente, 2010; Ramírez-Duque & Ramos-Lucumi, 2011) have proven them to better allow light penetration at similar biomass concentrations in comparison to their planar counterparts. Loop (B) is a modification of the (A) with the downcomer and upriser

connected at the bottom end and side of the storage respectively. However, the flat horizontal connecting pipe at the bottom of this configuration poses a possible disadvantage of microbial cell settling and sedimentation (Kunjapur & Eldridge, 2010). Therefore, it was adjusted with a 180° bend curvature (elbow) for increased flow speed (Ramírez-Duque & Ramos-Lucumi, 2011) resulting to loop (C). Applying the vertical cooling and vertical heating (VCVH) sections of (Pilkhwai et al., 2007a; Vijayan et al., 2007) to loop (C) resulted to loop (D). As in (B), the flat horizontal bottom of the storage tank in loop (D) connecting the downcomer may bring about microbial cell sedimentation. This was reduced through the implementation of a smooth diameter transition from the storage tank to the downcomer diameters resulting to a truncated cone-shaped bottom storage as seen in loop (E). The describing geometries of (E) are shown in Figure 13. During experimentation, the walls of all the sections except the riser were insulated with 1 cm cotton wool wrapped with aluminum foil to minimize heat flux.

### 3.3.1 ANALYTICAL MODEL FOR SIZING PROTOTYPE THERMOSIPHON PBR

Considering the complexity of the critical system geometries which affect the system's performance (flow rate and thermal stratification) (Shariah & Shalabi, 1997), the identification of the critical geometries within each of these five sections for which the fundamental thermodynamics, fluid dynamics and heat transfer analysis are to be applied is necessary in determining the overall shape and size of the thermosiphon PBR when performing analytical or parametric analysis. These critical geometries are illustrated in Figure 14 with their respective variables while Table 7 compiles the names of these design variables alongside their descriptions.



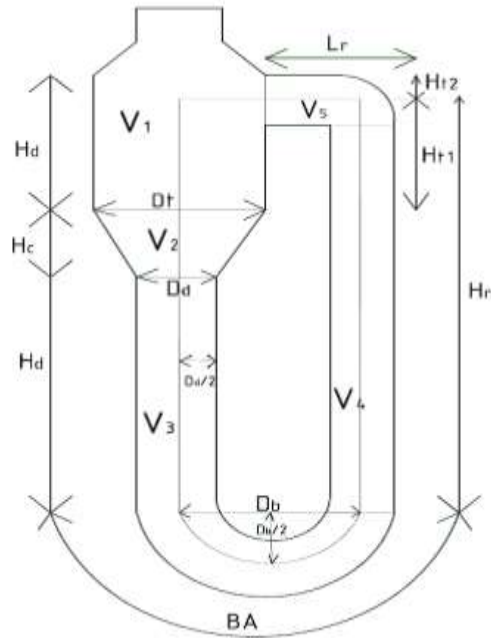


Figure 14: Schematic diagram of thermosiphon PBR's considered design parameters

Table 7: TPBR Critical system design parameters

SN	Parameter	Description
1	$H_t$	Height of vertical cylindrical tank
2	$H_{t1}$	Height of return pipe to vertical cylindrical tank
3	$H_c$	Height of bottom cooling tank
4	$H_d$	Height of downcomer
5	$H_r$	Height of riser
6	$BA$	Bend allowance
7	$L_r$	Length of upriser
8	$D_t$	Diameter of cylindrical tank
9	$D_d$	Diameter of downcomer
10	$L_p$	Length of connecting pipe
11	$V_T$	Total working volume

Since some of these geometrical parameters are constrained by practical limits such as availability and flexibility of the materials, a 1L bench scale prototype TPBR was arrived at by fixing all other design parameters into one equation (equation (14)) using their existing geometrical relationships as reported in literature. Additionally, the riser diameter,  $D_d$  was identified as the single parameter for optimization ( $20\text{mm} \leq D_d \leq 30\text{mm}$ ) thereby satisfying the 1L working volume and autoclave dimension constraints. The light intensity and availability on the riser section was the limiting factor for biomass productivity, growth rate, and product

formation (Acién et al., 1998; Acién Fernández et al., 1999; Carvalho et al., 2011; Fernandes et al., 2010; Kunjapur & Eldridge, 2010; Molina, Fernández, Acién, & Chisti, 2001; D Zhang et al., 2015) with optimal light absorption and minimal light gradient being reported by several researchers in that specified range of  $D_d$ . This approach evades the expensive, time consuming, trial and error method which is mostly applied in designing thermosiphon systems.

$$\begin{aligned} \frac{\pi(D_t/2)^2 H_t}{V_1} + \frac{\pi H_c [(D_t/2)^2 + (D_d/2)^2 + D_t D_d]}{3 V_2} + \frac{\pi(D_d/2)^2 [H_d + BA + H_r + L_r]}{V_3 + V_4 + V_5} \\ = \frac{1,000,000 \text{ mm}^3}{V_T} \end{aligned} \quad (14)$$

The implemented geometrical relationships and assumptions are as listed below:

1. The return pipe from the collector to the storage tank referred to as the upriser with height,  $H_{t1}$  is positioned closest to the top of the storage tank as possible (Shariah & Shalabi, 1997) and was fixed at 0.65 for this study (Close, 1962).

$$\begin{aligned} H_t &= 0.65 H_{t2} \\ H_t &= 0.35 H_{t1} \end{aligned} \quad (15)$$

2. To prevent reverse flow from the connecting pipe to the storage tank, the diameter ratio of the storage tank  $D_t$  to the connecting pipe  $D_d$  equals 4.38 as used by (C. Huang, Lin, & Wang, 2017).

$$D_t = 4.38 D_d \quad (16)$$

3. To minimize friction losses in the connecting pipe and enhance the systems flow rate, the connecting pipe length ( $L_p$ ) (which is the sum of  $H_d, BA, H_r$  and  $L_r$ ) to its diameter is  $\geq 50$  (Freegah et al., 2013) corresponding to equation (4)

$$\begin{aligned} L_p &= H_d + BA + H_r + L_r \\ L_p &= 53.5 D_d \end{aligned} \quad (17)$$

4. The heights ratios of the vertical cylindrical tanks,  $H_t$  and the bottom cooling tank,  $H_c$  is set to 3/2, implying that

$$H_t = 3/2 H_c \quad (18)$$

5. The ratio of the bottom cooling tank height,  $H_c$  to the vertical tanks diameter  $D_t$  equals 3 since as its corresponded to the top collector of the bottom tank as the case for (Shariah & Shalabi, 1997).

$$H_c = 3D_t \quad (19)$$

6. The collector spacing,  $D_0$  is less than or equal to the storage tank diameter  $D_t$  and was approximated equal in this study.

$$D_0 \cong D_t \quad (20)$$

7. The bend allowance height,  $H_{BA}$  equals one-half of  $D_0$  as per the geometrical alignment when applying 180 degree bending.

$$H_{BA} = 1/2 D_0 \quad (21)$$

8. The ration of down comer height,  $H_d$  to the bend allowance height,  $H_{BA}$  was set to 11 so as to enable a smooth 180 curvature of the connecting pipe.

$$H_d = 11H_{BA} \quad (22)$$

9. The absorber/riser height,  $H_r$  equals the summation of the down comer height  $H_d$ , bottom cooling tank height,  $H_c$  and vertical cylindrical tank height,  $H_t$

$$H_r = H_d + H_c + H_t \quad (23)$$

10. Finally, the upriser length,  $L_r$  is gotten by deducting the down comer height  $H_d$ , bend allowance  $BA$ , collecting height  $H_a$ , vertical cylindrical tank height  $H_t$  from the connecting pipe length  $L_p$ .

$$L_r = L_p - (H_d + BA + H_a + H_t) \quad (24)$$

At the end for this process, the optimized geometrical parameters for construction are represented in Table 8. The prototype thermosiphon PBR was constructed out of window glass with the technical drawing of the complete experimental setup and photograph shown in Figure 15 and Figure 17 respectively.

Table 8: Optimized geometrical parameters for TPBR prototype construction

<b>SN</b>	<b>Parameter</b>	<b>Value</b>	<b>Units</b>
1	$H_t$	50.42	<i>mm</i>
2	$H_{t1}$	17.65	<i>mm</i>
3	$H_c$	31.32	<i>mm</i>
4	$H_d$	457.24	<i>mm</i>
5	$H_r$	506.20	<i>mm</i>
6	$BA$	188.89	<i>mm</i>
7	$L_r$	36.31	<i>mm</i>
8	$D_t$	97.86	<i>mm</i>
9	$D_d$	22.34	<i>mm</i>
10	$L_p$	1188.65	<i>mm</i>
11	$V_T$	1 000 000	<i>mm</i> <sup>3</sup>

### 3.4 EXPERIMENTAL FLUID DYNAMIC STUDIES

#### 3.4.1 EXPERIMENTAL SETUP

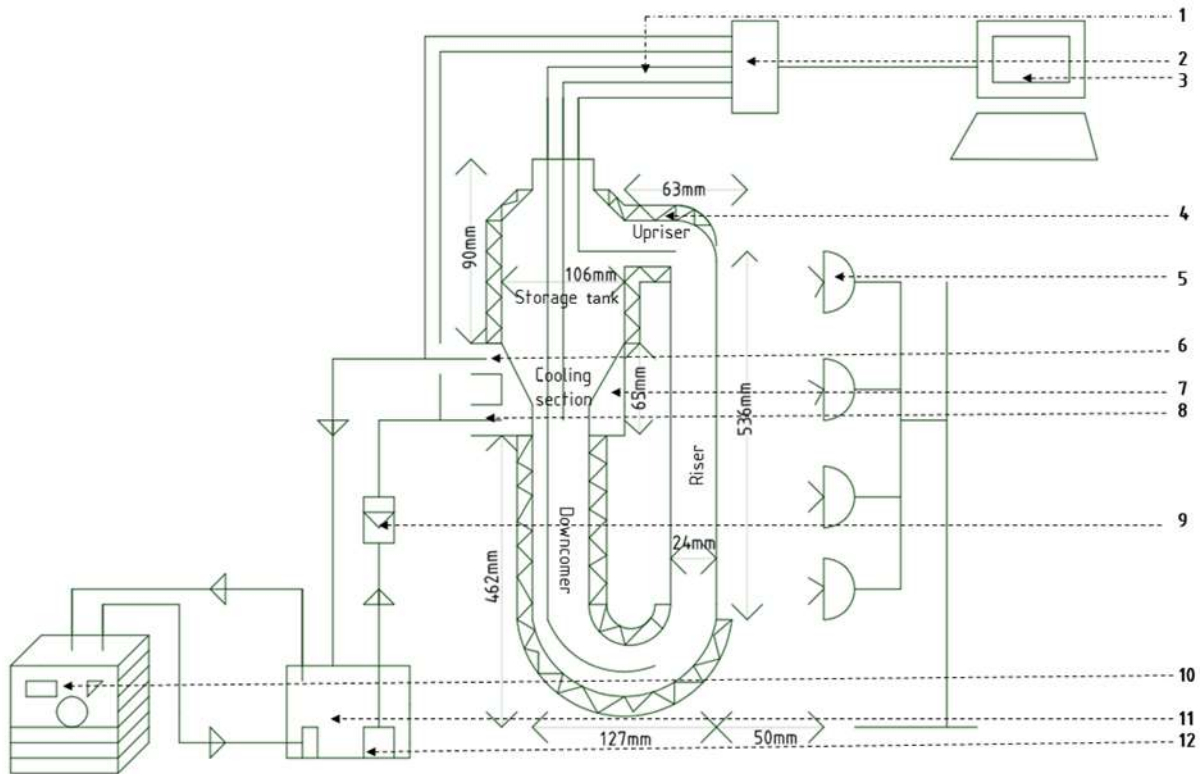


Figure 15: Schematic diagram of the experimental setup: (1) Thermocouples, (2) Data acquisition unit, (3) Computer, (4) Thermal insulation, (5) Halogen lamps, (6) Cooling water outlet, (7) Cooling water inlet, (8) Cooling sections, (9) Rotameter (10) Water chiller, (11) Reservoir, and (12) Submersible water pump

The experimental rig and a schematic view of the experiment setup are shown in Figure 15. The thermosiphon PBR was constructed with glass using the measurements given in Table 8 above and fixed on a framework to ensure vertical orientation. To minimize thermal heat losses to the surrounds, a layer of cotton wool and aluminum foil were used for thermal insulation by wrapping the storage tank, down-comer and up-riser excluding the cooling section to enable visibility of flow. The fluid temperatures were used as an indicator of system performance and the temperature distribution along the thermosiphon PBR were monitored with thermocouples (RTD, PT100, Simplex, Class A) with a 3 wire Nickel Sheath (SS316) of 3 mm diameter were placed and connected to a 4 channels data-acquisition unit (WIKA Instruments REB(TR40), South Africa) with a data sampling rate of 60 seconds which are then transferred to a Dell PC (64-bit, Intel(R) Core (TM) i7-4510U CPU) for further processing. Three of the thermocouples

labeled  $T_1, T_2$  and  $T_3$  were used to monitor the storage tank, down comer and up riser temperatures while two others labeled  $T_{w,in}$  and  $T_{w,out}$  were used to measure the inlet and outlet temperatures of the cooling sections, and the accuracy of the thermocouples was within  $\pm 1^\circ\text{C}$ . During experiments, the cooling water circuit supplies water at predefined conditions (constant temperature and flow rate of  $17^\circ\text{C}$  and  $0.5\text{ L/min}$  respectively) to the inlet through an 8mm ID flexible silicon tubing while the waste heat from the outlet water was removed in a secondary reservoir with a temperature controlled water chiller (HAILEA HS-28A, China) before being recirculated into the system from the secondary reservoir using a submersible water pump (Waterhouse WH360, South Africa). An inline water flow meter (SEAL Water Tech Rotameter 0.1-1.4LPM G1/2'', South Africa) was incorporated into the cooling water circuit which was used to control and measure the inlet volumetric flow rate into the cooling sections. Heating on the riser was provided by the luminance of 4 halogen floodlights fixed on a metal frame enabling the panel to be shifted forward and backward so as to either increase or decreasing the luminance reaching the riser.

### 3.4.2 FLUID FLOW, HEAT AND LIGHT TRANSFER RELATIONSHIPS IN THE TBPR

As shown on the design in Figure 15, the increase and decrease of the working fluid's temperature is brought about by the external one-sided illumination on the riser section and circulation of cooled water through the cooler (tube-in-tube cooling water jacket tube with the water flowing through the annulus) respectively. These are continuously responsible for density differential accounting for thermosiphoning within the TPBR (Gandhi et al., 2011; Louisos et al., 2013). A radiant energy balance around the irradiated area (the riser section) characterizes the light absorption as sensible heat flowing into the system. This is illustrated in Figure 16.

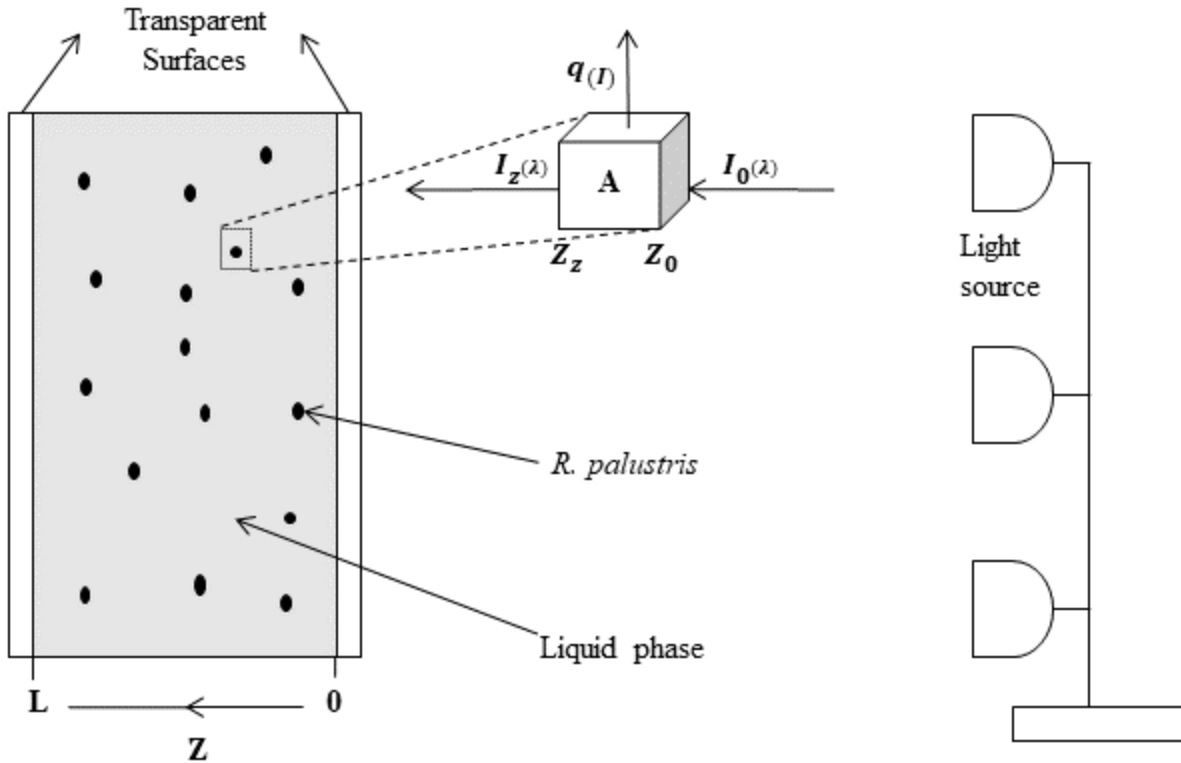


Figure 16: Schematic view of light radiating the TBPR. The front surface ( $z = 0$ ), to the rear surface ( $z = l$ ), with  $A$ ,  $I_0(\lambda)$ ,  $I_z(\lambda)$  and  $q(I)$  being the irradiated area, incident radiant illumination, radiant illumination at any point  $z$ , and volumetric sensible heat generated at that point  $z$  within the riser respectively.

#### 3.4.2.1 MODEL ASSUMPTIONS:

1. The irradiance at any point within the riser ( $I_z(\lambda)$ ) is a function of the total surface irradiation at the riser ( $I_0(\lambda)$ ), the optical properties of the culture (bacterial cell spectral mass extinction coefficient,  $K_b$ , the concentration and morphology of the microbial cells,  $X$ ), and the radial distance from that cell centroid/point ( $z$ ) to the illuminated surface which is mathematically governed by the Beer-Lambert Law (Acién et al., 1998; Acién Fernández et al., 1999; Benson & Rusch, 2006; Luo & Al-Dahhan, 2004; Ogbonna et al., 1995).
2. The light transfer is unidirectional since it is symmetric to the plane of the PBR (Murphy & Berberoğlu, 2011), and set to be perpendicular to the  $y$ -axis therefore the radiant illumination ( $I_0(\lambda)$ ) is to be constant in that direction and the light transmitted to any cell centroid/point ( $z$ ), was determined only in the  $x$ -axis (Berberoglu et al., 2007; Murphy & Berberoğlu, 2011; Sato, Yamada, & Hirabayashi, 2010).

3. The phases (liquid and microbial cells) are well-mixed and randomly oriented, cold, only absorbing and non-scattering in the photosynthetic active region (PAR) of the light spectrum, at very low biomass concentration ( $< 1\text{Kg}/\text{m}^3$ ) (Berberoglu et al., 2007; Murphy & Berberoğlu, 2011).
4. The riser's top and bottom surfaces are non-reflecting (Berberoglu et al., 2007; Jacobi et al., 2012).
5. Steady state radiation transfer prevails (Berberoglu et al., 2007) yielding (equation (25))

$$I_{0(\lambda)}A - I_{z(\lambda)}A - q_{(l)}A(z_z - z_0) = 0 \quad (25)$$

$$I_{0(\lambda)}A - I_{z(\lambda)}A - q_{(l)}A(z_z - z_0) = 0 \quad (26)$$

$$q_{(l)} = \frac{I_{0(\lambda)} - I_{z(\lambda)}}{Z_z - Z_0} \equiv \frac{\Delta I_{(\lambda)}}{\Delta Z} \equiv \frac{dI_{(\lambda)}}{dZ} \quad (27)$$

According to the Beer-Lambert law (equation (6)), where  $K_0$  is the overall spectral attenuation coefficient, and  $K_0 = K_b X$ , where  $K_b$  is the spectral mass extinction coefficient accounting for shelf shading effects between the bacterial cells at a biomass concentrations,  $X$  (Benson & Rusch, 2006; Luo & Al-Dahhan, 2004; Murphy & Berberoğlu, 2011).

Solving for the volumetric heat source term in (equation (27)) by substituting (equation (6)) results to the general (equation (28)) considered as volumetric heat-source due to the light attenuation by bacterial absorption.

$$\therefore q_{(l)}(\text{W}/\text{m}^3) = \frac{dI_{(\lambda)}}{dZ} \equiv -K_0 I_{0(\lambda)} e^{-K_0 Z} \quad (28)$$

However, the halogen lights produce a complete electromagnetic spectrum while the photosynthetic bacteria absorb only in the visible and infrared regions. Therefore, (equation (28)) was modified to generate volumetric heating only in the regions where the bacterial absorption occurs, leading to (equation (29)) which is implemented by a user-defined function (UDF).

$$q_{(l)}(\text{W}/\text{m}^3) = \int_{400}^{900} \frac{dI_{(\lambda)}}{dZ} d\lambda = \int_{400}^{900} -K_{0,\lambda} I_{0(\lambda)} e^{-K_{0,\lambda} Z} d\lambda \quad (29)$$

$K_b$  for *Rhodospseudomonas palustris* was experimentally estimated using the UV/VIS spectrophotometer (Model AE-S60-4U, A&E lab (UK) Co., Ltd) for normal-normal



transmittance measurement of five samples with known biomass concentration over the spectral range of 400 and 900 nm with (equation (30)).

$$K_b = \left[ \frac{\text{slope of } Ab \text{ vs } [Biomass]}{Z_{cuvette}(m)} \right]_{400}^{900} \quad (30)$$

On the other hand, the heat sink removes the sensible heat generated by (equation (29)) because of heat release through convection heat transfer from the walls of the cooling section to the circulating cooled water as per the experimental apparatus Figure 17. This entire process is fully captured by an energy balance of the system (equation (31)) operating under continuous heating and cooling but reaches steady state when ( $\dot{Q}_{lights} = \dot{Q}_{lost}$ ), enabling the radiant energy from the illuminating lights to be turn-off for ambient water cooling which is governed by the Newton's law of cooling (equation (32)). The heat transfer coefficient of the cooling walls was theoretically determined with the Newton's law of cooling by curve fitting (equation (33)) with experimental data as illustrated in Figure 18.

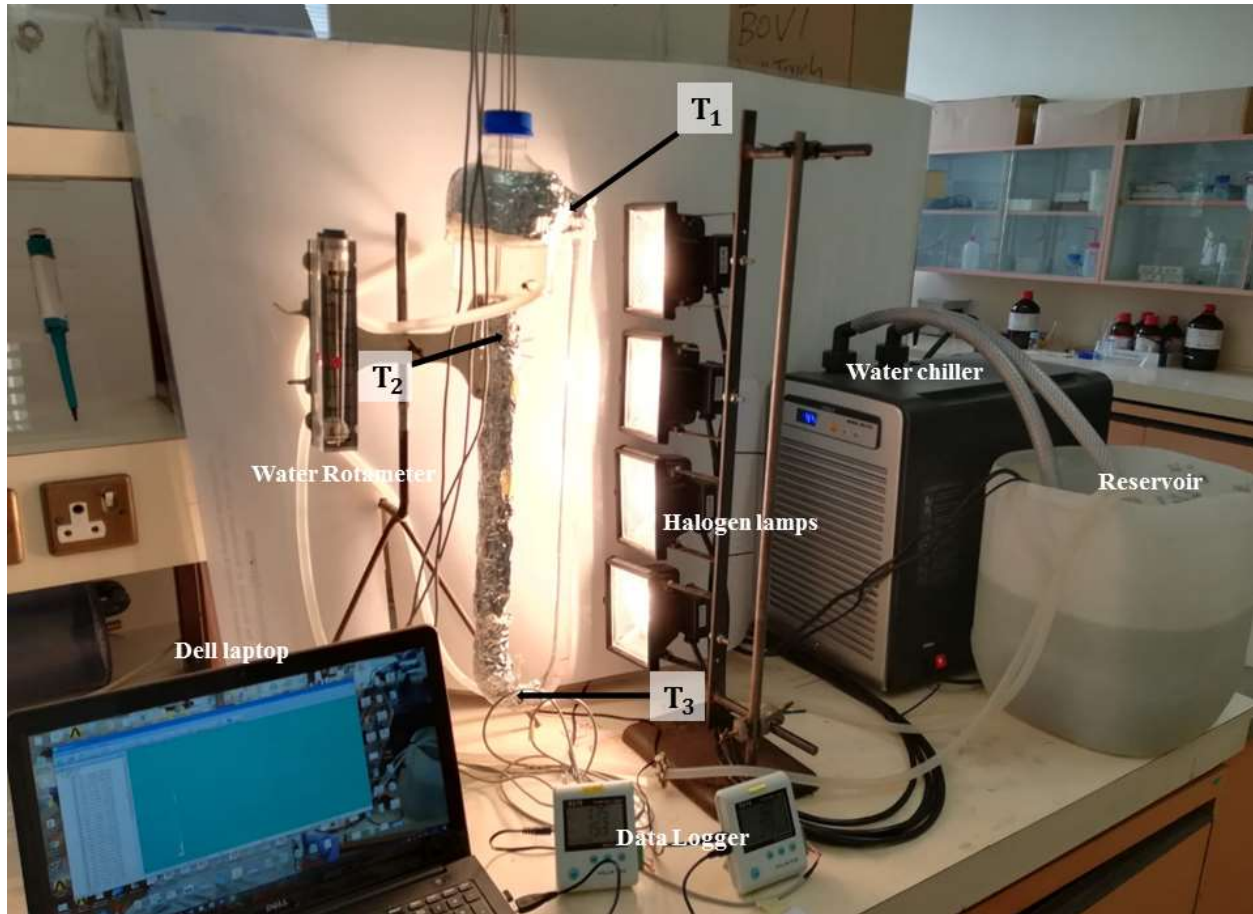


Figure 17: Photograph of the thermosiphon PBR in full operation for heat transfer analysis with the indicated positions of measuring position.

$$mC_p \frac{dT}{dt} = \dot{Q}_{lights} - \dot{Q}_{lost} \quad (31)$$

$$mC_p \frac{dT}{dt} = -\dot{Q}_{lost} \quad (32)$$

$$T(t) = (T_{stab} - T_{w,out})e^{\left(\frac{th_c A_c}{\rho V C_p}\right)} + T_{w,out} \quad (33)$$

Where  $m$ ,  $\rho$ ,  $V$  and  $C_p$  are the mass (kg), density ( $Kg/m^3$ ), volume ( $m^3$ ), and specific heat capacity ( $J/Kg.K$ ) of water respectively,  $\dot{Q}_{lights}$  and  $\dot{Q}_{lost}$  are the rate of heating (J/s) by halogen lamps and rate of losing heat (J/s) by convection respectively,  $t$  is time (s),  $h_c$  is the heat transfer coefficient of cooling section ( $J/s.K$ ),  $T_{stab}$  and  $T_{w,out}$  are the stabilization and outlet sub cooling water temperatures (K) respectively.

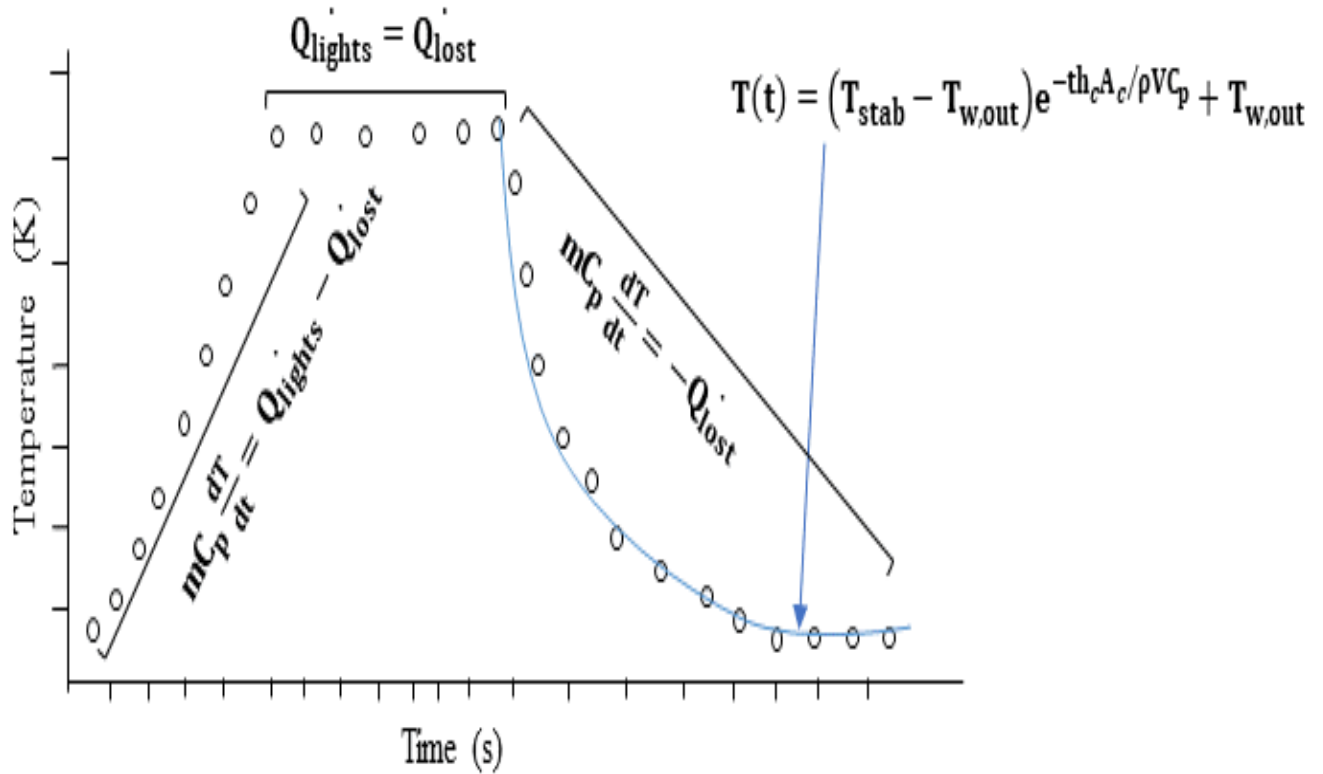


Figure 18: Schematic of the thermosiphon PBR's heating and cooling curve illustrating all the various sections where the heat transfer equations are applied

The riser wall's heat transfer coefficient was estimated with the newton's law cooling by curve fitting (equation (34)) to experimental data obtain from hot water cooling down to ambient in the thermosiphon PBR as illustrated in Figure 19.

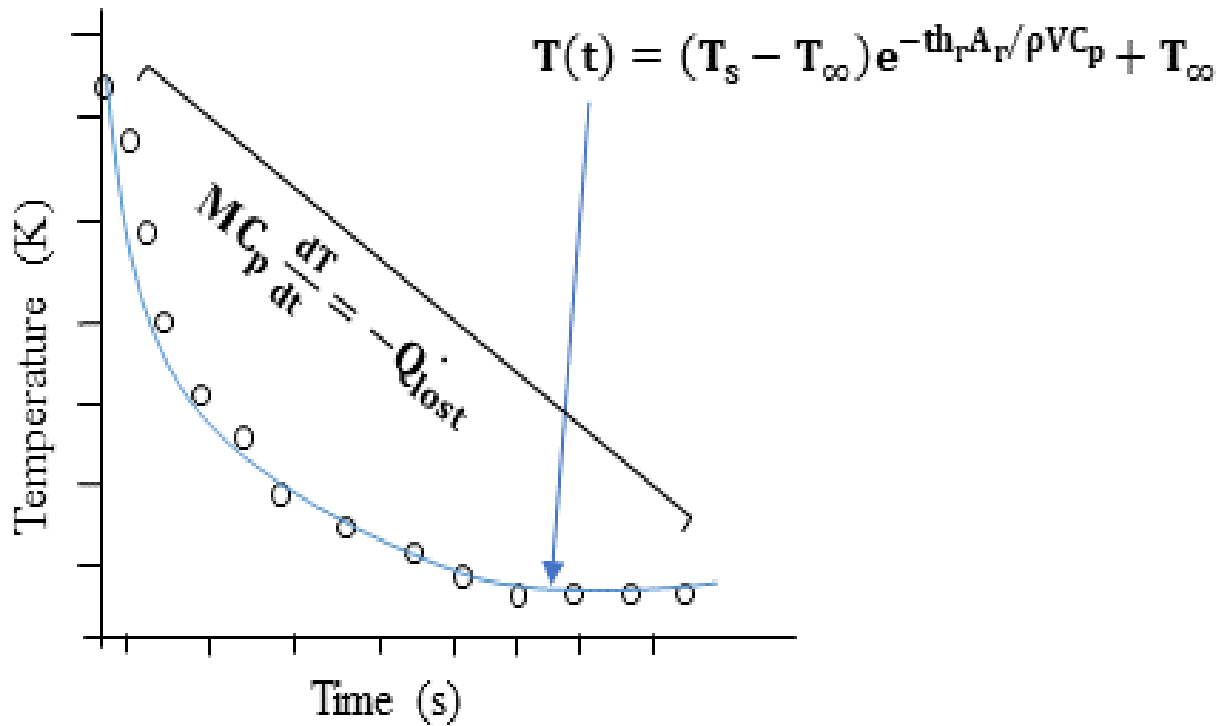


Figure 19: Schematic of thermosiphon PBR's cooling curve illustrating the application of newton's law of cooling for modeling the riser's heat transfer coefficient

$$T(t) = (T_s - T_\infty)e^{\left(\frac{-th_r A_r}{\rho V C_p}\right)} + T_\infty \quad (34)$$

Where  $h_r$  and  $A_r$  are the heat transfer coefficient ( $J/s.K$ ) and area ( $m^2$ ) of the riser section respectively,  $T_s$  and  $T_\infty$  represent the hot water and ambient temperature (k) respectively.

### 3.4.3 LAMP RADIATION MODELING FOR TPBR'S IRRADIANCE

Using the blackbody radiation spectrum of halogen lamps at a color temperature of 2900 K and numerically computing the thermosiphon PBR's available radiant flux density ( $W/m^2$ ) with equation (1) results to an overestimate of the radiant flux density, not practically available for bacterial absorption and attenuation. This is mainly because only a small fraction of the emitted lamp's intensity is in the visible and infrared wavelengths where the photosynthetic bacteria absorb. Therefore, focusing only on the photosynthetically active region (PAR) of the lamp's emission curve (350 to 950), illustrated in Figure 20, and numerically computing the area under that portion,  $A(T_{PAR})$  (equation (35)) will estimate a more appropriate amount of radiant flux density available for bacterial absorption and attenuation.

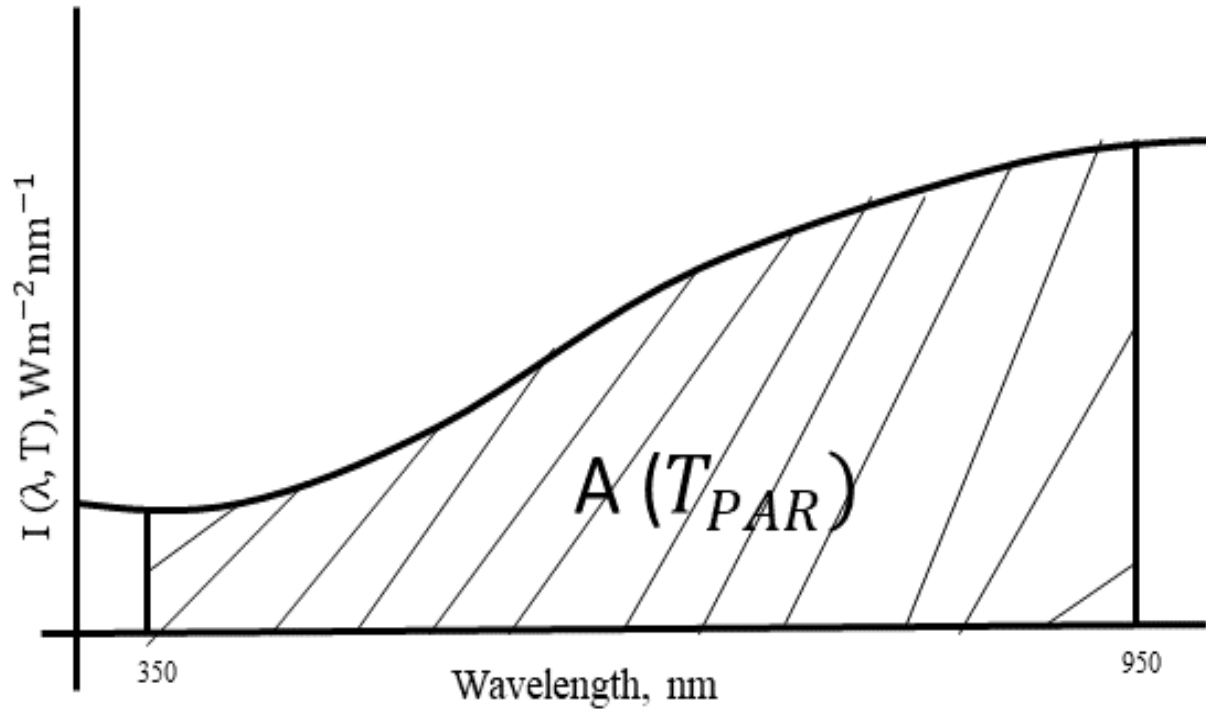


Figure 20: Schematic diagram of the halogen lamp's emission spectral in the photosynthetically active region with the shaded area showing the region for numerical computation of the radiant flux density

$$A(T_{PAR}) = \int_{350}^{950} I(\lambda, T) d\lambda \quad (35)$$

However, the emission spectral of halogen lamps only starts at 380nm as per the manufacturer's specification meanwhile the photosynthetic bacteria absorb in the wavelength range of (400 to 950nm). Therefore, the box model method (Berberoglu et al., 2007) was employed to accurately estimate the weighted average radiant flux density ( $W/m^2$ ) for bacterial absorption at centered wavelength  $\lambda_c$  (400, 500, 600, 700, 800 and 900nm) assigned as midpoint of each box, using 6 boxes of wavelength intervals (350 to 450, 450 to 550, 550 to 650, 650 to 750, 750 to 850, and 850 to 950 nm) such that the area under the original spectrum equals the area under the box (Berberoglu et al., 2007) Figure 21 with (equation (36)).

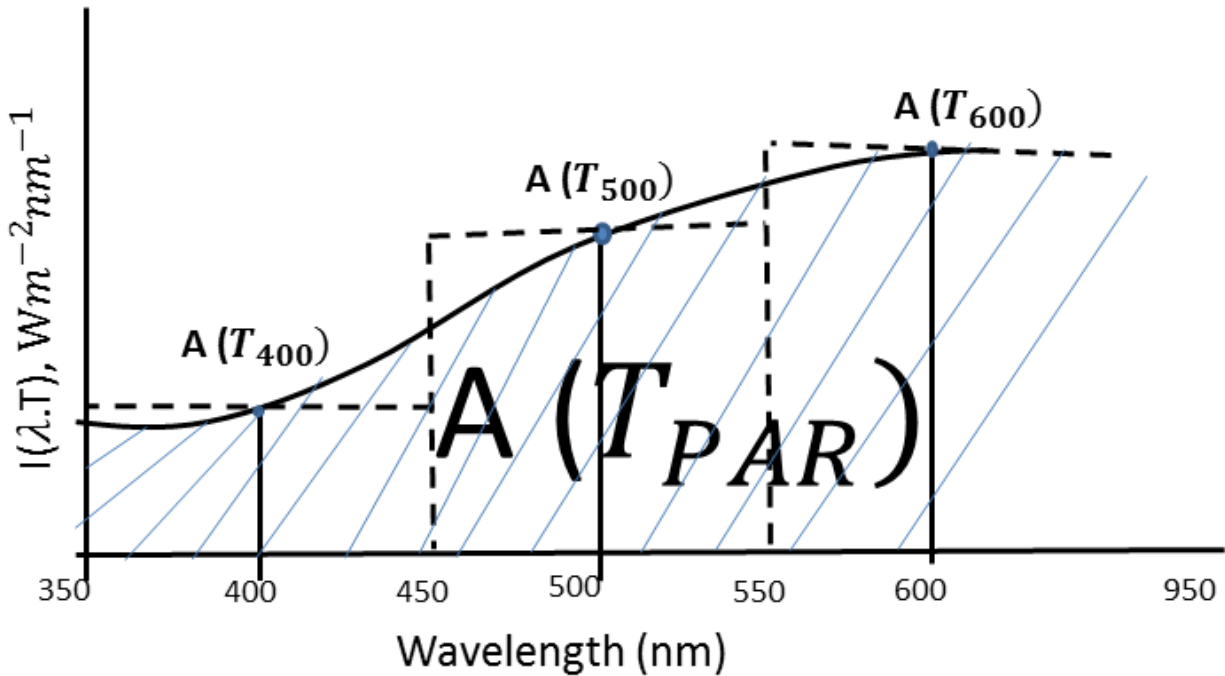


Figure 21: Schematic diagram of the box model applied to the photosynthetically active region of the halogen lamp spectrum

$$A(T_{400}) = \frac{\int_{350}^{450} I(\lambda, T) d\lambda}{10} \quad (36)$$

#### 3.4.4 RATE OF HEATING FROM LIGHT TRANSFER EXPERIMENTS

The *Rhodospseudomonas palustris* within the thermosiphon PBR are living cells, purple in color which absorbs light in the visible and near far infrared wavelengths for their photosynthetic and metabolic heat generation purposes bringing about the thermal effect which induces a temperature differential when the thermosiphon PBR is circulated. That thermal effect has been reported to be a function of the optical properties of the culture (bacterial cell spectral mass extinction coefficient,  $K_b$ , the concentration and morphology of the microbial cells,  $X$ ). Holding these parameters constant, one can investigate the metabolic heat contributions to the overall thermal effect by experimenting with fresh (active) and dead (inactive) bacterial cells at known biomass concentrations within the thermosiphon PBR. That metabolic heat contribution may enhance the thermosiphon PBR's natural convection flow power thereby maintaining more bacterial cells in free suspension, improving mass transfer, and eliminating the light and nutrient gradients through enhanced mixing thereby increasing to increase biomass productivity. The inactivation process of this active bacterial cells (see Figure 22) without tampering on their cell

morphology as well pigment color was achieved by heating the fresh bacterial culture to an inactivation temperature of 70 °C while holding that temperature for 60 minutes.

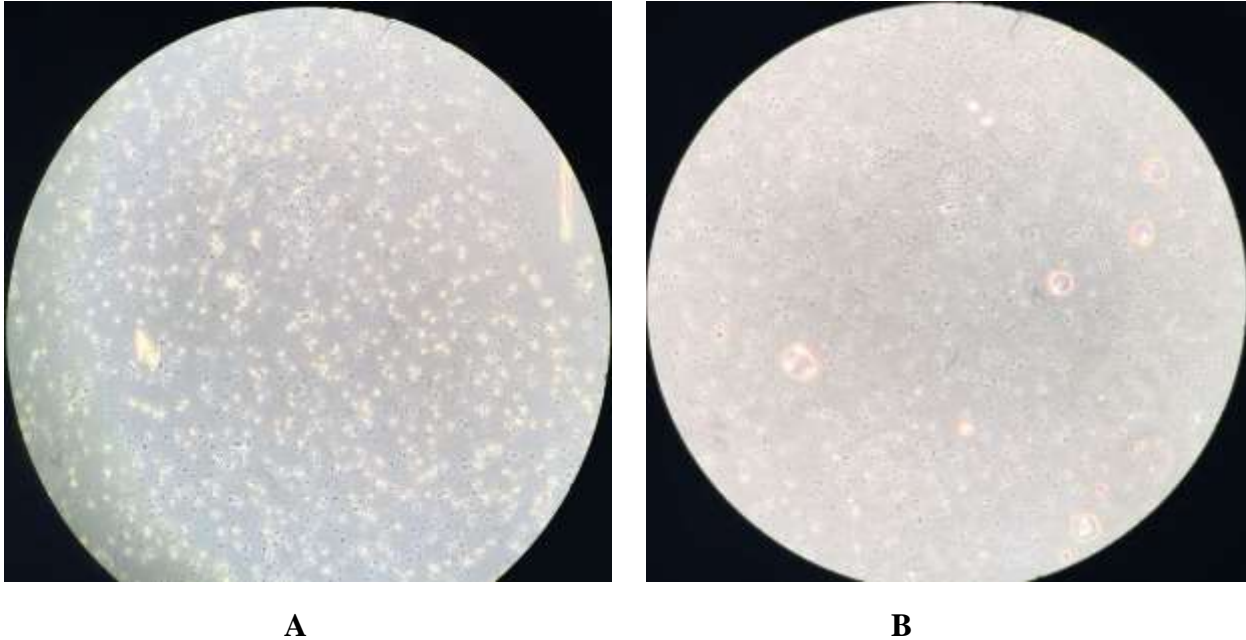


Figure 22: Photograph of (A) active and (B) inactivated *Rhodospseudomonas palustris* under a light microscope with a magnification of 40×

When the thermosiphon PBR is set up for experimental measurement of the rate of heat transfer from the solar simulators as describe in (section 3.4.2 ), the energy balance of the system operating at steady state equation ( $Q_{lights} = Q_{lost}$ ) is modified with equation (equation (37)) to calculated the rate of heat gain by the system from the solar simulators (equation (38))

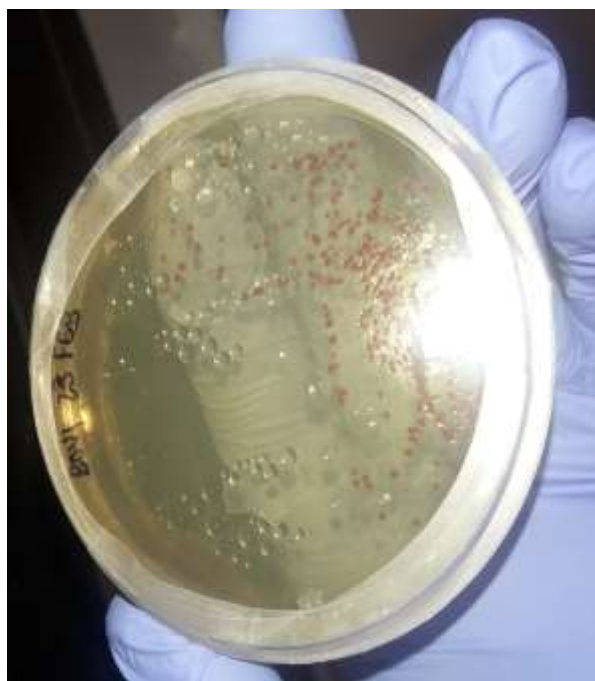
$$Q_{lost} = hA(T_{stab} - T_{w,out}) \quad (37)$$

$Q_{lost}$  is the rate of heat loss (J/s) by the thermosiphon PBR to the circulating cooling water,  $h$  is the heat transfer coefficient of previously estimated (J/s.K),  $T_{stab}$  and  $T_{w,out}$  are the stabilization and outlet cooling water temperatures (K) respectively.

$$Q_{lights} = hA(T_{stab} - T_{w,out}) \quad (38)$$

### 3.4.5 FRESH CULTURING OF BACTERIA FOR ACTIVE EXPERIMENTAL TESTING IN THE TPBR

*Rhodospseudomonas palustris* strain NCIMB 11774 was the photosynthetic bacteria strain selected for use in this study. It was grown in a synthetic medium containing: Glycerol (50mM), Na- glutamate (10mM), yeast extract (0.73M),  $K_2HPO_4$ (0.98M),  $KH_2PO_4$  (1.3M),  $NaS_2O_3 \cdot 5H_2O$  (1M), PABA (15mM),  $MgSO_4 \cdot 7H_2O$  (0.81M),  $CaCl_2 \cdot 2H_2O$  (0.34M), NaCl (6.8M),  $FeC_6H_5O_7$  (20mM), ZnCl (0.51mM),  $MnCl_2 \cdot 4H_2O$  (0.51mM),  $H_3BO_3$  (0.97mM),  $CoCl_2 \cdot 6H_2O$  (0.84mM),  $CuSO_4 \cdot 2H_2O$  (0.12mM),  $NiCl_2 \cdot 6H_2O$  (84 $\mu$ M),  $Na_2MoO_4 \cdot 2H_2O$  (0.17mM), Vitamin B12 (0.73 $\mu$ M), Thiamine (0.45mM) and  $H_2O$  (0.98 mL) with the pH at about  $7.3 \pm$  as shown in (Appendix A). The media was kept sterile by autoclaving at 120°C for 15 mins. Bacterial colonies cultured on agar were picked and resuspended into an airtight 1,000mL Schott bottle containing the growth medium (see Figure 23), and placed into an incubator set at 35°C with about 2500 lux external illumination from a 100 W tungsten lamp. The bacterial inoculum was allowed to grow for 5 days until it reached mid-logarithmic phase with an optical density of around 1.0, and then used for experimental testing in the Thermosiphon PBR.



A



B

Figure 23: Photographs of (A) *Rhodospseudomonas palustris* incubated on agar and (B) planktonic *Rhodospseudomonas palustris* biomass used for all experimental testing



### 3.4.6 FLUID FLOW VISUALIZATION

The hydrodynamics due to mixing in the TPBR were characterized quantitatively through the marker image tracking method (Joshi et al., 2009) and qualitatively by comparing the local velocity fluid flow profile to that of the numerical CFD simulation at the selected riser section. This entailed the drop wise addition of a 3.5M *NaOH* solution through one of the holes on the septum-sealed port at the cap of the TBPR into the working fluid comprising of 5mL Bromothymol Blue indicator (0.4mM), buffer solution (10ml each of  $KH_2PO_4$ (0.12M) and  $K_2HPO_4$ (98mM)) and  $0.5\text{ kg/m}^3$  *Rhodopseudomonas palustris* (fresh and dead). The visualization of color change (yellow to blue color) for both experiments containing fresh and dead *Rhodopseudomonas palustris* was focused on the riser section. The propagated color change through the buoyancy flow field of the riser's bottom (point A) to the top (point B),  $D_{AB}$  with respect to time ( $T_{AB}$ ) was recorded with a digital camera (SAMSUNG RF8JA1C8BRN, Taiwan). Quantitative analysis was carried out by calculating the riser's flow velocity with (equation (39)) and compared to that predicted by the CFD simulations. At the same time, the recorded flow video was intercepted at 15s intervals to produce photos which were then qualitatively compared to the CFD simulations flow mixing.

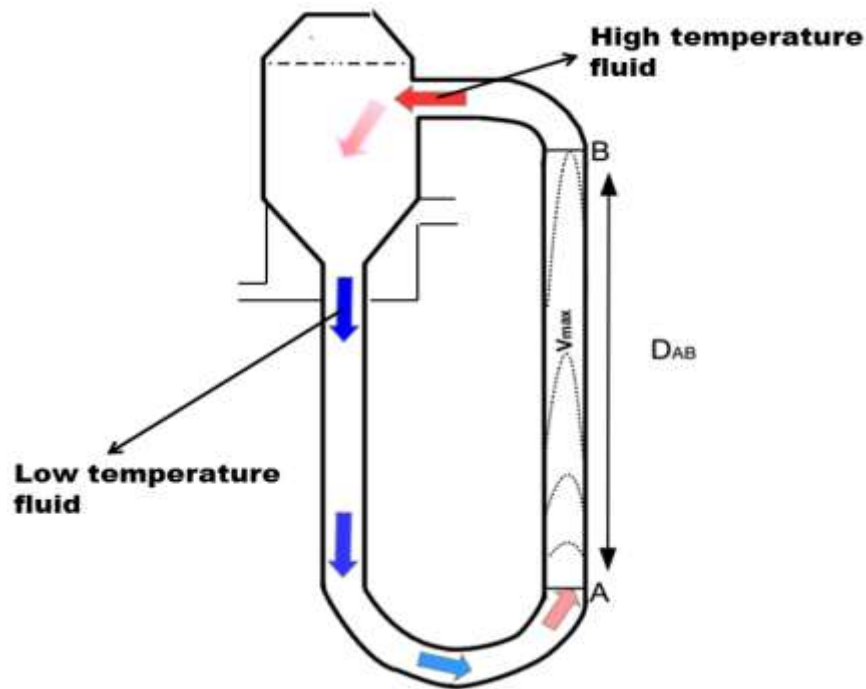


Figure 24: Schematic diagram for the estimation of local flow velocity through the riser section

$$V_{AB} = \frac{D_{AB}}{T_{AB}} \quad (39)$$

### 3.4.7 SEDIMENTATION EXPERIMENT

The rate of cell circulation and settling in the thermosiphon PBR was investigated by monitoring the biomass concentration in the storage tank over time for the fresh and dead bacterial cells. This entailed collecting 5mL samples at 60 minutes intervals with a syringe through one of the holes on the septum-sealed port at the cap of the thermosiphon BPR and calculating its cell dry weight from absorbance measurement with UV/VIS spectrophotometer (Model AE-S60-4U, A&E lab (UK) Co., Ltd) at 660nm using a calibration curve. The rate of cell settling ( $X_{s_t}$ ) was calculated by deducting the bacterial cell concentration in free suspension ( $X_t$ ) from the known initial biomass concentration ( $X_0$ ) as per (equation (40)) and illustrated on Figure 25 and Figure 26.

$$X_{s_t} = X_0 - X_t \quad (40)$$

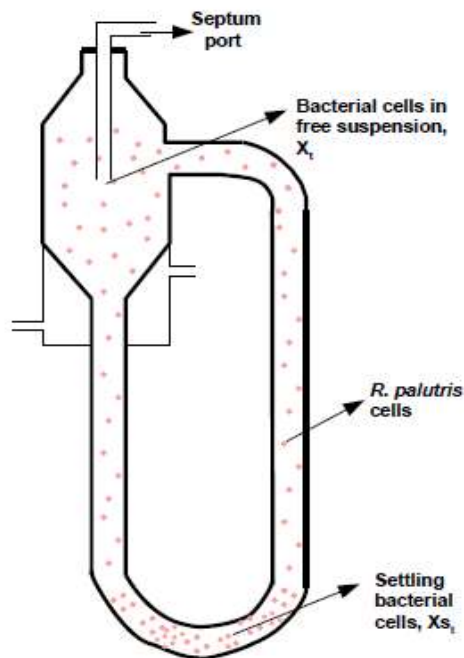


Figure 25: Schematic diagram for the estimation of biomass settling rate

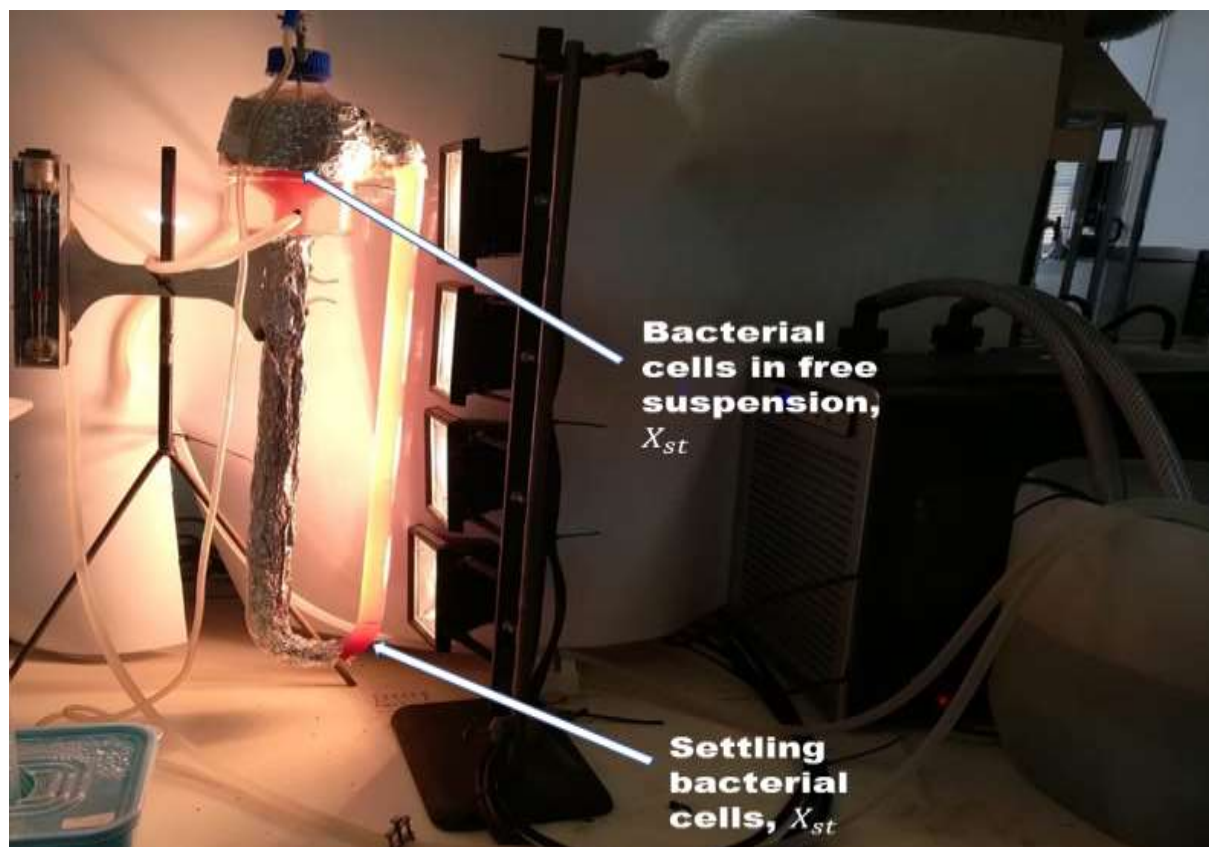


Figure 26: Photograph of the experimental setup illustrating the estimation of biomass settling

### 3.5 COMPUTATIONAL FLUID DYNAMICS MODELING

The CFD passive fluid flow and heat transfer analysis within the thermosiphon PBR was performed using the commercial CFD package ANSYS Fluent, version 17.2 which is based on the finite volume method (ANSYS Fluent, 2016). The geometry creation was the first step and a simplified 2D model from the 3D cylindrical domain has been considered here using the DesignModeler software as shown in Figure 27 (A) and (B). In essence, this approach minimizes the computational cost by enabling the CFD model to easily predict the experimental scenario within a shorter time. The computational domain had a height of 0.65m corresponding to the dynamic liquid level observed in experiments with the physical model. The mesh generation within the computational domain was attained with the Mesher of FLUENT, shown in Figure 27 (C) and (D). The mesh was composed of 49,566 fine element sizes with their quality reported in Table 9. This mesh was not uniform throughout the computational domain as boundary layer inflation (5 rows of mesh with size of 0.1 mm and growth factor of 1.2 (Alizadehdakheel et al.,

2010)) was used to ensure sufficient resolution of detail in the near wall regions with significant thermal and momentum gradients.

Table 9: Mesh quality details

<b>Mesh Metric</b>	<b>Minimum value</b>	<b>Maximum value</b>	<b>Average value</b>
Orthogonality	0.6291	1.0	0.99373
Skewness	1.3057e-010	0.58139	2.3036e-002
Aspect ration	1.0	10.003	2.289

This discretization enabled the governing equations (equation (10) to (12)) to be solved numerically by iteration at specific locations while assuming the flow to be laminar without viscous heating (Louisos et al., 2013), incompressible and non-reactive with constant physical properties (e.g.  $C_p$ ,  $k$ ,  $\rho$ ,  $\mu$ ) of water operating at 303.15 k in the formulation of the buoyancy term since as the bacteria cell dried weight and nutrient concentrations are very low compared to the volume of water within the reactor (Gandhi et al., 2011; Malik et al., 2013) as illustrated in Table 10. The boussinesq approximation was also incorporated into the model to account for buoyancy driven convection as the working fluid (mostly water) density changes induced by temperature field according to (equation (41)) (Gandhi et al., 2011; Malik et al., 2013).

$$\rho = \rho_{\infty}[1 - \beta(T_s - T_{\infty})] \quad (41)$$

Where  $\beta = 1/T_{\infty}$  ( $K^{-1}$ ) is the coefficient of thermal expansion (Louisos et al., 2013),  $\rho_{\infty}$  is the water density,  $T_{\infty}$  is the ambient temperature and  $T_s$  is the operating temperature.

Table 10: Thermophysical properties of water (Lide, 2003)

<b>Properties</b>	<b>Units</b>	<b>Value</b>
Specific heat capacity	$JKg^{-1}K^{-1}$	4178.4
Density	$Kgm^{-3}$	995.65
Thermal expansion coefficient	$K^{-1}$	0.000303
Dynamic viscosity	$Kgm^{-1}s^{-1}$	0.000798
Thermal conductivity	$Wm^{-1}K^{-1}$	0.616

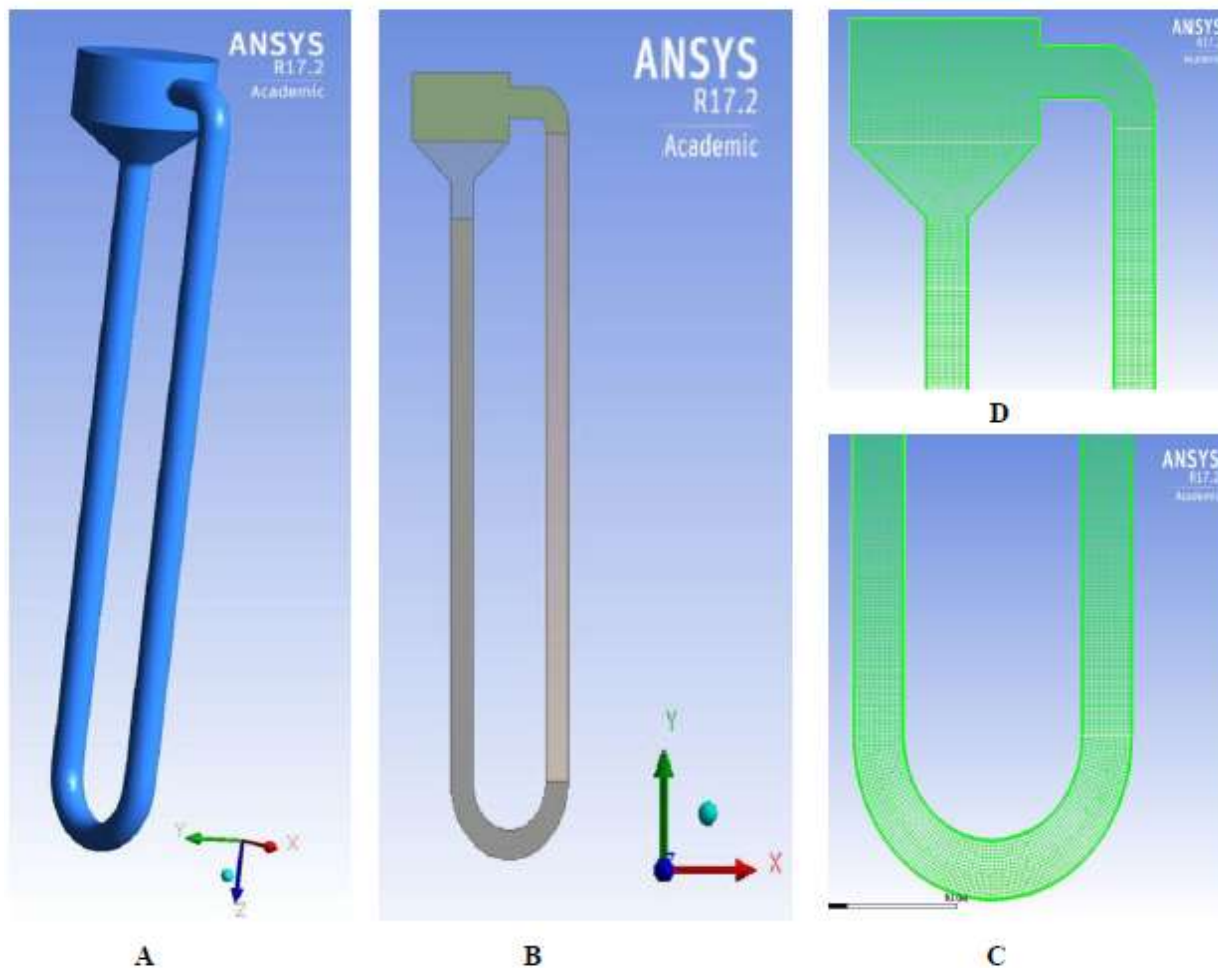


Figure 27: (A) and (B) are the 3D and 2D Thermosiphon PBR reactor geometries while (B) and (C) are the element meshing used at the top and bottom sections of the reactor respectively

### 3.5.1 BOUNDARY CONDITIONS

A non-slip boundary condition is applied to all the walls except for the top water surface which was defined as a free surface with constant shear (free slip) at an atmospheric pressure of 1 atmosphere (101.325 KPa) from the reference pressure point (Gandhi et al., 2011; Louisos et al., 2013; Xu et al., 2014). In order to simulate light transmission and non-uniform sensible heat generation, a user defined function (UDF) from (equation (29)) is interpreted and hooked to the riser cell zone. A zero-heat flux was assigned to all the walls as adiabatic sections assuming no heat is gain or lost because they are thermally insulated except for the riser and cooling wall sections where a convection heat transfer coefficients of  $1.46 \text{ J/s.K}$  and  $202.06 \text{ J/s.K}$  were

defined as boundary conditions. A body force term of  $9.8 \text{ ms}^{-2}$  was used as the acceleration due to gravity while an experimentally observed operating temperature of 303.15 K was assigned.

### 3.5.2 SOLUTION STRATEGY AND CONVERGENCE CRITERION

The numerical simulations were run on an i7-4510U CPU 2.00GHz 2.60GHz processor Intel(R) computer with 16 GB RAM and 64 bit operating system (Dell Inc., Stellenbosch, South Africa) using the pressure-density based solver and a combination of SIMPLE algorithm for pressure-velocity coupling and Second Order Upward Schemes for momentum and energy discretization (Basak et al., 2016; Louisos et al., 2013; Malik et al., 2013; Rek et al., 2012). An unsteady simulation with a step time of 0.01s and time step size of 5,000 was employed to model the dynamic behavior of the TPBR since it experiences a high temperature to velocity coupling to drive the buoyancy flow (Alizadehdakhel et al., 2010; Fadhl et al., 2013; Roldán, Smirnova, Fend, Casas, & Zarza, 2014). The under relaxation factors were 0.3 for pressure, 0.6 for momentum and 0.8 for energy and radiation as defined by (Rout, Thatoi, Acharya, & Mishra, 2012a). The pressure discretization used Body-force-weighted Schemes while the Green-Gauss scheme is used for spatial discretization (Louisos et al., 2013; Rout, Thatoi, Acharya, & Mishra, 2012b). The numerical computations in this study were considered converged when the scaled residuals for continuity, momentum and energy components had fallen below  $10^{-3}$  and  $10^{-6}$  respectively, as used by other researchers (Alizadehdakhel et al., 2010; Basak et al., 2016; Fadhl et al., 2013; Rek et al., 2012; Williamson & Wilson, 2009). Generally, it took 60.1s and 103,348 iterations for the simulation to converge.

## 3.6 ANALYTICAL METHOD

### 3.6.1 CELL CONCENTRATION

The bacterial cell concentration was determined with a UV/VIS spectrophotometer (Model AE-S60-4U, A&E lab (UK) Co., Ltd) at 660nm using distilled water as a blank solution. An OD660 of 1.0 corresponded to 0.7172 g dry weight/L for *Rhodopseudomonas palustris* according the setup calibration curve Figure 28

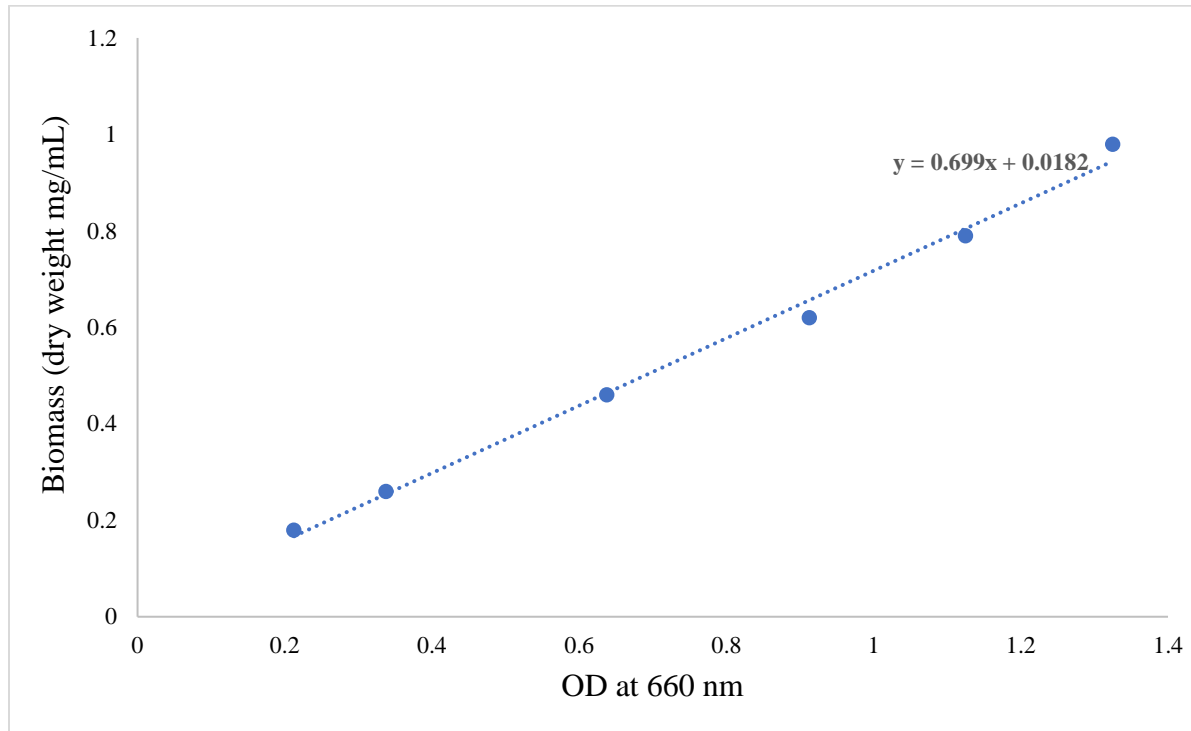


Figure 28: Biomass calibration curve of *Rhodopseudomonas palustris* used to convert absorbance to biomass. Reproduced from the original experimental graph established by (J.P. du Toit, 2017)

## CHAPTER FOUR

### RESULTS AND DISCUSSIONS

The use of CFDs and experimental validation for the development of the thermosiphon PBR led to a series of investigations which the results are presented and discussed in this chapter of the thesis. This chapter is broken down into six subchapters: parameters used for CFD model, CFD simulation results, flow visualization results, validation results, and effects of light absorption on the heating rate and thermosiphoning cells respectively.

#### 4.1 SPECTRAL PARAMETERS USED IN CFD MODELING

This subchapter contains the results and discussion of the experiments designed for the investigation of the relevant CFD modeling parameters. It starts by discussing the results of the halogen lamps as an illumination source for the thermosiphon PBR, followed by the spectral attenuation properties of active *Rhodoseupdomans palustris* cells and finally the measured heat transfer coefficient of the thermosiphon PBR system.

##### 4.1.1 RESULTS OF HALOGEN LAMP RADIATION MODEL

The spectral existence,  $I(\lambda, T)$  which is the flux of power per unit area per wavelength predicted by the Planck's radiation equation (1) for a perfect blackbody at a color temperature of 2900K is displayed in Figure 29. This emission spectral of the halogen lamp compares very well with that reported in literature (Cengel & Ghajar, 2011; MacIsaac et al., 1999). The spectral existence is seen to be lowest in the ultraviolet region, small in the visible region and highest in the infrared wavelengths regions. This implies that the emission spectra of the halogen lamps produce mostly long wavelength than short wavelength radiations as was expected. This confirms that they are not suitable for plants and microalgae whose absorption is in the visible region (relatively short wavelength region) but highly efficient for photosynthetic bacteria whose absorption is in the visible region, as well infrared region (long wavelength region). Also, with the specific energy content being inversely proportional to wavelengths, the photosynthetic pigment molecules of the bacteria: carotenoid and bacteriochlorophylls, will each experience minimal ionizing effects but however, immensely thermal effects respectively. Therefore, the sensible volumetric heat generation will be greatest for the thermosiphon PBR being illuminated by halogen lamps as to



compare to other existing light sources like cool white fluorescent, Gro-lux, AlInGAP II LED and GaAlAs LED etc.

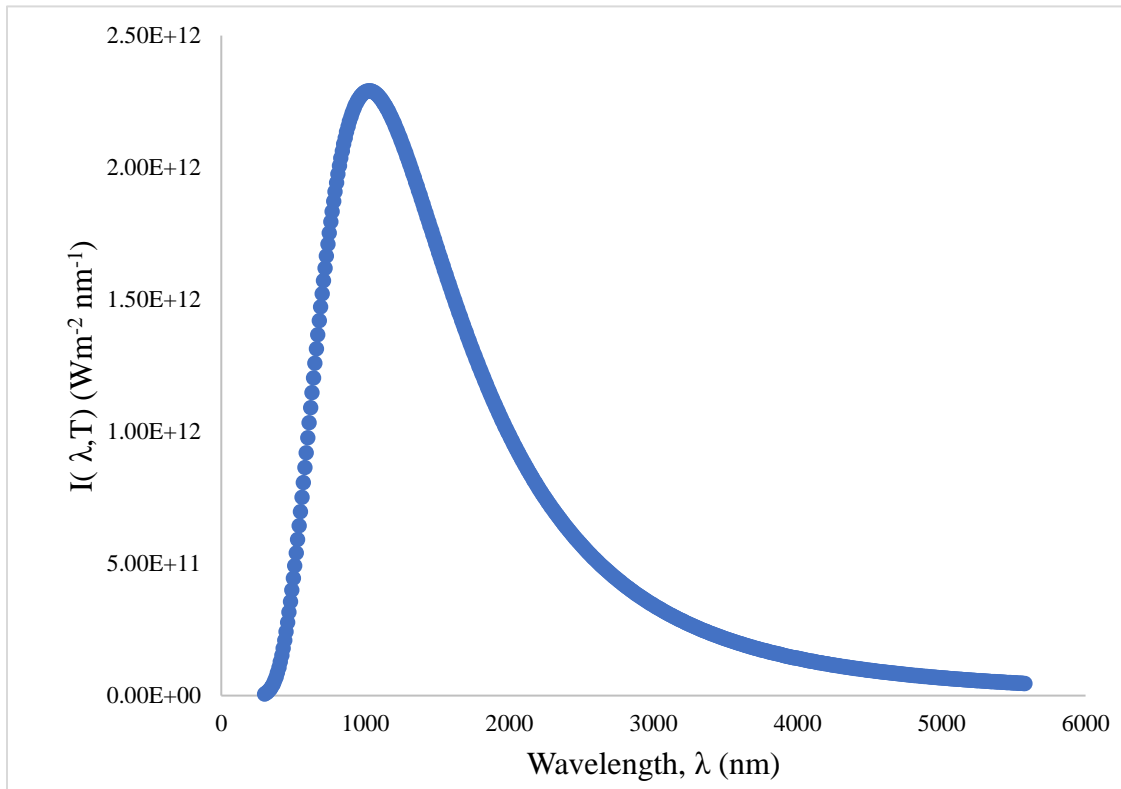


Figure 29: Blackbody radiation curve of halogen lamp used as solar simulators at a color temperature of 2900K

However, the emission spectrum in Figure 29 extends to wavelength regions of over 6000 nm where the photosynthetic bacteria do not absorb. Therefore, using this entire spectrum for radiant flux calculation will result to an over estimation of radiant flux which is either not been produced by the experimental halogen lamp or available for absorption by the photosynthetic bacteria. With the box method applied to easily perform the numerical integration over the PAR Figure 30, the actual average weighted radiant flux density ( $\text{W/m}^2$ ) available for bacterial absorption is reported in Table 11. The data reveals that the available radiant flux for bacterial absorption increases with an increasing wavelength. This confirms that the volumetric heating effect will be minimal at the short wavelengths, 400nm but increases as the wavelength approaches 900nm. This was then used as irradiance on the riser section of the thermosiphon PBR for the radiative transport equation as shown in the UDF (see APPENDIX A).

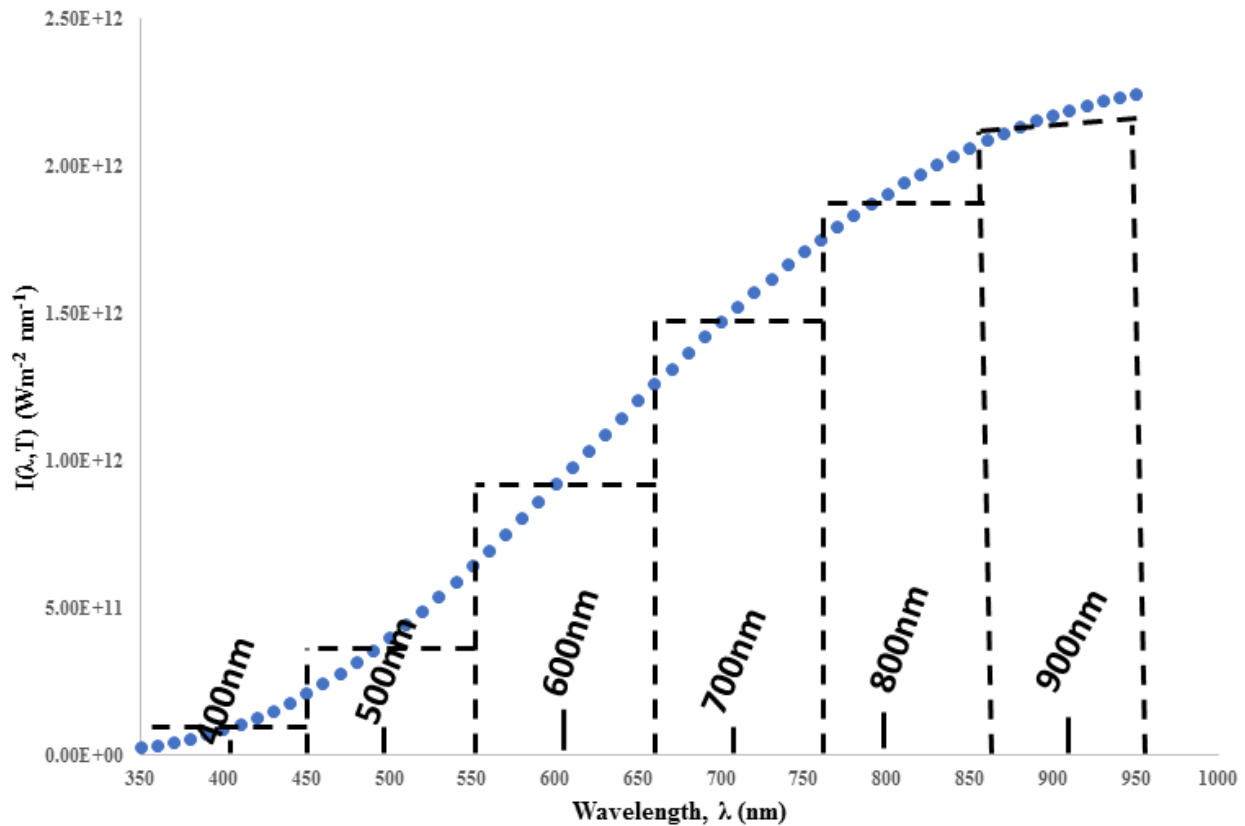


Figure 30: The box model applied to the photosynthetically active part of the Halogen lamp emission spectrum

Table 11: Summary of average weighted radiant flux density numerically computed with the box model

Box	Wavelength, $\lambda_c$ (nm)	Radiant flux, $I(T)$ ( $10^3 W/m^2$ )
1	400	1.43
2	500	5.25
3	600	11.06
4	700	16.94
5	800	21.45
6	900	24.12

#### 4.1.2 SPECTRAL EXTINCTION COEFFICIENT OF *R. PALUSTRIS*

The governing radiative transport equation (RTE) takes into account the spectral intensity as well as the spectral extinction properties of the medium. Therefore, the spectral extinction coefficient of *Rhodopseudomonas palustris* was measured to accurately model the light transfer within an absorbing medium. The absorbance of *Rhodopseudomonas palustris* at five different biomass concentrations ( $Kg/m^3$ ): 0.16, 0.27, 0.38, 0.49 and 0.59 in the spectral range from 400 to 900 nm were measured with UV spectrophotometer. The measurements were performed in triplicates and the arithmetic mean of the result was plotted against its wavelength absorbance as illustrated in Figure 31. This showed the bacterial wavelength absorbance to increase with an increasing biomass concentration. This pattern has been reported for another photosynthetic bacteria like *Rhodobacter sphaeroides* ATCC 49419 (Berberoglu & Pilon, 2007), and even cyanobacteria like *Anabaena variabilis* ATCC 29413-U (Berberoglu & Pilon, 2007). This confirms that more light is been absorbed in an optical thick medium and contributes greatly to increasing the sensible volumetric heating of photobioreactors via fluorescence and waste metabolic heat. The linear regression between absorbance (Ab) at each wavelength and biomass concentration (X) was performed to estimate the spectral mass extinction coefficient  $K_b$  as defined in (equation (30)), and reported in Table 12. Figure 32 shows the spectral mass extinction coefficient of *Rhodopseudomonas palustris* within the spectra range from 400 to 900 nm. This mass extinction coefficient includes the specific wavelength absorbance of the photosynthetic pigments plus the light scattered within that wavelength. Generally, the bacteria's mass extinction coefficient levels from 400 to 500 nm, decreases from 500 to 700 nm, peaks at 800 nm and then decreases to 900 nm. This implies that *Rhodopseudomonas palustris* has two light absorptions peaks: around 500nm and 800nm which falls in the visible and infrared regions of the electromagnetic spectrum respectively. Also, they correspond to the absorption peaks of carotenoid and bacteriochlorophylls which are the main photosynthetic pigments responsible for that light absorption in photosynthetic bacteria like *Rhodopseudomonas palustris*. This is in confirmation with the several published literature about the bacteria's photosynthetic activity region (PAR)(Nogi et al., 1985; Pilon et al., 2011).

Table 12: Spectral attenuation parameters of *Rhodospseudomonas palustris*

Wavelength (nm)	Slope ( $m^3/Kg$ )	$K_b(m^2/Kg)$
400	2.2042	220.42
500	2.2344	223.44
600	1.7231	172.31
700	1.2378	123.78
800	1.7758	177.58
900	1.2465	124.65

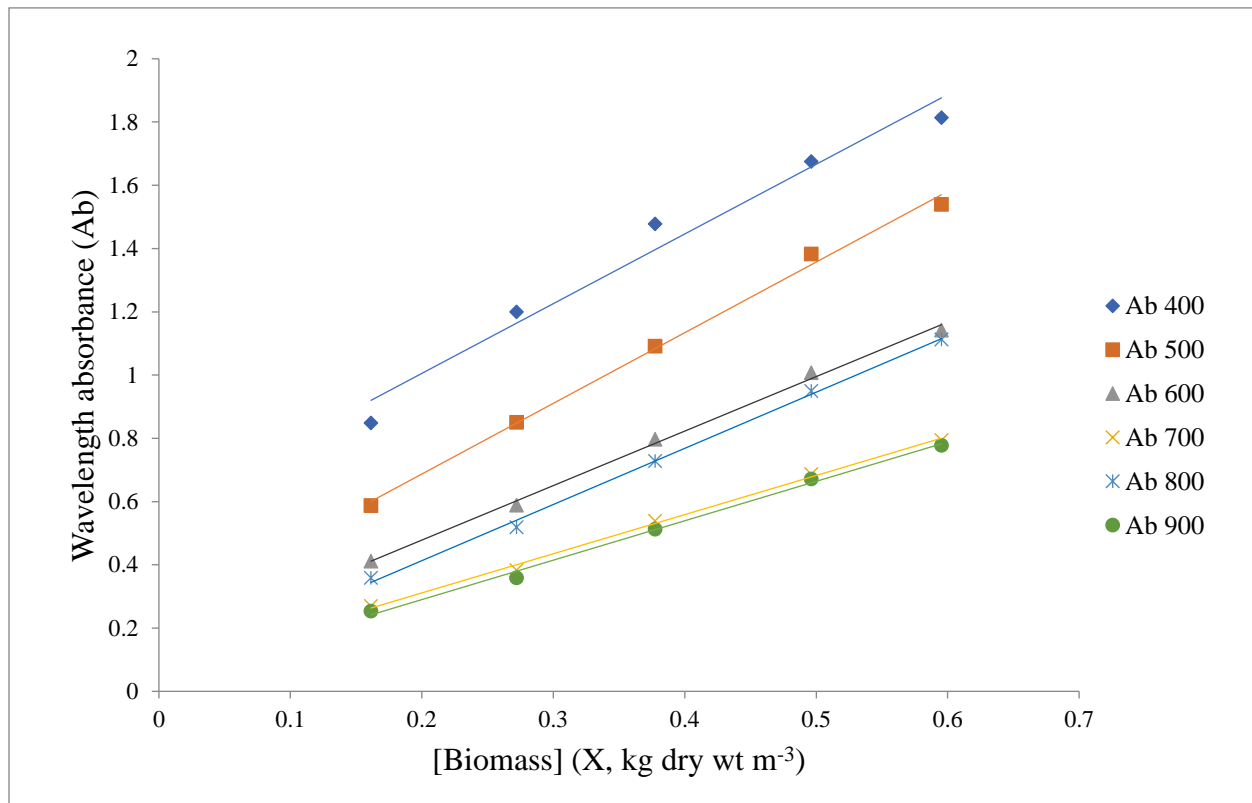


Figure 31: Linear regression between absorbance (Ab) and biomass concentration (X) at various wavelength (400 to 900 nm)

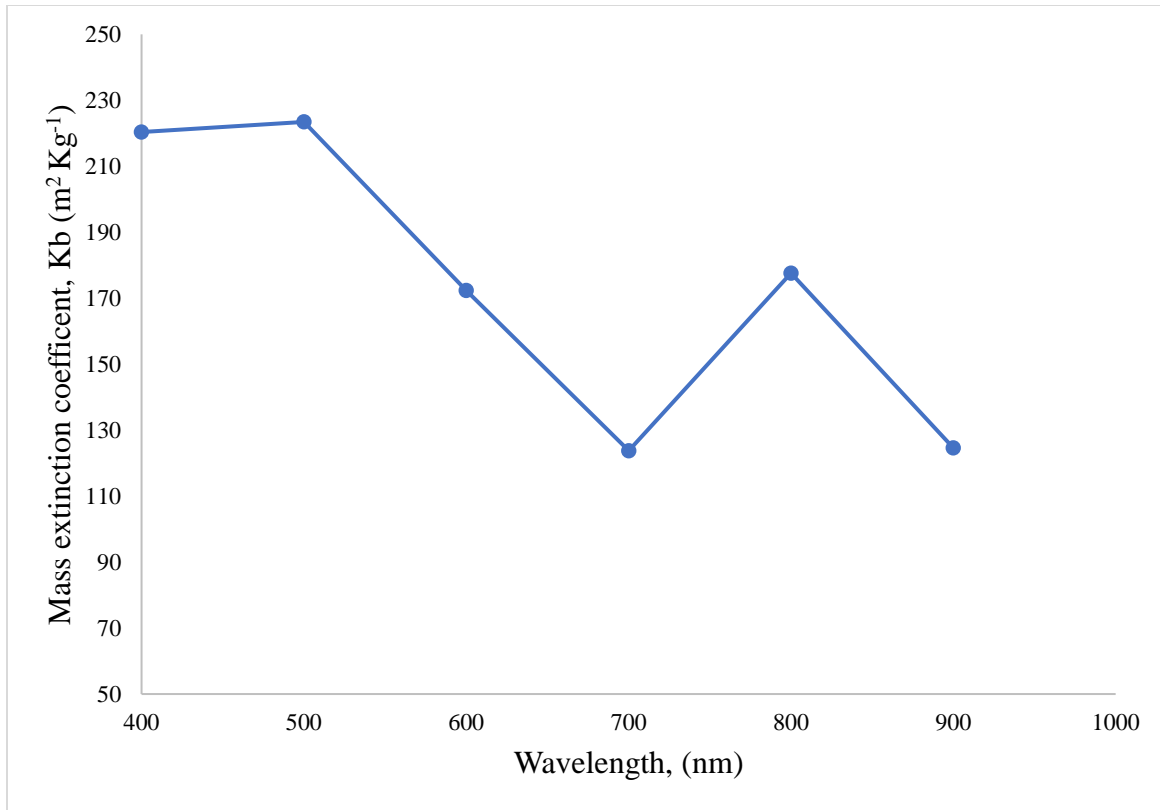


Figure 32: Spectral extinction coefficient of *Rhodospseudomonas palustris* measured at five different biomass concentrations from 400 to 900 nm

#### 4.1.3 RESULTS OF HEAT TRANSFER MEASUREMENTS

The thermal balance on the thermosiphon PBR system showed that its medium temperature is controlled by (i) radiative heat transfer from the halogen lamps, (ii) metabolic heat exchange within the system, (iii) convection heat transfer from the air surrounding the thermosiphon PBR, and (iv) convection heat transfer to circulating water at the cooler section of the thermosiphon PBR. Also, the heat transfer and natural fluid circulation within the thermosiphon PBR are directly coupled since as it's responsible for the temperature-induced density variation. Most modeling studies assume the existence of a forced convection correlation which enables them to calculate the heat transfer coefficient by knowing the flow regime and flow profile. However, this approach is inappropriate for the TPBR because of the direct coupling between the external heat transfer and the circulating fluid's density, which are unique for the experimental setup. Therefore, the heat transfer coefficient of thermosiphon PBR's cooler and riser sections were estimated with Newton's law of cooling by curve fitting equation (33) and (34) respectively with experimental data. For heat transfer coefficient of the cooling walls, the arithmetic mean of the three different center-pipe temperature vs time data for the thermosiphon PBR operating under biomass loading of  $0.5 \text{ Kg/m}^3$  active *Rhodospseudomonas palustris* cells was calculated and used for the curve fitting.

Figure 33 shows that the curve fits very well from the steady state temperature of 315.06k to the ambient cooling water temperature. Hence, the numerical estimation of the cooling wall's heat transfer coefficient was  $202 \text{ W/m}^2\text{K}$ . This value implies that the thermosiphon PBR's cooling walls were experiencing heat transfer to the circulating subcooled water by forced convection since as its heat transfer coefficient fell within the range of forced convection by external means ( $10\text{-}75,000 \text{ W/m}^2\text{K}$ ) (Ansys Fluent, 2016). On the other hand, for the heat transfer coefficient of the thermosiphon PBR's riser walls, the arithmetic mean of the three different center-pipe temperature vs time data for the thermosiphon PBR operating under hot water at about 341.7K and cooling to environment's ambient temperature was calculated and used for the curve fitting.

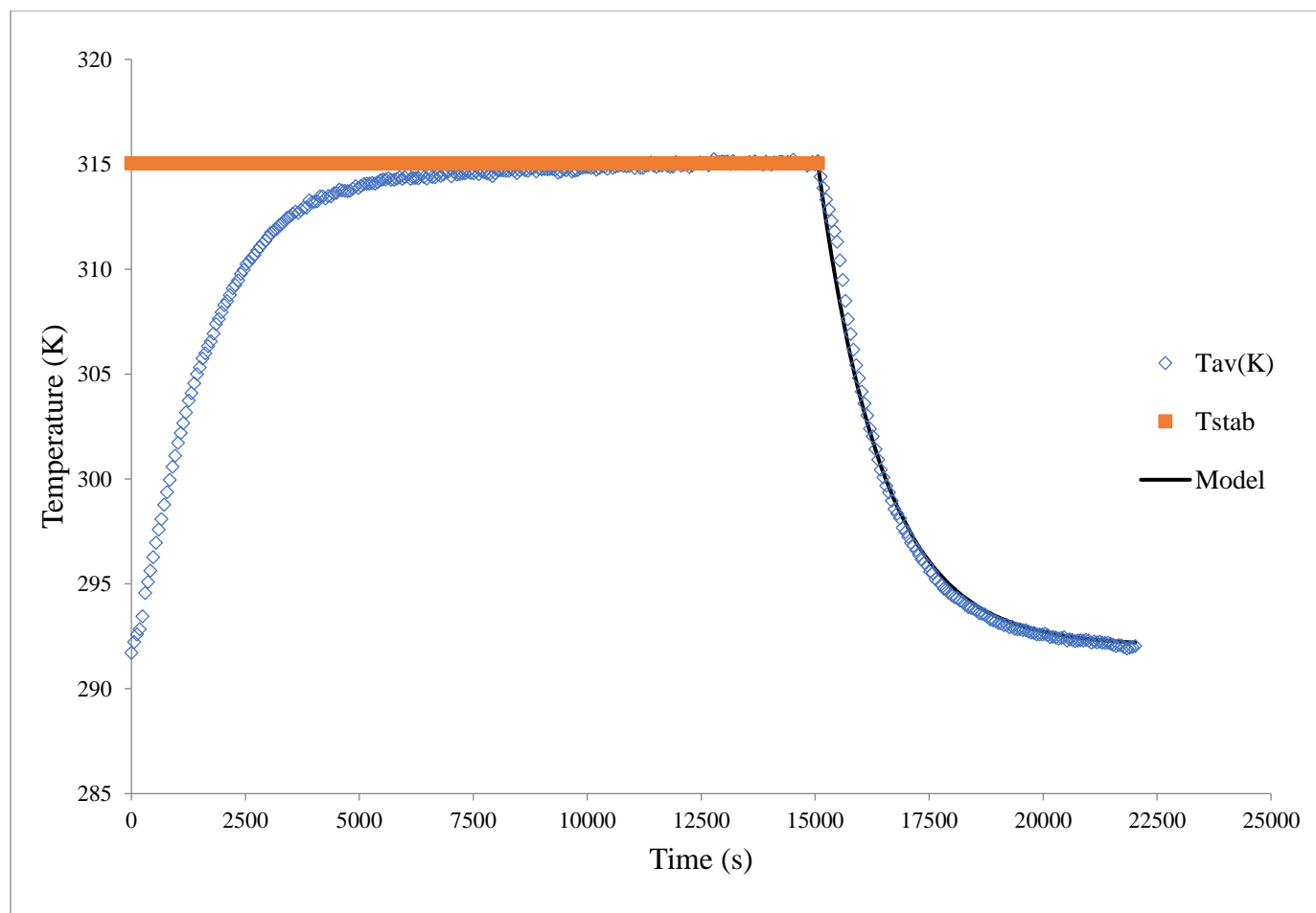


Figure 33: Temperature of thermosiphon PBR as a function of time for the three thermocouple sensor positions. Experimental data (average temperature,  $T_{av}$  and stabilization temperature,  $T_{stab}$ ): from startup to thermal equilibrium indicated with symbols while theoretical curve (model); illumination switch off after 15000 s indicated with a solid line.

Figure 34 shows that the curve fits very well and the heat transfer coefficient of the riser walls was numerically estimated to be  $2 \text{ W/m}^2\text{K}$ . This value implies that the thermosiphon PBR's riser walls were losing heat to the environment via natural convection since its heat transfer coefficient is far below that of forced convection. This was in accordance with our expectations and the values were used for the CFD simulations of thermosiphon PBR's heat transfer and buoyancy driven flow.

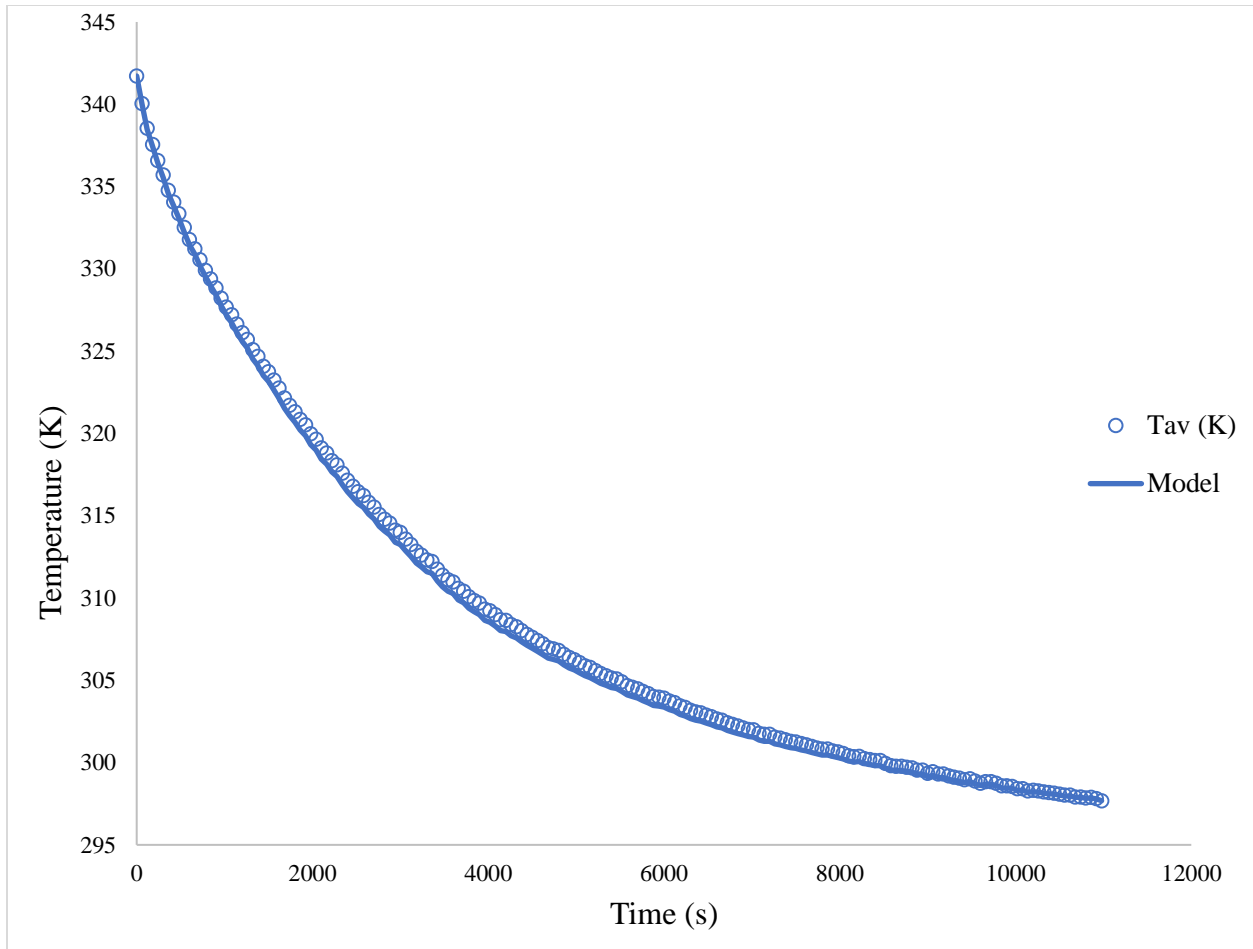


Figure 34: Temperature of the hot water in thermosiphon PBR as a function of times for the three thermocouple sensor positions. The experimental data (average temperature,  $T_{av}$ ) and theoretical curve (model) are indicated with symbols and lines respectively.



## 4.2 CFD SIMULATIONS RESULTS

This section contains the thermosiphon BPR's CFD simulation results and discussion. The model was setup in ANSYS Fluent version 17.2 and activated for 2D, transient, boussinesq approximation, thermophysical properties of water, radiation transfer User-Defined Function (UDF), and heat transfer coefficient of the riser and cooling walls. The converged solution was post-processed to allow for simple interpretation of the results. The results were obtained in terms of temperature (K) and velocity (m/s) distributions in the working fluid and presented by the means of contours and vectors plots for the modeled variables. This allowed for qualitative analysis by providing a more comprehensive visualization of the thermosiphon PBR operation. (see the attached compact disc (CD) for the ANSYS reported html file for the CFD simulations results).

### 4.2.1 TEMPERATURE DISTRIBUTION

The CFD predicted temperature distribution of the thermosiphon PBR is discussed here. As well, the CFD simulated temperature distribution was probe at three positions corresponding to the three experimental center-pipe thermocouple locations for monitoring the thermosiphon PBR's five main sections (storage tank, cooling, downcomer, riser and upper bend sections).

Figure 35 shows the temperature distribution of the working fluid within the thermosiphon PBR and it can be seen that the circulating fluid is thermally heterogeneous. However, areas of high temperatures are observed to occupy the thermosiphon PBR's top section (upriser and storage tank section) while those of relatively lower temperature settle in the bottom (downcomer section). This simulation result verifies the hypothesis that buoyancy effects characterize the temperature distribution and fluid flow within the thermosiphon BPR since as fluid of lower density is floating while that of higher density is settling. This is even more conspicuous at the cooling wall sections where parallel temperature lines show the decrease of the working fluid's temperature as it propagates through the downcomer.

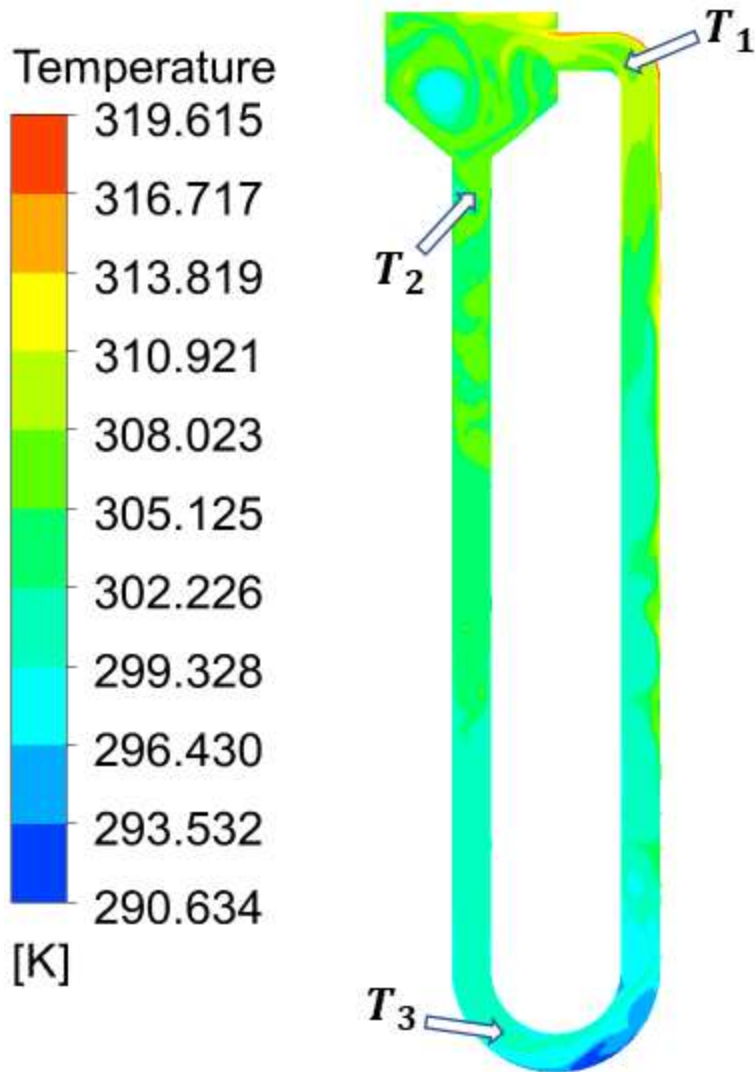


Figure 35: Temperature contours of CFD steady state simulations showing the temperature notation points, which correspond to the thermocouple positions in the experimental set-up

Another important observation is made at the cooling and riser section where the working fluid's temperature distribution is observed to be highly stratified as seen in Figure 36. This is presumed to be the result of force convection of the subcooling water at the cooling walls and light attenuation in the riser section respectively. The defined heat transfer coefficient of the cooling walls brought about its rapid cooling as the sidewalls had a significantly lower temperature as to compare to the inner annulus of cooling section. On the other hand, the UDF implemented radiative transfer equation (RTE) was responsible for the non-uniform, left to right temperature

stratification through the riser's cross section. This is in accordance with the hypothesis of the non-uniform volumetric heating being dependent on the attenuated light from the front irradiated wall surface to the reactor center and rear surface according the famous Beer-Lambert law (Luo & Al-Dahhan, 2004, 2011) which is highly heterogeneous in the presence of bacterial cells (Benson & Rusch, 2006) and for buoyancy forces in these cases.

The stratified nature of the riser's temperature predicted by the CFD model agrees very well with the results presented by (Roldán et al., 2014) in the thermal analysis of a volumetric solar absorber. However, their result cannot be directly used to match the thermosiphon PBR's CFD model since their solar absorber was made of a solid material with gradual changing porosity. Other thermosiphon CFD analyses focus mostly on the quantitative validation of probed temperature readings, mainly because the temperature distribution in the absorber/solar collection are very uniform or homogenous since as they defined either a constant wall temperature or uniform surface flux heating. Their modeling methodology is practically limited to situations where the absorbers/solar collectors are coated with black material to enhance solar absorption. However, this was not the practical case for the thermosiphon PBR whose riser walls were transparent to enhance light penetration and available for microbial absorption as the design consideration.

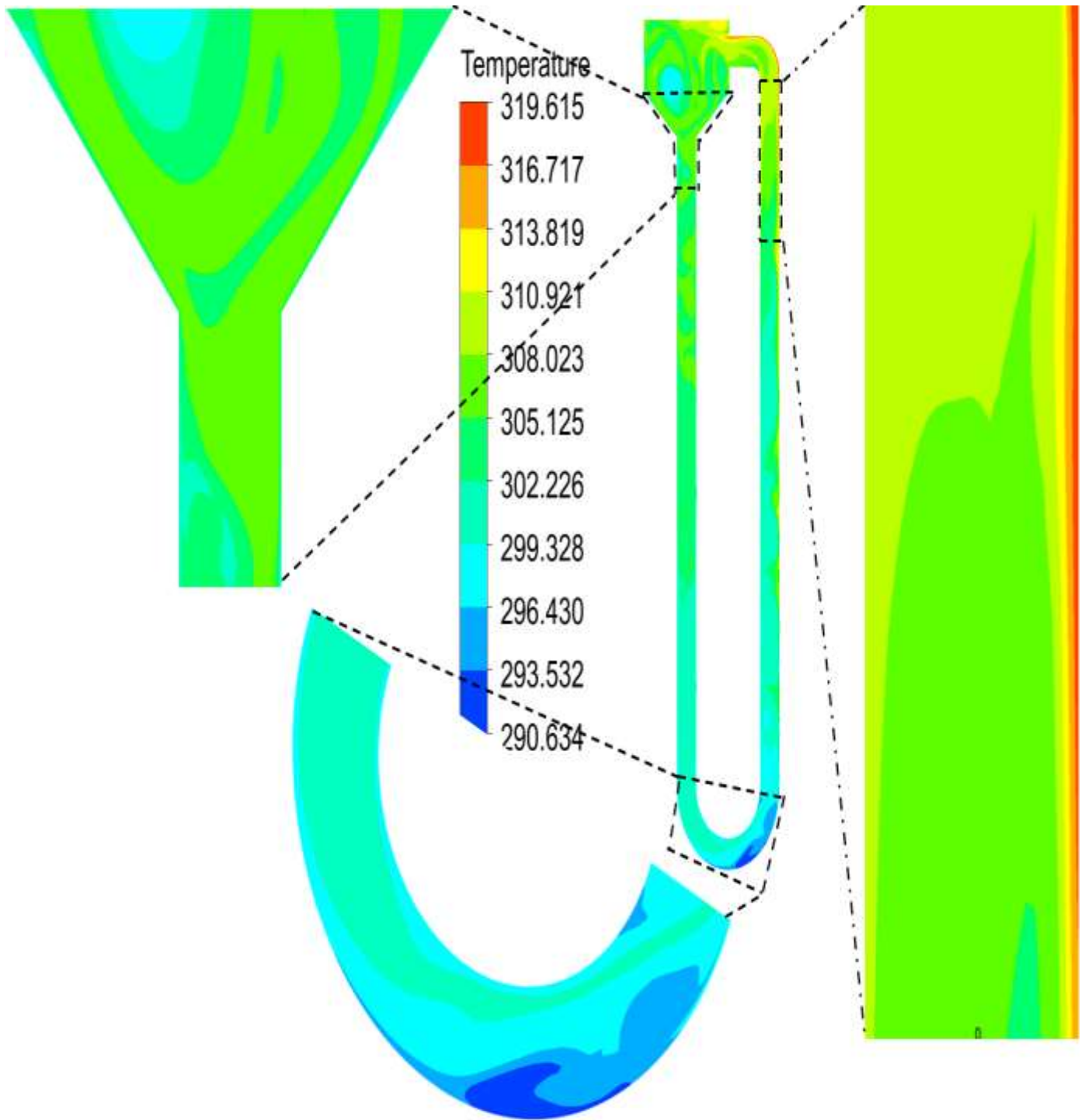


Figure 36: Temperature contours distribution with magnified areas of high temperature gradient within the thermosiphon PBR's CFD simulation

#### 4.2.2 VELOCITY DISTRIBUTION

The CFD predicted velocity distribution of the thermosiphon PBR is discussed here. As well, the CFD simulated velocity distribution was probed at two positions corresponding to the bottom and top riser position used to monitoring the thermosiphon PBR's riser local flow velocity.

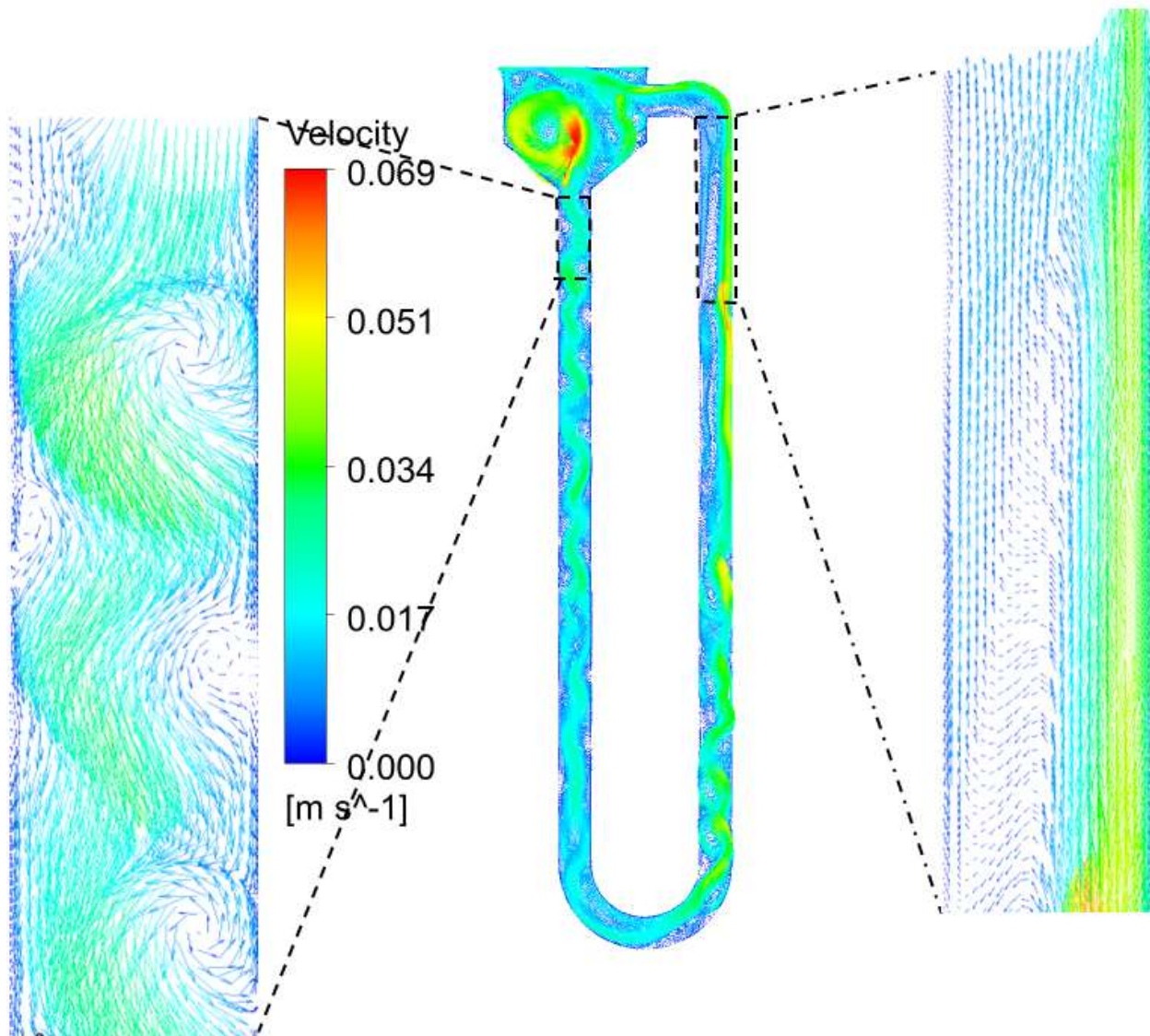


Figure 37: Velocity vectors of the CFD simulations showing the direction of flow due to thermosiphoning

Figure 37 shows the velocity vector distribution of the working fluid within the thermosiphon PBR and it can be seen that the velocity vector distribution varies throughout the domain. However, the velocity vectors indicate an upward movement on the riser section with a

corresponding downward movement on the downcomer section. This indicates the presence of buoyancy driven flow which is highly favored towards the forward direction with little or no flow reversals. These results are a better representation of the reality in the TPBR than those presented in literature (Louisos et al., 2013) which make use of constant uniform wall temperature and surface flux by reporting the bulk fluid motion of a 2D thermosiphon to be a chaotic flow regime and associated with flow reversals. This high degree of forward buoyancy driven flow is presumed to exist as a result of the smooth light transfer through the riser section captured by the UDF radiative transfer equation. The gradual attenuation of this light and subsequent volumetric heat generation guarantees a smooth temperature-induced density gradient which enhances the forward buoyancy flow. At the same time, it eliminates the heat deprived internal core of the absorber/solar collector which brings about flow instabilities in other thermosiphon systems.

The eddies within the downcomer section are seen to be very strong with a serpent-like profile. The defined adiabatic boundary conditions of the downcomer walls prevented heat losses through that section resulting to the almost steady temperature and density of the circulating fluid. However, the effect of gravity was greatest within this section and was interpreted to be responsible for the rapid downward movement of the fluid since it is colder and generally heavier. This was practically impossible to see in experimental setup because the downcomer section of TPBR was thermal insulated with a layer of cotton wool and aluminum foil. However, this revelation provides valuable insights into fluid flow profile within the downcomer section.

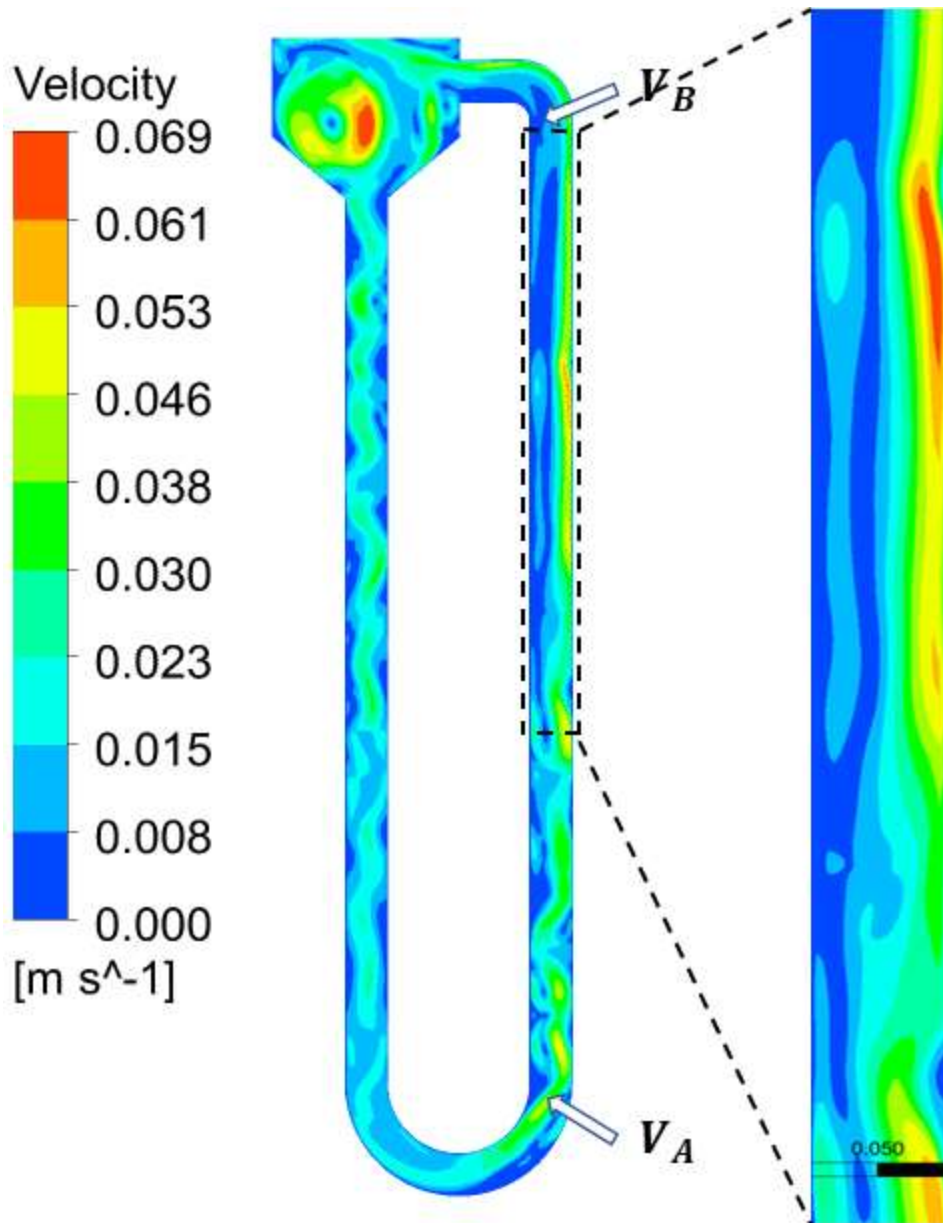


Figure 38: Velocity contours of the CFD simulations showing the two velocity notation points and the riser's flow profile.

Figure 38 shows the velocity contour distribution of the working fluid within the thermosiphon PBR and it can be seen that the velocity of the working fluid varies throughout the domain. This corresponds very well with the natural fluid flow being induced by density gradients which are caused volumetric heating through light absorption and cooling of the working fluid at the riser and cooling section respectively. The fluid flow can be attributed mainly to buoyancy effects,

agreeing with observation in the flow field visualization experiments (see section 4.3 ). Additionally, it can be noted that the fluid flow velocities predicted by CFD simulation remain laminar, at 0.069 m/s. This velocity falls within the range of other flow velocity studies relating to more conventional photobioreactor designs, at 0.038 m/s, 0.11 m/s and 0.36 m/s for wholly, half and alternately aerated airlift PBRs respectively (J. Huang et al., 2016). As well, they were in the range of some experimental thermosiphon solar water heating (SWH) systems of  $3.3 \times 10^{-2}$  m/s (Morrison et al., 2005), 0.8 m/s (Gandhi et al., 2011). The 0.8 m/s of Gandhi (2011) is of a larger order of magnitude but this can be likely explained due to their defined outdoor boundary conditions for sunlight which resulted to large temperature differences driving faster flow.

Another important observation is the riser's fluid flow profile which is more tilted towards the front of the riser section. This was expected since as the incident light intensity which when absorbed by the microbial cells is responsible for volumetric heating and buoyancy flow has an inverse relationship with the penetration depth (riser diameter). Therefore, the incident light intensity drops exponentially from the front to the rear surface of the riser according the famous Beer-Lambert law (Luo & Al-Dahhan, 2004, 2011) thereby producing a buoyancy flow which is more tilted towards the front of the riser section. This CFD predicted flow profile agrees very well with in literature for volumetric solar absorber (Roldán et al., 2014).

Another important observation is the swirly eddied fluid flow in the storage tank section, which corresponds well with experimental observation (see section 4.4.3 ), and was interpreted to occur as a result of rapid heat lost at a small dimension cooling section bringing about rapid density variations. This occurrence is will highly favor the satisfactory passive fluid flow and keep bacterial cells in suspension within the tank section of the TPBR. Also, it would likely result to improving the mass transfer, and eliminating the light and nutrient gradients through enhanced mixing thereby increasing biomass productivity



### 4.3 FLOW VISUALIZATION RESULTS

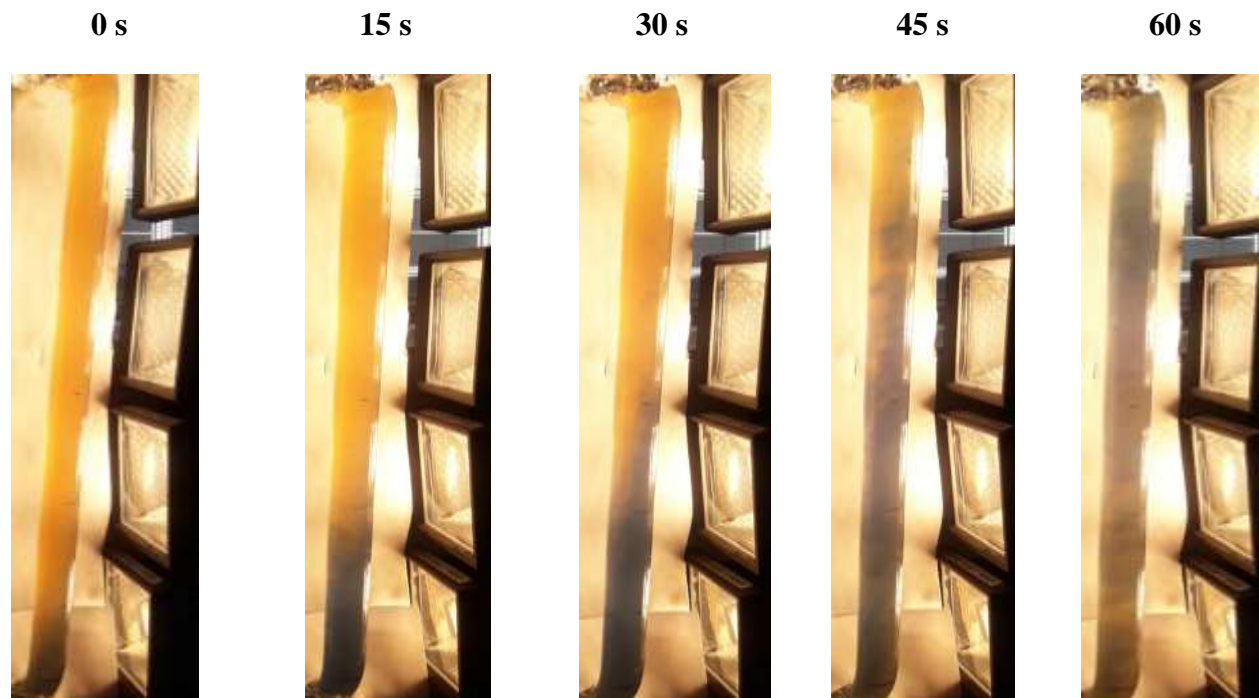
This section contains the results and discussions for the visualization of local circulation patterns generated by the buoyancy flow through the riser section of the thermosiphon PBR. This provides insight into the hydrodynamics of both experimental scenarios: activated and inactivated *Rhodopseudomonas paulustris* cells operating under the same conditions of  $0.5 \text{ kg/m}^3$  of biomass concentration. This experimental fluid dynamic investigation was realized through the nonintrusive technique of ‘image maker method’ (Joshi et al., 2009). As already stated, the underlying principle of this technique is the measurement of the displacement marked by the fluid particles in consecutive images. A small difference of less than 3% was reported when this image maker method under the name “color dye method” was compared with the commonly used acid tracer method with pH meters for the mixing time characterization of a flat panel airlift PBR (Reyna-Velarde et al., 2010). Therefore, the image marker method was reliable for the hydrodynamic characterization of buoyancy driven flow through the riser section of the TPBR. Conversely, the acid tracer method was inappropriate for this study since as the TPBR’s geometry was too constrained for the insertion of a pH meter on the riser section.

The thermosiphon PBR medium content is comprised of a buffered solution, *Rhodopseudomonas palustris* (fresh and dead) which produced a purple color that changes to pale yellow upon addition of the bromothymol blue indicator. This occurrence was expected since the buffer solutions weaken the effect of the *Rhodopseudomonas palustris* media’s pH 7.3 to below 6.0 where the bromothymol blue indicator showed a pale-yellow color. The pale-yellow color was observed to change into blue upon the drop wise addition of a 3.5M NaOH solution from the top septum-sealed port at the cap of the thermosiphon BPR. This pale yellow to blue color change was expected since the presence of NaOH solution brought about a pH shift to some value greater than 7.6 where the bromothymol blue indicator showed a blue color. This color change and dissipation of the thermosiphon PBR medium content was marked by the plug of fluid motion in consecutive images.

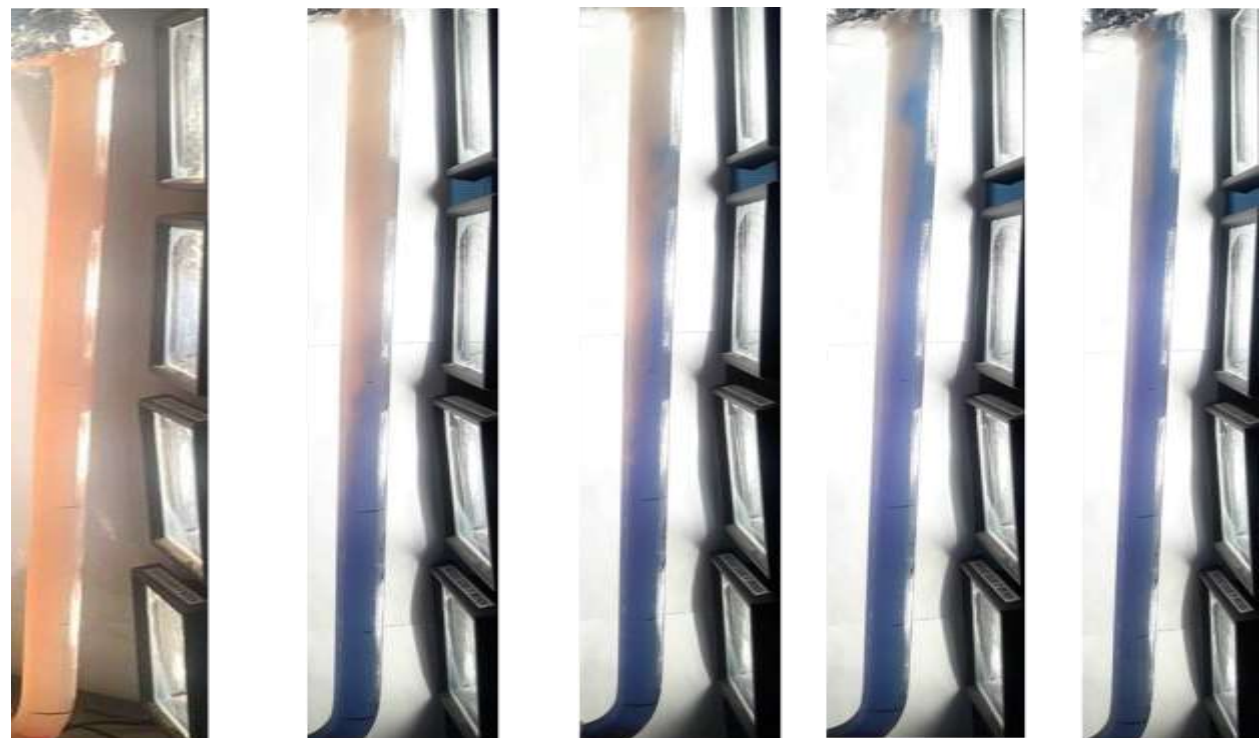
Figure 39 shows snapshots taken at the riser section of the thermosiphon BPR for activated and inactivated bacterial cells operating under the same conditions so that they could be compared. Photographs were taken at intervals of 15s from the time the color change (pink to blue) emerged at the bottom until when it reaches and exit the top of the riser into the storage tank via the up-

riser. Photos on the top side of Figure 39 had inactive bacterial cells while the others at the bottom side had active bacterial cells. The overall and specific color change dissipation rates between the various time intervals in one particular case and that of the same time interval between the two cases (active and inactive experiments) were identified as the main features worth observing in the photographs for comparison. In general, this color change dissipation rates provides insights into the fluid velocity as well as TPBR's mixing which are difficult to evaluate independently.

From 0 to 60 seconds of both cases, it is clearly seen that there is a general upward movement of the flow mixing towards storage tank due to buoyancy effect, strong enough to propagate this color dissipation within its main flow. It is important to note that the color dissipation and turbulence is favoured towards the front than to the rear surface of the riser section, corresponding with the anticipated light absorption and, therefore density, gradient. Furthermore, the flow mixing at the same time intervals of the two cases clearly shows the color dissipation and turbulence rate to be slight better for the active than the inactive bacterial cell experiments. This was expected since the active *Rhodospseudomonas palustris* cells were still undergoing metabolic heat generation with the light absorption meanwhile the inactivation process halted that for the inactive *Rhodospseudomonas palustris* cells. Also, the inactivated *Rhodospseudomonas palustris* cells may have experience morphological cell damages during the inactivation process which might have affected their photosynthetic pigment molecule and light absorbing potentials. It was presumed that this contribution led to an increased stabilization temperature and enhanced the dissipation and turbulence within the riser section of the thermosiphon PBR.



**Inactivated bacterial cells**



**Activated bacterial cells**

Figure 39: Flow visualization photographs of the TPBR at intervals of 15s, operating under  $0.5 \text{ Kg/m}^3$  intervals under for active and inactive bacterial cells with pink to blue color dissipation showing indicating fluid flow through the riser

#### 4.4 VALIDATION: COMPARISON BETWEEN EXPERIMENTS RESULTS AND CFD SIMULATIONS

This section contains the results and discussion for the validation of the CFD model via experiments. As already stated, this validation will provide some credibility to the model results and the temperature, velocity, and fluid flow profile were the parameters identified for validation purposes. These model parameters were validated via (i) quantitatively through the measurements of three center-pipe temperatures on the thermosiphon PBR and two points local flow velocity at on the riser's buoyancy flow field, and (ii) qualitatively through flow profile visualization on riser section of the thermosiphon PBR. Since the experimental results of the active *Rhodospseudomonas palustris* were generally better than those of the inactive bacterial cells, their results were used to validate the numerical CFD simulation results in this section using (equation (42)). More to that, the actual thermosiphon PBR will be operated with active bacterial cells absorbing light for photosynthesis while continuously converting substrates to products like biohydrogen

$$\% \text{ Deviation} = \frac{|\text{Experimental data} - \text{CFD predicted data}|}{\text{Experimental data}} \times 100 \quad (42)$$

##### 4.4.1 TEMPERATURE VALIDATION RESULTS

The experimental temperature readings of three center-pipe locations ( $T_1, T_2, \text{ and } T_3$ ) were measured and compared to the CFD predicted temperatures as presented in Table 13. The CFD simulations results were able to predict the thermosiphon PBR's thermal performance for all three points with a relatively small difference of less than 5% as observed. In addition to the experimental measurement error, the thermal radiation, heat transfer coefficients and buoyancy fluid flow influences the temperature value obtained. More to that, the numerical simulation was a 2D model, and the radiation heat transfer and extinction coefficient by *Rhodospseudomonas palustris* for attenuating light have been included in the UDF volumetric heat source. These conditions have been reported to bring about some deviations of less than 5% for volumetric solar absorber (Roldán et al., 2014). However, the reported deviation of this study is still significantly lower than that reported in literature for thermosiphon heat pipes and natural convection industrial oven with 10.78% (Fadhl et al., 2013) and 15% (Rek et al., 2012)

respectively. However, smaller deviation of less than 3% have been reported for volumetric absorber solar absorber (Roldán et al., 2014). This shows that the 2D CFD simulation results are in appreciable agreement with the experimental results. Generally, the CFD simulations under predicted the TPBR's thermal performance. This was a result of the model not accounting for the radiation concentration of 4 halogen lamps as well as their spectral emissivity factors. This limitation could be improved by making use of a pyrometer to experimentally determine the radiation amplification while accounting for the emissivity at every glass interface.

Table 13: Comparison of measured and CFD simulated temperatures

Measuring point	Experiment (K)	CFD simulation (K)	Deviation (%)
$T_1$	$317.7 \pm 0.5$	307.9	3.1
$T_2$	$313.8 \pm 0.6$	305.5	2.7
$T_3$	$312.6 \pm 2$	299.5	4.2

#### 4.4.2 VELOCITY VALIDATION RESULTS

The local flow velocities at two center-pipe points (bottom and top) of the riser section were used to quantitatively compare the CFD simulation results as presented in Table 14. Note that, the experimental local flow velocity was unmeasured at the starting point (bottom riser) since it is the first point of distance-time velocity measurement. The time taken for the color change and dissipation rate to travel the riser distance to the top point (end point) was measured and recorded as  $V_2$ . The local flow velocities between these two points were then compared to the probed CFD simulation results at the same points which were generally less than 10%. Nevertheless, these results are still acceptable although there is certainly room for improvement through the use of more sophisticated non-invasive fluid flow measurement techniques like the high resolution digital Particle image Velocimetry (PIV)(Gandhi et al., 2011; Joshi et al., 2009; Morrison et al., 2005)

Table 14: Comparison of measured and CFD simulated velocities

Measuring point	$V_1$	$V_2$
Experiment (m/s)	unmeasured	$0.0093 \pm 0.0004$
CFD simulation (m/s)	0.0161	0.0085
Overall deviation (%)		9.2

#### 4.4.3 FLUID FLOW PROFILE VALIDATION RESULTS

Photographs of the local fluid flow profile at 45s and 60s intervals passing through the riser section were assumed fully developed and therefore used to qualitatively compare the CFD simulation results as illustrated in Figure 40. It is clear that this 2D CFD simulation agrees with experimental data by revealing a fluid flow profile which is more tilted towards the front of the riser section. This is in agreement with literature analysis of light penetration through organisms since the density gradient is strongly dependent on the temperature rise, which is itself a function of light absorption, which drops exponentially from the front to the rear surface of the riser.

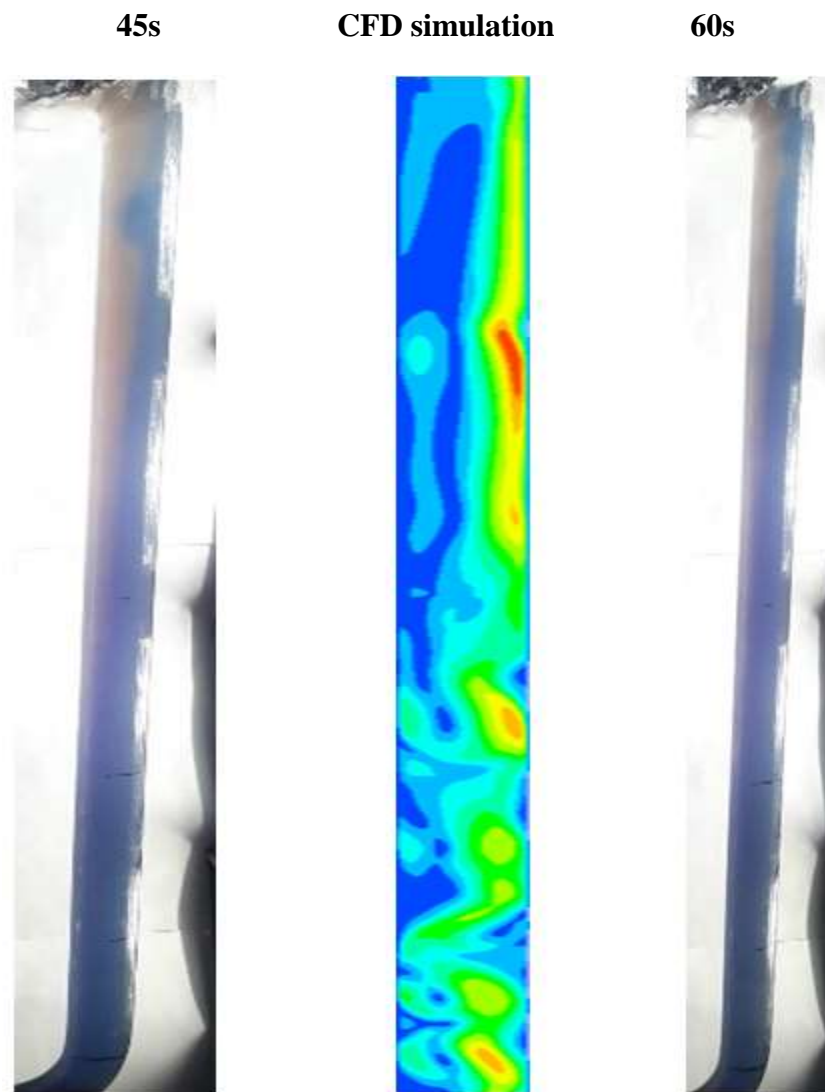


Figure 40: Flow visualization photographs of 45s and 60s compared with CFD simulation results

Also, photographing the thermosiphon PBR's storage tank and cooling tank section shows a swirling and serpentine fluid flow which enhances the mixing intensity around those areas. This was not expected but however matches well with the numerical simulation Figure 41. This was interpreted to occur as a result of rapid heat lost at a small dimension cooling section bringing about rapid density variations, combine to the gravitational pull of the working fluid which enhances its circulation velocity while propagating through the downcomer. This implies that the thermosiphon PBR's mixing speed is highest at the storage tank section and induces the bacterial cells to freely circulate from the illuminated surface to the dark center. This would likely result to improving the mass transfer, and eliminating the light and nutrient gradients through enhanced mixing thereby increasing biomass productivity.

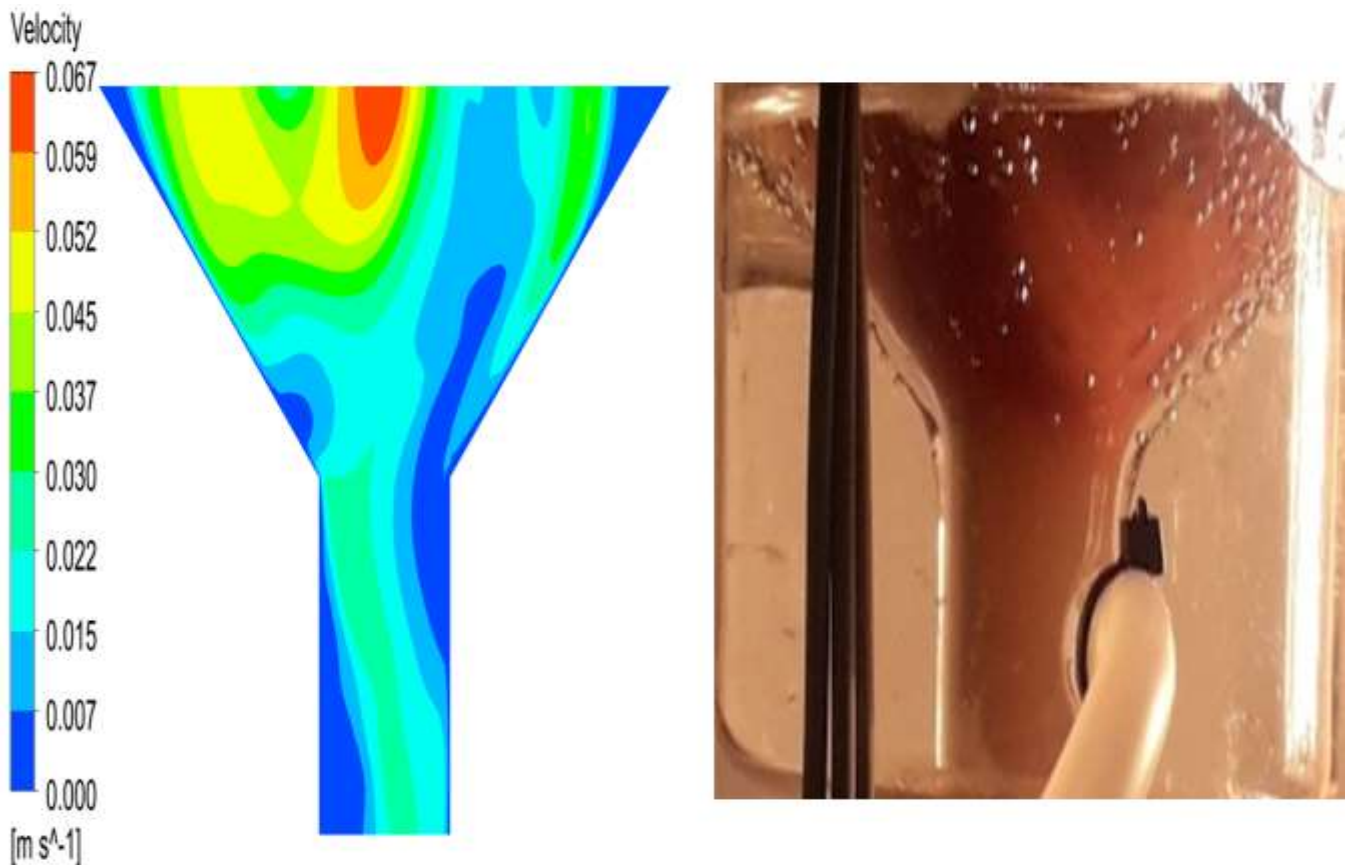


Figure 41: Flow visualization photograph of the storage and mixing tank sections compared with CFD simulation results

#### 4.5 EFFECT OF LIGHT ABSORPTION ON HEATING RATE

This section presents the results and discussion of microbial light absorption and its effects on the heating of the thermosiphon PBR. It provides insight into the metabolic heat contributions the thermosiphon PBR operating efficiency. Since the thermosiphon BPR is unable to absorb light before the system starts-up, evaluating its startup to steady state behavior is a critical variable for evaluating the reliability and efficiency of the thermosiphon PBR. Theoretically, the thermosiphon BPR's efficiency will be low if it requires a long starting to steady state time or if it is unable to attain steady state (C. Huang et al., 2017). For both systems, the thermosiphon BPR's startup proceeds through an increase of the sensible heat as a result of bacterial light absorption, and subsequent temperature change that was monitored at three different center-pipe locations by thermocouples probes. The arithmetic mean was calculated and examine over the duration of the experiments followed by the numerical estimation of the rate of heating from light absorption as illustrated in Figure 42.

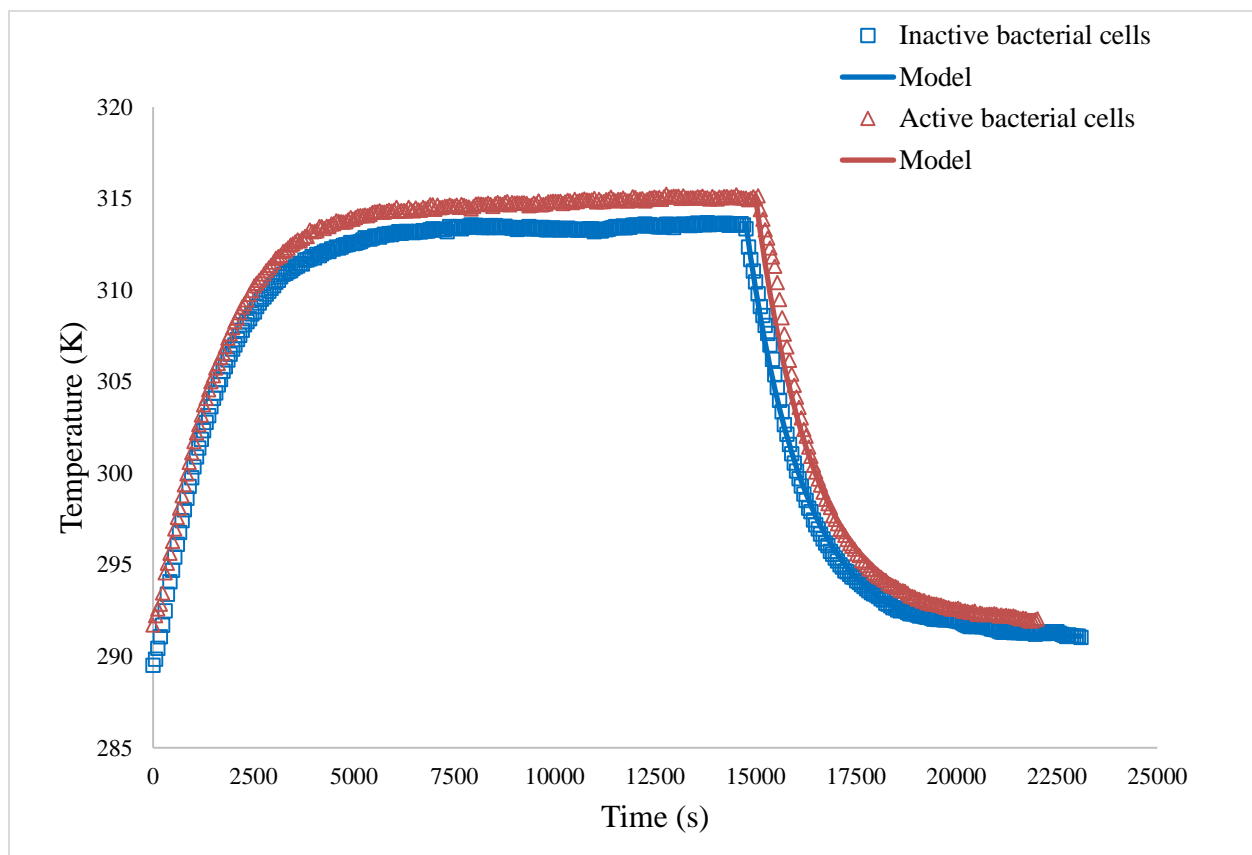


Figure 42: Heating rate: startup to steady temperature-time profile for active and inactive bacterial cells within the thermosiphon PBR and under the same operating conditions.



The startup behavior of the thermosiphon BPR operating with active and inactive bacterial cells were approximately the same by reaching a steady state time of around 5000s. However, their resulting steady state characteristics were slightly different with the highest and lowest steady temperatures of 315.06k and 313.56k attained by the active and inactive bacteria cells respectively. This was expected since as the inactivated bacterial cells could only absorb light due to their purple color pigmentation which accounted for temperature being lower than that of the activate *Rhodopseudomonas palustris* bacterial cells which were able to absorb and generate metabolic heat. Also, the computed heat gain followed the same trend with the highest and lowest being 68.69 J/s and 63.65 J/s for the active and inactive bacteria cells respectively. As a result, there was a 3.7% increase in the steady temperature corresponding to 7.9% increase in heating rate for active and inactive bacterial cells as we earlier hypothesize and this difference was attributed to the metabolic heat generation and fluoresce waste heat for the active bacterial cells as well some morphological damages in the cell structures during the inactivation of the bacterial cells. This is mainly because almost all the photons were assumed to be absorbed by *Rhodopseudomonas palustris* cells and very little light energy is absorbed by the medium because every other parameter (incident radiant illumination, and cooling water flow rate) was relatively constant for both experiments.

Another important observation is that the steady state (315.06K and 313.56K) as well as startup (around 29.15K ) temperatures of both cases were of suitable ranges for the cultivation of a wide variety of microbial species including microalgae, cyanobacteria and purple non-sulphur bacteria (Argun & Kargi, 2010; Pires et al., 2017; D Zhang et al., 2015) like *Rhodopseudomonas palustris* which is here investigated. However, the thermosiphon PBR's steady temperatures could even be altered to estimated temperatures of 303.08k where other photosynthetic microbial species have been reported to growth favorably just by increasing the flowrate of the circulating subcooled water.

#### 4.6 EFFECT LIGHT ABSORPTION ON THERMOSIPHONING CELLS

This section presents the results and discussion of microbial light absorption and its effects thermosiphoning cells within the thermosiphon PBR. It provides insights into the bacterial cell circulation and free suspension within the thermosiphon PBR as illustrated in Figure 43. Starting the experiment with an initial biomass concentration of  $0.5\text{kg}/\text{m}^3$  for both the active and inactive bacterial cells, the circulating cells in free suspension decreased by 14.2%, and 16.9% corresponding to approximately 86% and 83% of freely circulating bacterial cells within the first 1 hour of operation respectively. Thus, the generated fluid flow from thermosiphoning within the thermosiphon PBR was not sufficiently strong to keep all the biomass in free suspension. However, there was generally a 3% increase of active bacterial cells in free suspension which was maintained throughout the steady state conditions. This was not entirely the case for the inactive bacterial cells as the damage of the cell morphological structure during the inactivation process partially contributed to a further 4.8% in the free suspension circulating cells after 3 hours of operation. Most importantly, the results reveals that a higher stabilization temperature of the thermosiphon PBR leads to an increased thermosiphoning and faster flow rates, which would likely result in enhanced cell circulation, however, bacterial cultures are limited to physiological temperatures. Nonetheless, the thermosiphon PBR did demonstrate the continual and passive circulation of a significant majority of bacterial biomass within the reactor.

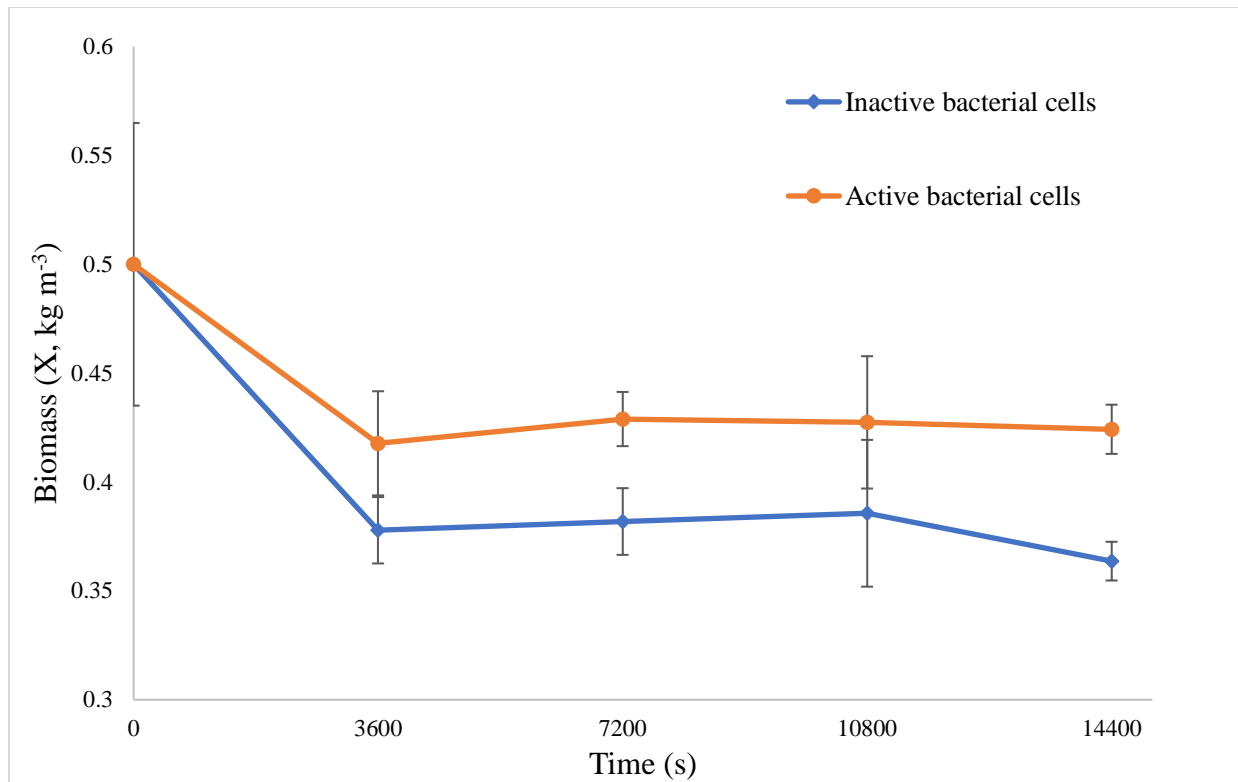


Figure 43: Biomass circulation rate for active and inactive *Rhodospseudomonas palustris* bacterial cells with the error bars representing the standard deviations of three repeats.

## CHAPTER FIVE

### CONCLUSIONS AND RECOMMENDATIONS

#### 5.1 CONCLUSIONS

The main aim of this research was to use CFD modeling and experiments to support the development of a thermosiphon photobioreactor, where fluid circulation is achieved by temperature difference arising from light absorption. The goal of the larger project, of which this work forms a part, is to apply the thermosiphon PBR for waste-water treatment by a candidate photosynthetic bacterium like *Rhodospseudomonas palustris* which is extremely metabolically diverse, and able to consume a large variety of potentially recalcitrant wastewater components, while simultaneously producing high purity hydrogen.

This aim was achieved by addressing five key objectives: (i) the development of photobioreactor geometry based on the passive thermosiphon fluid flow and construct it for testing, (ii) the numerical modeling of passive fluid flows within the reactor geometry using ANSYS-workbench version 17.2, (iii) the qualitative and quantitative validation of the Thermosiphon PBR design by comparing how closely the experimental model corresponds to the CFD model, and (iv) the investigation of microbial light absorption, and corresponding heat transfer rates within the Thermosiphon PBR. Overall, the thesis main aim and objectives were successfully accomplished with the following conclusions arrived at.

The 1-L working volume thermosiphon PBR was designed by structurally adapting the original thermosiphon loop published by Close (1962), sized with a single parameter optimization for the riser's diameter, constructed with glass and other hydrogen impermeable auxiliary units thereby meeting up with the design criteria for photosynthetic microorganism cultivation and subsequent hydrogen production.

The thermosiphon PBR's CFD model made use of the boussinesq approximation as well as experimental and theoretical obtained heat transfer coefficients for buoyancy driven convection, a User-Defined Function (UDF) for radiative transport equation which incorporates experimentally obtained spectral irradiance and attenuation parameters of active *Rhodospseudomonas palustris*. The UDF captured the non-uniform volumetric sensible heating from light absorption, primarily mediated by microbial cells in the reactor. The CFD simulation

flow patterns clearly showed buoyancy driven characteristic flow profiles. Specifically, the settling tank showed strong eddies, while flow velocities tilted to the front in the riser section.

The reliability of the CFD simulations were ascertained through validation experiments with active *Rhodospseudomonas palustris* for thermal performance, local fluid flow and local flow velocity profiles measurements. Quantitatively, the experimental and CFD predicted temperature and local fluid flow velocities measurements at the tested points were to less than 5% and 10% respectively. Also, the flow visualization on the riser section of the thermosiphon BPR also found that light absorption significantly influences fluid flow circulation and mixing which lead to a satisfactory agreement between the experimental observations and the CFD simulations results from a qualitative view point.

The experiments with active and inactive *Rhodospseudomonas palustris* were used to quantitatively estimate the contributions of the bacterial metabolic heat generation and waste fluorescence heat to the overall thermal effect. The results revealed the bacterial metabolic heat generation and waste fluoresce heat to bring about a 4% and 8% increase in the steady state temperatures and heating rate respectively. However, the influence of the medium absorbance was assumed very little thereby putting in some uncertainties around the morphological cell structure damages during the inactivation of the bacterial cells. Also, the attained steady temperatures were of suitable ranges for the cultivation of a wide variety of microbial species including microalgae, cyanobacteria and purple non-sulphur bacteria.

The thermosiphoning effect arising from the bacterial metabolic heat generation and waste fluorescence heat was also investigated and it contributed to keeping a vast majority of bacterial cells in free suspension. In general, the thermosiphon PBR provided satisfactory fluid flow to keep bacterial cells in suspension, maintaining up to 88% of the bacterial loading in free suspension. However, its generated fluid flow from thermosiphoning was not sufficiently strong to keep all the biomass in free suspension. Never the less, the increased stabilization temperature resulted to an increased thermosiphoning and faster flow rates, which brought about the enhanced free suspension of bacterial cells during circulation.

## 5.2 RECOMMENDATIONS

The developed TPBR has been demonstrated both numerically and experimentally to provide satisfactory passive fluid flow, keeping up to 88% of the bacterial loading in free suspension. This was mainly based on the temperature-induced density difference resulting from continuous non-uniform sensible heating due to microbial light absorption and subsequent heat removal through forced convection of the circulating water on the riser and cooling section respectively. This is a significant development within this research area; however, further investigations as recommended below are required to advance the established thermosiphon driven Photobioreactor:

1. The qualitative CFD model validation with image marker method has been performed in this work; however, further validation making use of advanced non-invasive fluid flow measurement techniques like high resolution digital Particle image Velocimetry (PIV) would improve confidence in the model results. In addition, it would not only improve the experimental accuracy of the local fluid flow velocity measurements but also allow for three-dimensional flow pattern investigations and dead zone characterization with the computational fluid dynamic model.
2. The present work has established the CFD model technique for the thermosiphon photobioreactor with a simplified 2D model. This approach minimizes computational expensive while accurately simulating the passive fluid flow and heat transfer. Nonetheless, this work could be further extended to a 3D model to compare with the present 2D model for fluid flow reversal, instabilities and dead zones which has been reported in other thermosiphon related systems.
3. The current work makes use of the emission spectrum of halogen lamps as graybody solar simulators at a color temperature of 2900k but did not investigated the radiation amplification and concentration factor of using four halogen lamps. The influence of the radiation distribution and concentration on the riser section of thermosiphon PBR should be further examined with a pyrometer while accounting for the emissivity at every glass interface.

4. Although with the very small illumination distance (less than 50mm) between the lamp surfaces and the riser section of thermosiphon PBR, yet the influence of thermal convection on the passive fluid flow has been identified as negligible compared to the radiative transfer effect of the lamps, a study of its influence on the overall thermosiphoning will provide a complete confidence of the assumption, and affirm its influence on the passive fluid flow and free suspension of bacterial cells.
5. The User-Defined Function (UDF) for radiative transport equation used in this work is a modified form of the Beer-Lambert law and is only valid for biomass concentration less than  $1\text{Kg}/\text{m}^3$  meanwhile *Rhodospseudomonas palustris* can grow up to  $> 2\text{Kg}/\text{m}^3$  for an optically dense culture. Therefore, further modification of the UDF with the two-flux approximation is essential for simulating experimental scenario with anticipated biomass concentration greater than  $1\text{Kg}/\text{m}^3$ .
6. The true value of such a CFD model can be exploited by performing parametric and sensitivity analysis on factors which have a significant impact on the design and operation of the physical thermosiphon photobioreactor like the investigation of different material thickness and types at the various thermosiphon PBR's sections, geometric modification, heat and light transfer values, which will suit different climatic conditions for outdoor application should be considered for further modeling.
7. Finally, cultivating photosynthetic bacteria like *Rhodospseudomonas palustris* in this Thermosiphon PBR for subsequent hydrogen production is essential for data on hydrogen bubble production and its light scattering effects to be incorporated in a three phase CFD model

## REFERENCES

- Acién, F. G., Garcia Camacho, F., Sanchez Perez, J. A., Fernandez Sevilla, J. M., Molina Grima, E., Fernández, F. G. A., ... Grima, E. M. (1998). Modeling of Biomass Productivity in Tubular Photobioreactors for Microalgal Cultures: Effects of Dilution Rate, Tube Diameter, and Solar Irradiance. *Biotechnology and Bioengineering*, 58, 605–616.
- Acién Fernández, F. G., Fernández Sevilla, J. M., & Molina Grima, E. (2013). Photobioreactors for the production of microalgae. *Reviews in Environmental Science and Biotechnology*, 12(2), 131–151. <https://doi.org/10.1007/s11157-012-9307-6>
- Acién Fernández, F. G., García Camacho, F., & Chisti, Y. (1999). Photobioreactors: light regime, mass transfer, and scaleup. *Progress in Industrial Microbiology*, 35(C), 231–247. [https://doi.org/10.1016/S0079-6352\(99\)80118-0](https://doi.org/10.1016/S0079-6352(99)80118-0)
- Akkerman, I., Janssen, M., Rocha, J., & Wijffels, R. H. (2002). Photobiological hydrogen production: Photochemical efficiency and bioreactor design. In *International Journal of Hydrogen Energy* (Vol. 27, pp. 1195–1208). [https://doi.org/10.1016/S0360-3199\(02\)00071-X](https://doi.org/10.1016/S0360-3199(02)00071-X)
- Alizadehdakhel, A., Rahimi, M., & Alsairafi, A. A. (2010). CFD modeling of flow and heat transfer in a thermosyphon. *International Communications in Heat and Mass Transfer*, 37(3), 312–318. <https://doi.org/10.1016/j.icheatmasstransfer.2009.09.002>
- Anderson, G. (2003). Study of Light as a parameter in the growth of algae in a Photo-Bioreactor ( PBR ) This page is for on-line indexing purposes and should not be included in your printed version . *An ASAE Annual International Meeting*, (July 2003), 1–23. Retrieved from [https://www.researchgate.net/publication/280720969\\_Study\\_of\\_Light\\_as\\_a\\_parameter\\_in\\_the\\_growth\\_of\\_algae\\_in\\_a\\_Photo-Bioreactor\\_PBR/citations](https://www.researchgate.net/publication/280720969_Study_of_Light_as_a_parameter_in_the_growth_of_algae_in_a_Photo-Bioreactor_PBR/citations)
- Anderson, G. (2015). Study of Light as a parameter in the growth of algae in a Photo-Bioreactor ( PBR ). Retrieved from [https://www.researchgate.net/publication/280720969\\_Study\\_of\\_Light\\_as\\_a\\_parameter\\_in\\_the\\_growth\\_of\\_algae\\_in\\_a\\_Photo-Bioreactor\\_PBR/citations](https://www.researchgate.net/publication/280720969_Study_of_Light_as_a_parameter_in_the_growth_of_algae_in_a_Photo-Bioreactor_PBR/citations)



- Ansys Fluent. (2016). Module 08 : Heat Transfer. ANSYS Inc.
- ANSYS Fluent. (2016). Module 01 : Overview of the CFD Process. In *Module 01 : Overview of the CFD Process, Release 17.0*. ANSYS Inc.
- Argun, H., & Kargi, F. (2010). Photo-fermentative hydrogen gas production from dark fermentation effluent of ground wheat solution: Effects of light source and light intensity. *International Journal of Hydrogen Energy*, 35(4), 1595–1603. <https://doi.org/10.1016/j.ijhydene.2009.12.040>
- Asfia, F. J., & Dhir, V. K. (1996). An experimental study of natural convection in a volumetrically heated spherical pool bounded on top with a rigid wall. *Nuclear Engineering and Design*, 163(3), 333–348. [https://doi.org/10.1016/0029-5493\(96\)01215-0](https://doi.org/10.1016/0029-5493(96)01215-0)
- Bangert, K. (2013). *Photo-Bioreactor Modelling And Development Of Methods For The Optimisation Of Micro-algal Biodiesel Production*. The University of Sheffield.
- Basak, N., & Das, D. (2007). The prospect of purple non-sulfur (PNS) photosynthetic bacteria for hydrogen production: The present state of the art. *World Journal of Microbiology and Biotechnology*, 23(1), 31–42. <https://doi.org/10.1007/s11274-006-9190-9>
- Basak, N., Jana, A. K., & Das, D. (2016). CFD modeling of hydrodynamics and optimization of photofermentative hydrogen production by *Rhodospseudomonas palustris* DSM 123 in annular photobioreactor. *International Journal of Hydrogen Energy*, 41(18), 7301–7317. <https://doi.org/10.1016/j.ijhydene.2016.02.126>
- Başaran, T., & Küçüka, S. (2003). Flow through a rectangular thermosyphon at specified wall temperatures. *International Communications in Heat and Mass Transfer*, 30(7), 1027–1039. [https://doi.org/10.1016/S0735-1933\(03\)00161-1](https://doi.org/10.1016/S0735-1933(03)00161-1)
- Benson, B. C., & Rusch, K. A. (2006). Investigation of the light dynamics and their impact on algal growth rate in a hydraulically integrated serial turbidostat algal reactor (HISTAR). *Aquacultural Engineering*, 35(2), 122–134. <https://doi.org/10.1016/j.aquaeng.2005.09.005>
- Berberoglu, H., Gomez, P. S., & Pilon, L. (2009). Radiation characteristics of *Botryococcus braunii*, *Chlorococcum littorale*, and *Chlorella* sp. used for CO<sub>2</sub> fixation and biofuel

- production. *Journal of Quantitative Spectroscopy and Radiative Transfer*, 110(17), 1879–1893. <https://doi.org/10.1016/j.jqsrt.2009.04.005>
- Berberoglu, H., & Pilon, L. (2007). Experimental measurements of the radiation characteristics of *Anabaena variabilis* ATCC 29413-U and *Rhodobacter sphaeroides* ATCC 49419. *International Journal of Hydrogen Energy*, 32(18), 4772–4785. <https://doi.org/10.1016/j.ijhydene.2007.08.018>
- Berberoglu, H., Yin, J., & Pilon, L. (2007). Light transfer in bubble sparged photobioreactors for H<sub>2</sub> production and CO<sub>2</sub> mitigation. *International Journal of Hydrogen Energy*, 32(13), 2273–2285. <https://doi.org/10.1016/j.ijhydene.2007.02.018>
- Bitog, J. P., Lee, I. B., Lee, C. G., Kim, K. S., Hwang, H. S., Hong, S. W., ... Mostafa, E. (2011). Application of computational fluid dynamics for modeling and designing photobioreactors for microalgae production: A review. *Computers and Electronics in Agriculture*, 76(2), 131–147. <https://doi.org/10.1016/j.compag.2011.01.015>
- Budihardjo, I., Morrison, G. L., & Behnia, M. (2007). Natural circulation flow through water-in-glass evacuated tube solar collectors. *Solar Energy*, 81(12), 1460–1472. <https://doi.org/10.1016/j.solener.2007.03.002>
- Carvalho, A. P., Silva, S. O., Baptista, J. M., & Malcata, F. X. (2011). Light requirements in microalgal photobioreactors: An overview of biophotonic aspects. *Applied Microbiology and Biotechnology*. <https://doi.org/10.1007/s00253-010-3047-8>
- Cengel, Y. A., & Ghajar, A. J. (2011). *Heat and Mass Transfer: Fundamentals and Applications*.
- Chisti, Y. (2008). Biodiesel from microalgae beats bioethanol. *Trends in Biotechnology*, 26(3), 126–131. <https://doi.org/10.1016/j.tibtech.2007.12.002>
- Clarke, K. G. (2013). *Bioprocess Engineering: An introductory Engineering and Life Science Approach [Hardcover]*. Woodhead Publishing. <https://doi.org/10.1533/9781782421689.147>
- Close, D. J. (1962). The performance of solar water heaters with natural circulation. *Solar Energy*, 6(1), 33–40. [https://doi.org/10.1016/0038-092X\(62\)90096-8](https://doi.org/10.1016/0038-092X(62)90096-8)

- Cornet, J. F., Dussap, C. G., Gros, J. B., Binois, C., & Lasseur, C. (1995). A simplified monodimensional approach for modeling coupling between radiant light transfer and growth kinetics in photobioreactors. *Chemical Engineering Science*, *50*(9), 1489–1500. [https://doi.org/10.1016/0009-2509\(95\)00022-W](https://doi.org/10.1016/0009-2509(95)00022-W)
- Cui, Z., & Fan, L. S. (2004). Turbulence energy distributions in bubbling gas-liquid and gas-liquid-solid flow systems. *Chemical Engineering Science*, *59*(8–9), 1755–1766. <https://doi.org/10.1016/j.ces.2004.01.031>
- Deo, D., Ozgur, E., Eroglu, I., Gunduz, U., & Yucel, M. (2012a). Photofermentative Hydrogen Production in Outdoor Conditions. *Hydrogen Energy - Challenges and Perspectives*, (October 2012). <https://doi.org/10.5772/50390>
- Deo, D., Ozgur, E., Eroglu, I., Gunduz, U., & Yucel, M. (2012b). Photofermentative Hydrogen Production in Outdoor Conditions. In *Hydrogen Energy - Challenges and Perspectives*. <https://doi.org/10.5772/50390>
- Dwi, A., & Reksodipuro, P. (2009). *Molecular Genetic Studies on the Light Harvesting – Reaction Centre ( LH-RC ) Genes in the Purple Non-Sulphur Bacterium Blastochloris viridis*. University of Glasgow.
- Fadhl, B., Wrobel, L. C., & Jouhara, H. (2013). Numerical modelling of the temperature distribution in a two-phase closed thermosyphon. *Applied Thermal Engineering*, *60*(1–2), 122–131. <https://doi.org/10.1016/j.applthermaleng.2013.06.044>
- Fernandes, B. D., Dragone, G. M., Teixeira, J. A., & Vicente, A. A. (2010). Light regime characterization in an airlift photobioreactor for production of microalgae with high starch content. *Applied Biochemistry and Biotechnology*, *161*(1–8), 218–226. <https://doi.org/10.1007/s12010-009-8783-9>
- Freegah, B., Asim, T., & Mishra, R. (2013). Computational Fluid Dynamics based Analysis of a Closed Thermo-Siphon Hot Water Solar System. *26th International Congress of Condition Monitoring and Diagnostic Engineering Management*.
- Fu, L., Leutz, R., & Ries, H. (2006). Physical modeling of filament light sources. *Journal of*

- Applied Physics*, 100(10). <https://doi.org/10.1063/1.2364669>
- Gandhi, M. S., Sathe, M. J., Joshi, J. B., & Vijayan, P. K. (2011). Two phase natural convection: CFD simulations and PIV measurement. *Chemical Engineering Science*, 66(14), 3152–3171. <https://doi.org/10.1016/j.ces.2011.02.060>
- Gilbert, J. J., Ray, S., & Das, D. (2011). Hydrogen production using *Rhodobacter sphaeroides* (O.U. 001) in a flat panel rocking photobioreactor. *International Journal of Hydrogen Energy*, 36(5), 3434–3441. <https://doi.org/10.1016/j.ijhydene.2010.12.012>
- Gómez-Pérez, C. A., Espinosa, J., Montenegro Ruiz, L. C., & van Boxtel, A. J. B. (2015). CFD simulation for reduced energy costs in tubular photobioreactors using wall turbulence promoters. *Algal Research*, 12, 1–9. <https://doi.org/10.1016/j.algal.2015.07.011>
- Gupta, P. L., Lee, S. M., & Choi, H. J. (2015a). A mini review: photobioreactors for large scale algal cultivation. *World Journal of Microbiology and Biotechnology*, 31(9), 1409–1417. <https://doi.org/10.1007/s11274-015-1892-4>
- Gupta, P. L., Lee, S. M., & Choi, H. J. (2015b). A mini review: photobioreactors for large scale algal cultivation. *World Journal of Microbiology and Biotechnology*, 31(9), 1409–1417. <https://doi.org/10.1007/s11274-015-1892-4>
- Hallenbeck, P. C., & Benemann, J. R. (2002). Biological hydrogen production; Fundamentals and limiting processes. *International Journal of Hydrogen Energy*, 27(11–12), 1185–1193. [https://doi.org/10.1016/S0360-3199\(02\)00131-3](https://doi.org/10.1016/S0360-3199(02)00131-3)
- Huang, C., Lin, W. K., & Wang, S. R. (2017). Two-Phase Closed-Loop Thermosyphon Solar Water Heater with Porous Wick Structure: Performance and Start-Up Time. *Arabian Journal for Science and Engineering*, 42(11), 4885–4894. <https://doi.org/10.1007/s13369-017-2660-6>
- Huang, J., Feng, F., Wan, M., Ying, J., Li, Y., Qu, X., ... Li, W. (2015). Improving performance of flat-plate photobioreactors by installation of novel internal mixers optimized with computational fluid dynamics. *Bioresource Technology*, 182, 151–159. <https://doi.org/10.1016/j.biortech.2015.01.067>

- Huang, J., Ying, J., Fan, F., Yang, Q., Wang, J., & Li, Y. (2016). Bioresource Technology Development of a novel multi-column airlift photobioreactor with easy scalability by means of computational fluid dynamics simulations and experiments. *Bioresource Technology*, 222, 399–407. <https://doi.org/10.1016/j.biortech.2016.09.109>
- Jacobi, A., Steinweg, C., Sastre, R. R., & Posten, C. (2012). Advanced photobioreactor LED illumination system: Scale-down approach to study microalgal growth kinetics. *Engineering in Life Sciences*, 12(6), 621–630. <https://doi.org/10.1002/elsc.201200004>
- Janssen, M., Tramper, J., Mur, L. R., & Wijffels, R. H. (2003). Enclosed outdoor photobioreactors: Light regime, photosynthetic efficiency, scale-up, and future prospects. *Biotechnology and Bioengineering*, 81(2), 193–210. <https://doi.org/10.1002/bit.10468>
- Ji, C. F., Legrand, J., Pruvost, J., Chen, Z. A., & Zhang, W. (2010). Characterization of hydrogen production by *Platymonas Subcordiformis* in torus photobioreactor. In *International Journal of Hydrogen Energy* (Vol. 35, pp. 7200–7205). <https://doi.org/10.1016/j.ijhydene.2010.02.085>
- Joshi, J. B., Tabib, M. V, Deshpande, S. S., & Mathpati, C. S. (2009). Dynamics of Flow Structures and Transport Phenomena, 1. Experimental and Numerical Techniques for Identification and Energy Content of Flow Structures. *Industrial & Engineering Chemistry Research*, 48(17), 8244–8284. <https://doi.org/10.1021/ie8012506>
- Jouanneau, Y., Wong, B., & Vignais, P. M. (1985). Stimulation by light of nitrogenase synthesis in cells of *Rhodospseudomonas capsulata* growing in N-limited continuous cultures. *BBA - Bioenergetics*, 808(1), 149–155. [https://doi.org/10.1016/0005-2728\(85\)90037-4](https://doi.org/10.1016/0005-2728(85)90037-4)
- Kapdan, I. K., & Kargi, F. (2006, March). Bio-hydrogen production from waste materials. *Enzyme and Microbial Technology*. <https://doi.org/10.1016/j.enzmictec.2005.09.015>
- Kong, B., & Vigil, R. D. (2014). Simulation of photosynthetically active radiation distribution in algal photobioreactors using a multidimensional spectral radiation model. *Bioresource Technology*, 158, 141–148. <https://doi.org/10.1016/j.biortech.2014.01.052>
- Krujatz, F., Illing, R., Krautwer, T., Liao, J., Helbig, K., Goy, K., ... Weber, J. (2015). Light-

- field-characterization in a continuous hydrogen-producing photobioreactor by optical simulation and computational fluid dynamics. *Biotechnology and Bioengineering*, 112(12), 2439–2449. <https://doi.org/10.1002/bit.25667>
- Kunjapur, A. M., & Eldridge, R. B. (2010). Photobioreactor design for commercial biofuel production from microalgae. *Industrial and Engineering Chemistry Research*, 49(8), 3516–3526. <https://doi.org/10.1021/ie901459u>
- Lide, D. R. (2003). CRC Handbook of Chemistry and Physics. *CRC Handbook of Chemistry and Physics*, 1264–1266. <https://doi.org/10.1021/ja906434c>
- Louisos, W. F., Hitt, D. L., & Danforth, C. M. (2013). Chaotic flow in a 2D natural convection loop with heat flux boundaries. *International Journal of Heat and Mass Transfer*, 61(1), 565–576. <https://doi.org/10.1016/j.ijheatmasstransfer.2013.02.015>
- Luo, H. P., & Al-Dahhan, M. H. (2004). Analyzing and Modeling of Photobioreactors by Combining First Principles of Physiology and Hydrodynamics. *Biotechnology and Bioengineering*, 85(4), 382–393. <https://doi.org/10.1002/bit.10831>
- Luo, H. P., & Al-Dahhan, M. H. (2011). Verification and validation of CFD simulations for local flow dynamics in a draft tube airlift bioreactor. *Chemical Engineering Science*, 66(5), 907–923. <https://doi.org/10.1016/j.ces.2010.11.038>
- MacIsaac, D., Kanner, G., & Anderson, G. (1999). Basic physics of the incandescent lamp (lightbulb). *The Physics Teacher*, 37(9), 520–525. <https://doi.org/10.1119/1.880392>
- Malalasekera, W., & Versteeg, H. K. (2006). *An Introduction to Computational Fluid Dynamics - The Finite Volume Method*. *AIAA Journal* (Vol. 44). <https://doi.org/10.2514/1.22547>
- Malik, A. H., Shah, A., & Khushnood, S. (2013). CFD analysis of heat transfer within a bottom heated vertical concentric cylindrical enclosure. In *Journal of Physics: Conference Series* (Vol. 439). <https://doi.org/10.1088/1742-6596/439/1/012004>
- Massart, A., Mirisola, A., Lupant, D., Thomas, D., & Hantson, A. L. (2014). Experimental characterization and numerical simulation of the hydrodynamics in an airlift photobioreactor for microalgae cultures. *Algal Research*, 6(PB), 210–217.

<https://doi.org/10.1016/j.algal.2014.07.003>

- Molina-Grima, E., Acien, G., Camacho, F. G., Chisti, Y., Molina Grima, E., Acien Fernández, F. G., & Camacho, F. G. (1999). Hydrogen production from empty fruit bunch hydrolysate by photosynthetic bacteria View project Biotechnology of marine microalgae: development of antibiofouling surfaces for photobioreactors View project Photobioreactors: light regime, mass transfer, and . *Article in Journal of Biotechnology Journal of Biotechnology*, 70(1–3), 231–247. [https://doi.org/10.1016/S0168-1656\(99\)00078-4](https://doi.org/10.1016/S0168-1656(99)00078-4)
- Molina, E., Fernández, J., Acien, F. G., & Chisti, Y. (2001). Tubular photobioreactor design for algal cultures. *Journal of Biotechnology*, 92(2), 113–131. [https://doi.org/10.1016/S0168-1656\(01\)00353-4](https://doi.org/10.1016/S0168-1656(01)00353-4)
- Morrison, G. L., & Braun, J. E. (1985). System modeling and operation characteristics of thermosyphon solar water heaters. *Solar Energy*, 34(4–5), 389–405. [https://doi.org/10.1016/0038-092X\(85\)90051-9](https://doi.org/10.1016/0038-092X(85)90051-9)
- Morrison, G. L., Budihardjo, I., & Behnia, M. (2005). Measurement and simulation of flow rate in a water-in-glass evacuated tube solar water heater. *Solar Energy*, 78(2), 257–267. <https://doi.org/10.1016/j.solener.2004.09.005>
- Murphy, T. E., & Berberoğlu, H. (2011). Effect of algae pigmentation on photobioreactor productivity and scale-up: A light transfer perspective. *Journal of Quantitative Spectroscopy and Radiative Transfer*, 112(18), 2826–2834. <https://doi.org/10.1016/j.jqsrt.2011.08.012>
- Nogi, Y., Akiba, T., & Horikoshi, K. (1985). Wavelength dependence of photoproduction of hydrogen by rhodospirillum rubrum. *Agricultural and Biological Chemistry*, 49(1), 35–38. <https://doi.org/10.1080/00021369.1985.10866684>
- Ogbonna, J. C., Yada, H., & Tanaka, H. (1995). Light supply coefficient: A new engineering parameter for photobioreactor design. *Journal of Fermentation and Bioengineering*, 80(4), 369–376. [https://doi.org/10.1016/0922-338X\(95\)94206-7](https://doi.org/10.1016/0922-338X(95)94206-7)
- Ogueke, N. V., Anyanwu, E. E., & Ekechukwu, O. V. (2009). A review of solar water heating

- systems. *Journal of Renewable and Sustainable Energy*, 1(4), 043106.  
<https://doi.org/10.1063/1.3167285>
- Pilkhwal, D. S., Ambrosini, W., Forgione, N., Vijayan, P. K., Saha, D., & Ferreri, J. C. (2007a). Analysis of the unstable behaviour of a single-phase natural circulation loop with one-dimensional and computational fluid-dynamic models. *Annals of Nuclear Energy*, 34(5), 339–355. <https://doi.org/10.1016/j.anucene.2007.01.012>
- Pilkhwal, D. S., Ambrosini, W., Forgione, N., Vijayan, P. K., Saha, D., & Ferreri, J. C. (2007b). Analysis of the unstable behaviour of a single-phase natural circulation loop with one-dimensional and computational fluid-dynamic models. *Annals of Nuclear Energy*, 34(5), 339–355. <https://doi.org/10.1016/j.anucene.2007.01.012>
- Pilon, L., Berberoğlu, H., & Kandilian, R. (2011). Radiation transfer in photobiological carbon dioxide fixation and fuel production by microalgae. *Journal of Quantitative Spectroscopy and Radiative Transfer*. <https://doi.org/10.1016/j.jqsrt.2011.07.004>
- Pires, J. C. M., Alvim-ferraz, M. C. M., & Martins, F. G. (2017). Photobioreactor design for microalgae production through computational fluid dynamics : A review. *Renewable and Sustainable Energy Reviews*, 79(May), 248–254. <https://doi.org/10.1016/j.rser.2017.05.064>
- Posten, C. (2009). Design principles of photo-bioreactors for cultivation of microalgae. *Engineering in Life Sciences*, 9(3), 165–177. <https://doi.org/10.1002/elsc.200900003>
- Pulz, O. (2001). Photobioreactors: Production systems for phototrophic microorganisms. *Applied Microbiology and Biotechnology*, 57(3), 287–293. <https://doi.org/10.1007/s002530100702>
- Ramírez-Duque, J. L., & Ramos-Lucumi, M. A. (2011). Hydrodynamic computational evaluation in solar tubular photobioreactors bends with different cross sections. *CTyF - Ciencia, Tecnología y Futuro*, 4(4), 59–72.
- Rek, Z., Rudolf, M., & Zun, I. (2012). Application of CFD Simulation in the Development of a New Generation Heating Oven. *Strojniški Vestnik – Journal of Mechanical Engineering*, 58(2), 134–144. <https://doi.org/10.5545/sv-jme.2011.163>
- Reyna-Velarde, R., Cristiani-Urbina, E., Hernández-Melchor, D. J., Thalasso, F., & Cañizares-



- Villanueva, R. O. (2010). Hydrodynamic and mass transfer characterization of a flat-panel airlift photobioreactor with high light path. *Chemical Engineering and Processing: Process Intensification*, 49(1), 97–103. <https://doi.org/10.1016/j.cep.2009.11.014>
- Roldán, M. I., Smirnova, O., Fend, T., Casas, J. L., & Zarza, E. (2014). Thermal analysis and design of a volumetric solar absorber depending on the porosity. *Renewable Energy*, 62, 116–128. <https://doi.org/10.1016/j.renene.2013.06.043>
- Rout, S. K., Thatoi, D. N., Acharya, A. K., & Mishra, D. P. (2012a). CFD supported performance estimation of an internally finned tube heat exchanger under mixed convection flow. *Procedia Engineering*, 38(Icmoc), 585–597. <https://doi.org/10.1016/j.proeng.2012.06.073>
- Rout, S. K., Thatoi, D. N., Acharya, A. K., & Mishra, D. P. (2012b). CFD supported performance estimation of an internally finned tube heat exchanger under mixed convection flow. In *Procedia Engineering* (Vol. 38, pp. 585–597). Elsevier B.V. <https://doi.org/10.1016/j.proeng.2012.06.073>
- Samanci, A., & Berber, A. (2011). Experimental investigation of single-phase and two-phase closed thermosyphon solar water heater systems. *Scientific Research and Essays*, 6(4), 688–693. <https://doi.org/10.5897/SRE09.072>
- Sato, T., Yamada, D., & Hirabayashi, S. (2010). Development of virtual photobioreactor for microalgae culture considering turbulent flow and flashing light effect. *Energy Conversion and Management*, 51(6), 1196–1201. <https://doi.org/10.1016/j.enconman.2009.12.030>
- Shariah, A., & Shalabi, B. (1997). Optimal design for a thermosyphon solar water heater. *Renewable Energy*, 11(3), 351–361. [https://doi.org/10.1016/S0960-1481\(97\)00005-0](https://doi.org/10.1016/S0960-1481(97)00005-0)
- Shukla, R., Sumathy, K., Erickson, P., & Gong, J. (2013). Recent advances in the solar water heating systems: A review. *Renewable and Sustainable Energy Reviews*, 19, 173–190. <https://doi.org/10.1016/j.rser.2012.10.048>
- Sierra, E., Ación, F. G., Fernández, J. M., García, J. L., González, C., & Molina, E. (2008). Characterization of a flat plate photobioreactor for the production of microalgae. *Chemical*

- Engineering Journal*, 138(1–3), 136–147. <https://doi.org/10.1016/j.cej.2007.06.004>
- Skjånes, K., Andersen, U., Heidorn, T., & Borgvang, S. A. (2016). Design and construction of a photobioreactor for hydrogen production, including status in the field. *Journal of Applied Phycology*, 28(4), 2205–2223. <https://doi.org/10.1007/s10811-016-0789-4>
- Soman, A., & Shastri, Y. (2015). Optimization of novel photobioreactor design using computational fluid dynamics. *Applied Energy*, 140, 246–255. <https://doi.org/10.1016/j.apenergy.2014.11.072>
- Tamburic, B., Zemichael, F. W., Crudge, P., Maitland, G. C., & Hellgardt, K. (2011a). Design of a novel flat-plate photobioreactor system for green algal hydrogen production. *International Journal of Hydrogen Energy*, 36(11), 6578–6591. <https://doi.org/10.1016/j.ijhydene.2011.02.091>
- Tamburic, B., Zemichael, F. W., Crudge, P., Maitland, G. C., & Hellgardt, K. (2011b). Design of a novel flat-plate photobioreactor system for green algal hydrogen production. *International Journal of Hydrogen Energy*, 36(11), 6578–6591. <https://doi.org/10.1016/j.ijhydene.2011.02.091>
- USHIO America, I. (2018). Halogen Lamps Technical Specifications Data. Retrieved from <https://www.ushio.com/technology/halogen/>
- Vijayan, P. K., Sharma, M., & Saha, D. (2007). Steady state and stability characteristics of single-phase natural circulation in a rectangular loop with different heater and cooler orientations. *Experimental Thermal and Fluid Science*, 31(8), 925–945. <https://doi.org/10.1016/j.expthermflusci.2006.10.003>
- Wang, B., Lan, C. Q., & Horsman, M. (2012). Closed photobioreactors for production of microalgal biomasses. *Biotechnology Advances*. Elsevier Inc. <https://doi.org/10.1016/j.biotechadv.2012.01.019>
- Wheaton, Z. C., & Krishnamoorthy, G. (2012). Modeling radiative transfer in photobioreactors for algal growth. *Computers and Electronics in Agriculture*, 87, 64–73. <https://doi.org/10.1016/j.compag.2012.05.002>

- Williamson, M. E., & Wilson, D. I. (2009). Development of an improved heating system for industrial tunnel baking ovens. *Journal of Food Engineering*, *91*(1), 64–71. <https://doi.org/10.1016/j.jfoodeng.2008.08.004>
- Xu, B., Li, P., & Waller, P. (2014). Study of the flow mixing in a novel ARID raceway for algae production. *Renewable Energy*, *62*, 249–257. <https://doi.org/10.1016/j.renene.2013.06.049>
- Yang, Z., Cheng, J., Ye, Q., Liu, J., Zhou, J., & Cen, K. (2016). Decrease in light/dark cycle of microalgal cells with computational fluid dynamics simulation to improve microalgal growth in a raceway pond. *Bioresource Technology*, *220*, 352–359. <https://doi.org/10.1016/j.biortech.2016.08.094>
- Yu, G., Li, Y., Shen, G., Wang, W., Lin, C., Wu, H., & Chen, Z. (2009). A novel method using CFD to optimize the inner structure parameters of flat photobioreactors. *Journal of Applied Phycology*, *21*(6), 719–727. <https://doi.org/10.1007/s10811-009-9407-z>
- Zhang, D., Dechatiwongse, P., & Hellgardt, K. (2015). Modelling light transmission , cyanobacterial growth kinetics and fluid dynamics in a laboratory scale multiphase photobioreactor for biological hydrogen production. *Algal Research*, *8*, 99–107. <https://doi.org/10.1016/j.algal.2015.01.006>
- Zhang, D., Xiao, N., Mahbubani, K. T., del Rio-Chanona, E. A., Slater, N. K. H., & Vassiliadis, V. S. (2015). Bioprocess modelling of biohydrogen production by *Rhodospseudomonas palustris*: Model development and effects of operating conditions on hydrogen yield and glycerol conversion efficiency. *Chemical Engineering Science*, *130*, 68–78. <https://doi.org/10.1016/j.ces.2015.02.045>
- Zhang, T. (2013). Dynamics of fluid and light intensity in mechanically stirred photobioreactor. *Journal of Biotechnology*, *168*(1), 107–116. <https://doi.org/10.1016/j.jbiotec.2013.07.007>
- Zvirin, Y. (1982). A review of natural circulation loops in pressurized water reactors and other systems. *Nuclear Engineering and Design*, *67*(2), 203–225. [https://doi.org/10.1016/0029-5493\(82\)90142-X](https://doi.org/10.1016/0029-5493(82)90142-X)

## APPENDIX A: UDF SOURCE CODE

User define function for the implementation of non-uniform volumetric heat generation term

```

    /*heat_source udf for non-uniform volumetric heat generation due to light penetration*/
#include "udf.h"

#define I_o1 1.42916235e+03 /*radiant intensity for 350-450nm (W/m2)*
#define I_o2 5.254294537e+03 /*radiant intensity for 450-550nm (W/m2)*
#define I_o3 1.105942157e+04 /*radiant intensity for 550-650nm (W/m2)*
#define I_o4 1.694148845e+04 /*radiant intensity for 650-750nm (W/m2)*
#define I_o5 2.145313883e+04 /*radiant intensity for 750-850nm (W/m2)*
#define I_o6 2.411873212e+04 /*radiant intensity for 850-950nm (W/m2)*

#define Kb_o1 2.2042e+02 /*350-450nm bacterial mass absorption coefficient (m2/Kg) */
#define Kb_o2 2.2344e+02 /*450-550nm bacterial mass absorption coefficient (m2/Kg) */
#define Kb_o3 1.7231e+02 /*550-650nm bacterial mass absorption coefficient (m2/Kg) */
#define Kb_o4 1.2378e+02 /*650-750nm bacterial mass absorption coefficient (m2/Kg) */
#define Kb_o5 1.7758e+02 /*750-850nm bacterial mass absorption coefficient (m2/Kg) */
#define Kb_o6 1.2465e+02 /*850-950nm bacterial mass absorption coefficient (m2/Kg) */

#define X 0.5 /*bacterial biomass concentration (kg/m3)*
#define X_1 1.934554e-01 /* light entering point (m) */

/*All dimensions are in SI units*/

DEFINE_SOURCE(heat_source, c, t, dS, eqn)
{
    real xc[ND_ND]; /*position vector */
    real Z, K_o1, K_o2, K_o3, K_o4, K_o5, K_o6, source;

```

```

    K_o1=Kb_o1*X, K_o2=Kb_o2*X, K_o3=Kb_o3*X, K_o4=Kb_o4*X, K_o5=Kb_o5*X,
    K_o6=Kb_o6*X; /*overall spectral attenuation coefficients (m^-1)*/

    C_CENTROID(xc,c,t); /*acquire the cell centeriod*/

    Z= X_1 - xc[0]; /*determine the distance from the light entering point */

    source = - 1.0*((K_o1*I_o1*exp(-K_o1*Z))+(K_o2*I_o2*exp(-
    K_o2*Z))+(K_o3*I_o3*exp(-K_o3*Z))+(K_o4*I_o4*exp(-K_o4*Z))+(K_o5*I_o5*exp(-
    K_o5*Z))+(K_o6*I_o6*exp(-K_o6*Z))); /*spectral energy source term (W/m^3)*/

    printf("Z is %e source is %e\n", Z, source); /* display on screen for inspection */

    dS[eqn]=0.0;

    return (-1*source); /* (-1) accounts for the opposition orientation of physical riser position */

}

```

## APPENDIX B: ANSYS WORKBENCH ENVIRONMENT

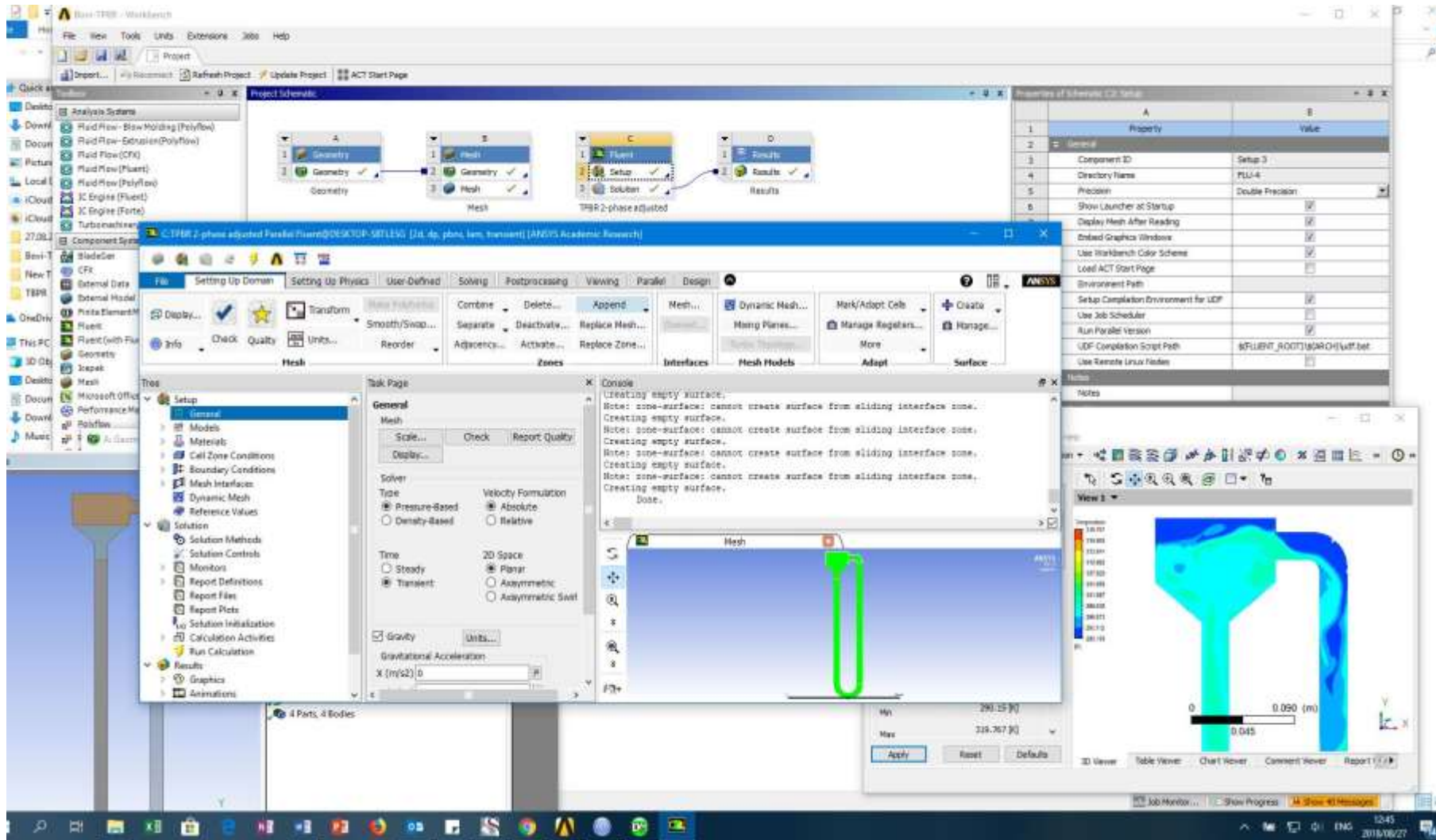


Figure 44: Photograph of the ANSYS workbench environment used throughout the simulation process of this work

## APPENDIX C: CFD RESIDUAL MONITORING

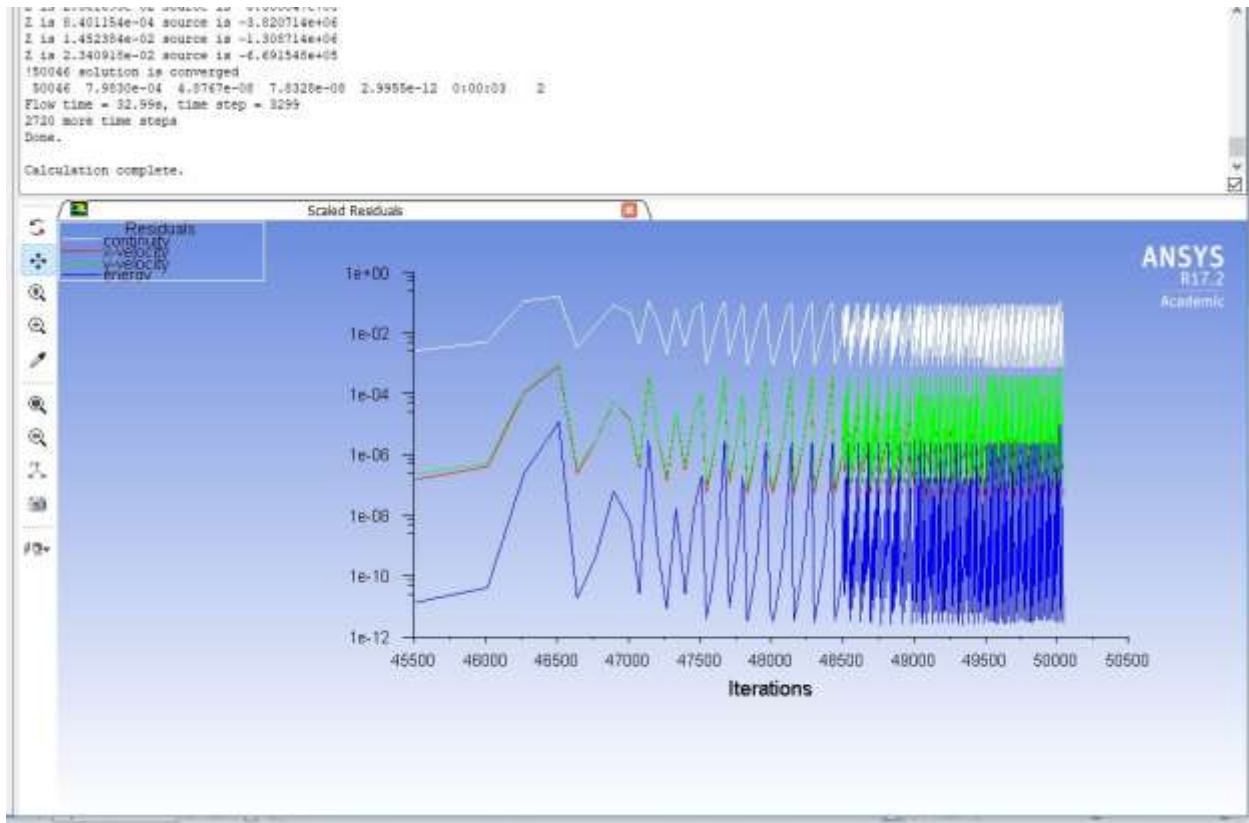


Figure 45: photograph of the scaled residuals used throughout the simulation process of this work

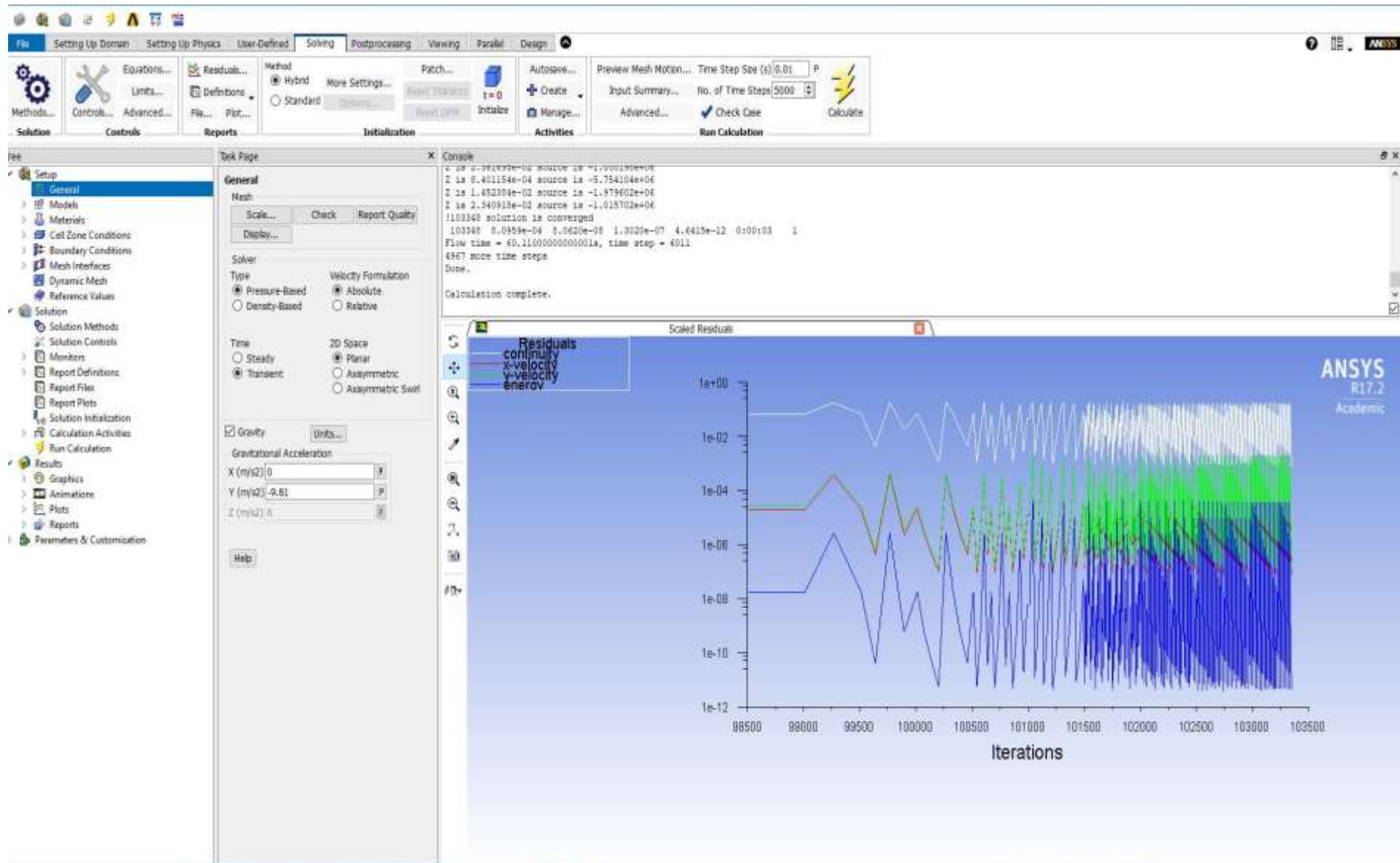


Figure 46: photograph of the final scaled residuals used for the simulation process of this work



## APPENDIX C: NEWTON'S LAW OF COOLING

### Application of newton's law of cooling to model the heat transfer coefficient of the TPBR's cooling and riser walls

The newton's law of cooling states that the rate of cooling/heating of an object is approximately proportional to the temperature difference between the object and its environment according to equation (1)

$$\dot{Q} = -hA(T_s - T_\infty) \quad (43)$$

Where  $\dot{Q}$ ,  $h$ ,  $A$ ,  $T_s$ , and  $T_\infty$  are the rate of cooling/heating, heat transfer coefficient, area, temperature of the object and temperature of the environment respectively.

$$\dot{Q} \equiv \rho V C_p \frac{dT}{dt} - hA(T_s - T_\infty) \quad (44)$$

$$\frac{\rho V C_p}{hA} \frac{dT}{dt} = -(T_s - T_\infty) \quad (45)$$

Let  $\frac{\rho V C_p}{hA} = \tau$ , the thermal time constant and substituted in equation 5

$$\tau \frac{dT}{dt} = -(T_s - T_\infty) \quad (46)$$

$$\frac{1}{T_s - T_\infty} dT = \frac{-1}{\tau} dt \quad (47)$$

$$\int_{T_{si}}^{T_s} \frac{1}{T_s - T_\infty} dT = \frac{-1}{\tau} \int_0^t 1 dt \quad (48)$$

$$\ln|T_s - T_\infty|_{T_{si}}^{T_s} = \frac{-t}{\tau} \quad (49)$$

Since the object (TPBR's cooling and riser walls) are cooling down to the environment,  $T_s > T_\infty$  implying that  $|T_s - T_\infty| = (T_s - T_\infty)$

$$\ln(T_s - T_\infty)_{T_{si}}^{T_s} = \frac{-t}{\tau} \quad (50)$$

$$\left( \frac{T_s - T_\infty}{T_{si} - T_\infty} \right) = e^{-t/\tau} \quad (51)$$

$$T_s = (T_{si} - T_\infty)e^{-t/\tau} + T_\infty \quad (52)$$

From equation 42, the heat transfer coefficient of the TPBR's cooling and riser walls are estimated by curve fitting the following equations with experimental data

1. Heat transfer coefficient of cooling walls

$$T(t) = (T_{stab} - T_{w,out})e^{\left(-\frac{th_c A_c}{\rho V C_p}\right)} + T_{w,out} \quad (53)$$

Where  $M$ ,  $\rho$ ,  $V$  and  $C_p$  are the mass (kg), density ( $Kg/m^3$ ), volume ( $m^3$ ), and specific heat capacity ( $J/Kg.K$ ) of water respectively,  $\dot{Q}_{lights}$  and  $\dot{Q}_{lost}$  are the rate of heating (J/s) by halogen lamps and rate of losing heat (J/s) by convection respectively,  $t$  is time (s),  $h_c$  is the heat transfer coefficient of cooling section ( $J/s.K$ ),  $T_{stab}$  and  $T_{w,out}$  are the stabilization and outlet sub cooling water temperatures (K) respectively.

2. Heat transfer coefficient of the riser walls

$$T(t) = (T_s - T_\infty)e^{\left(-\frac{th_r A_r}{\rho V C_p}\right)} + T_\infty \quad (54)$$

Where  $h_r$  and  $A_r$  are the heat transfer coefficient ( $J/s.K$ ) and area ( $m^2$ ) of the riser section respectively,  $T_s$  and  $T_\infty$  represent the hot water and ambient temperature (k) respectively.

**APPENDIX D: R. PALUSTRIS GROWTH FORMULA**

Stock No	Chemical name	Chemical formula	Weight (g)	Distill water (mL)	
<b>BUFFER SOLUTIONS</b>					
1	Potassium phosphate dibasic	$K_2HPO_4$	17	100	
2	Potassium phosphate monobasic	$KH_2PO_4$	17	100	
<b>BULK NUTRIENTS</b>					
3	Yeast extract	$C_{19}H_{14}O_2$	2	1,000	
4	Sodium thiosulphate pentahydrate	$NaS_2O_3 \cdot 5H_2O$	2.51		
5	4-Aminobenzoic acid	<i>PABA</i>	0.02		
6	Magnesium Sulphate heptahydrate	$MgSO_4 \cdot 7H_2O$	2		
7	Calcium chloride dydrate	$CaCl_2 \cdot 2H_2O$	0.5		
8	Sodium chloride	<i>NaCl</i>	4		
9	Ferric citrate	$FeC_6H_5O_7$	0.05		
<b>TRACE ELEMENTS</b>					
10	Zinc chloride	<i>ZnCl</i>	$70 \times 10^{-3}$		1,000
11	Manganese (II) chloride tetrahydrate	$MnCl_2 \cdot 4H_2O$	$100 \times 10^{-3}$		
12	Boric acid	$H_3BO_3$	$60 \times 10^{-3}$		
13	Cobalt (II) chloride hexahydrate	$CoCl_2 \cdot 6H_2O$	$200 \times 10^{-3}$		
14	Calcium sulphate dihydrate	$CuSO_4 \cdot 2H_2O$	$30 \times 10^{-3}$		
15	Nickel (II) chloride hexahydrate	$NiCl_2 \cdot 6H_2O$	$22 \times 10^{-3}$		
16	Sodium molybdate	$Na_2MoO_4 \cdot 2H_2O$	$40 \times 10^{-3}$		
<b>STRILE ADDITIONS</b>					
17	Glycerol	$C_3H_8O_3$	29.43	100	
18	Na- glutamate	$NaC_5H_8NO_4$	34.02	100	
19	Vitamin B12	$C_{63}H_{88}CoN_{14}P$	0.001	100	
20	Thiamine	$C_{12}H_{17}N_4OS +$	0.12	100	
<b>pH ADJUSTMENT</b>					
21	Sodium hydroxide	<i>NaOH</i>	40	100	

## APPENDIX E: COMPOSITON OF INOCULATED GROWTH MEDIA FOR *R. PALUSTRIS*

SN	Composition	Volume (mL)
1	<b>Buffer solutions</b>	
	I. $K_2HPO_4$	10
	II. $KH_2PO_4$	10
2	<b>Bulk nutrients</b>	100
3	<b>Water</b>	982
4	<b>10M NaOH (sets pH to <math>\pm 7.3</math>)</b>	19 to 21 drops
5	<b>Sterile additions</b>	
	I. 5M Glycerol	10
	II. 2M Na- glutamate	5
	III. Vitamin B12	1
	IV. Thiamine	1
	V. Trace elements	1

## APPENDIX F: EXPERIMENTAL EQUIPMENT

Calculating the dilution factor for preparing an active *R. palustris* medium of  $0.5 \frac{g \text{ bacteria}}{L \text{ solution}}$

$$\text{Dilution factor} = \frac{V_{TOTAL}}{V_{SOLUTION}} \quad (55)$$

Considering a 1ml sample and diluting it with a factor of 4,

$$\text{Dilution factor} = \frac{1ml}{0.25ml} \quad (56)$$

Therefore

$$\text{Dilution factor} = 4 \frac{L_{solution}}{L_{stock}} \quad (57)$$

Measuring the optical density of the sample and converting it to biomass concentration with the calibration curve Figure and following equations

$$\text{Sample's biomass concentration} = (\text{Optical density} \times 0.699) + 0.0182 \quad (58)$$

And

$$\begin{aligned} \text{Stock's biomass concentration} \\ = \text{Sample's biomass concentration} \times \text{dilution factor} \end{aligned} \quad (59)$$

Table 15: Results of the biomass concentration calculations for active *R. palustris*

Sample No	Dilution factor	Optical density	Sample's biomass Concentration (g/L)	Sample's biomass Concentration (g/L)
1	4	0.418	0.310	1.242
2	4	0.597	0.436	1.742
3	4	0.577	0.422	1.686
4	4	0.564	0.412	1.650
			0.395	1.580

Required dilution factor

$$= \text{Average stock's biomass} \frac{\text{g bacteria}}{\text{L stock}} \times \frac{1}{0.5} \frac{\text{L stock}}{\text{g bacteria}} \quad (60)$$

And

$$\text{Required dilution factor} = 1.580 \frac{\text{g bacteria}}{\text{L stock}} \times \frac{1}{0.5} \frac{\text{L stock}}{\text{g bacteria}} \quad (61)$$

Therefore

$$\text{Required dilution factor} = 3.160 \frac{\text{g bacteria}}{\text{L stock}} \quad (62)$$

Also,

$$V_{\text{stock}} \text{ addition} = V_{\text{solution}} \div \text{required dilution factor} \quad (63)$$

Hence

$$V_{\text{stock},l} \text{ addition (ml)} = 1000 \text{ ml} \div 3.160 \frac{\text{g bacteria}}{\text{L stock}} \quad (64)$$

$$V_{\text{stock},l} \text{ addition (ml)} = 316.5 \text{ ml} \quad (65)$$

Therefore

316.5 mL of the active growing *R. palustris* was measured and added to 683.5 ml of deionized water to make up the 1000 mL medium used for testing.

**Calculating the dilution factor for preparing an active *R. palustris* medium of  $0.5 \frac{\text{g bacteria}}{\text{L solution}}$**

Table 16: Results of the biomass concentration calculations for inactivated *R. palustris*

Sample No	Dilution factor	Optical density	Sample's biomass Concentration (g/L)	Sample's biomass Concentration (g/L)
1	4	0.448	0.331	1.325
2	4	0.469	0.346	1.384
3	4	0.514	0.377	1.510
Average			0.352	1.406

$$\text{Required dilution factor} = 1.406 \frac{\text{g bacteria}}{\text{L stock}} \times \frac{1}{0.5} \frac{\text{L stock}}{\text{g bacteria}} \quad (66)$$

Therefore

$$\text{Required dilution factor} = 2.813 \frac{\text{g bacteria}}{\text{L stock}} \quad (67)$$

Also,

$$V_{\text{stock addition}} = V_{\text{solution}} \div \text{required dilution factor} \quad (68)$$

Hence

$$V_{\text{stock},l} \text{ addition (ml)} = 1000 \text{ ml} \div 2.813 \frac{\text{g bacteria}}{\text{L stock}} \quad (69)$$

$$V_{\text{stock},l} \text{ addition (ml)} = 355.5 \text{ ml} \quad (70)$$

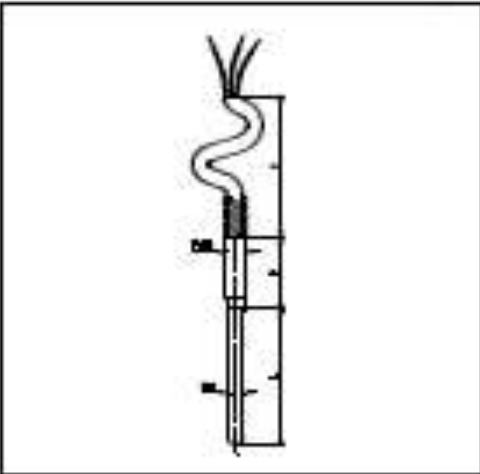
Therefore

355.5 mL of the inactivated *R. palustris* was measured and added to 644.5 ml of deionized water to makeup the 1000 mL medium used for testing.

# APPENDIX F: THERMOCOUPLE MANUFACTURER'S SPECIFICATION

<b>WIKAI</b> Temperature		Production: W _____	DDL: _____	Rev 19812
STANDARD RTD WITH POINTED SEAL & EXT. LEADS OPTIONAL PROCESS CONNECTION		MODEL: REB (TR40)		



RESISTOR: ref. DB81	Configuration
TY 'B' -50/+450	2-wire
TY 'A' -50/+450	3-wire
CER 'B' -200/+600	4-wire
CER 'A' -200/+600	OTHER:
GLAS 'B' -200/+400	

Process Conn. (Type)	Process Conn. Mat.:
None (1)	SS316
Comp. Fitting (2)	BRASS
Cap-Nut (3)	OTHER:
Setral Conn. (4)	

Process Conn. Thread :	1/4" BSP
1/4" BSP	1/4" NPT
1/4" NPT	OTHER:

Tag	Fit to TW
Coat. Cart.	Cal. Cart.
Insulation	on W

Mark required box with 'X'

T1	R	E	B				
----	---	---	---	--	--	--	--

SENSOR TYPE	1 1/2 100	3 1/2 100	8 Special				
	2 1/2 1000	4 1/2 120					
NO. OF SENSORS	8 Single	8 Double	8 Triple				
MATERIAL	G Stainless SS316		E Other Material				
	H Inconel SS316						
PROBE DIAMETER	M 5.0mm		S3 Special				
	4T 4.75mm	M 6.0mm					
	M 6.0mm	E 12.0mm					

SPECIFIC DETAILS:	WIKAI Ref.:	NOTES:	SPECIFIC DETAILS:	WIKAI Ref.:	NOTES:
PROBE LENGTH (L):	IR 010		IMMERSION LENGTH (Typ. L <sub>i</sub> =L <sub>s</sub> +40mm)	L <sub>i</sub> =	
CABLE INSULATION:			CABLE LENGTH (X):		
OTHER SPECIFICATIONS:					

QTY.:	REF. CODE:	SALES J. NO.:	CUSTOMER:	ORIGINATOR:	DATE:
MRF REF. NO.:		MRF.:		PLANNER:	DATE:
W					

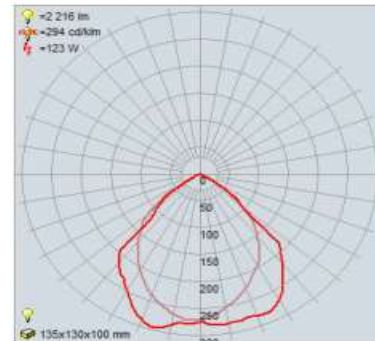
WIKAI 4076 (002) (071) 170, Callfax (002) 4076 2094, Johannesburg, P.O. Box 71033, Germiston 2047, Tel: (011) 427-9000, Fax: (011) 427-9002



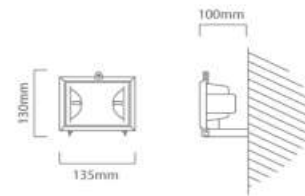
## APPENDIX G: HALOGEN LAMP MANUFACTURERS GUIDE



**FS13 IES DIAGRAM**



**FS13 CAD DIAGRAM**



### FS13: ENCL. FLOODLIGHT 150W W/TUBE BLACK

**BARCODE:** 6007328001157  
**COLOUR:** Black  
**MATERIAL:** Die Cast Aluminium  
**LENS:** Clear Tempered Glass  
**IP RATING:** 54

**PACK SIZE:** 16  
**WIDTH:** 135mm  
**HEIGHT:** 130mm  
**DEPTH:** 100mm  
**LAMP TYPE:** Including 1 x R7s max 150W QI Premium J78 230V

**ADDITIONAL INFO:** Spare Glass: X017

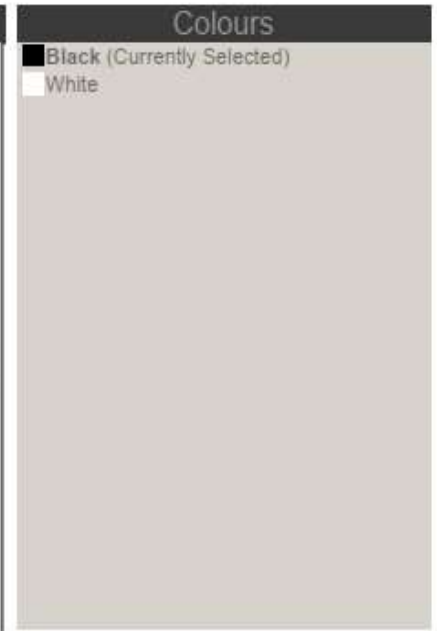
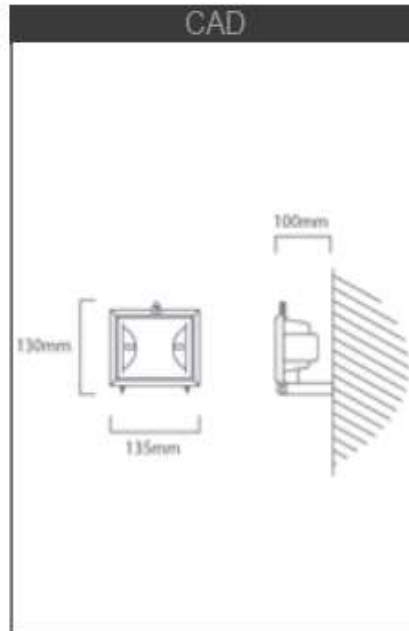
### CONTACT US

Cape Town - 9 Racecourse Road, Milnerton, 7441  
 Johannesburg - 10 Milkyway Avenue, Linbro Business Park, Sandton, 2065  
 email: [admin@eurolux.co.za](mailto:admin@eurolux.co.za), [www.eurolux.co.za](http://www.eurolux.co.za)

**eurolux**

Lighting your way

**Product Spec Sheet**



Fitting Details	
Rectangular Flood Light	
Fitting code	FS13B
Fitting Colour	Black
IP rating	55
Lens/Shade Color	Clear
Lens/Shade	Glass
Material	
Class	1
Box Qty	16 per box
Fitting Material	Die Cast Aluminium
Height	130mm
Width	135mm
Depth	100mm
Barcode	6007328001157
Spares	Spare Glass: X017

Lamps used by Fitting	
Description	R7S 150W Q1 Premium J78 Halogen
Type	Halogen
Base	R7S
Wattage	150W
Voltage	240V
Luminous flux	2200lm
Dimmable	Yes
Colour	Warm White
Color in Temp	2900K
Lifetime	2000hours
Max lenght	78mm
Diameter	9mm
Box Qty	50per box
Barcode	6007328030294